AxisSPH:Devising and validating an axisymmetric smoothed particle hydrodynamics code

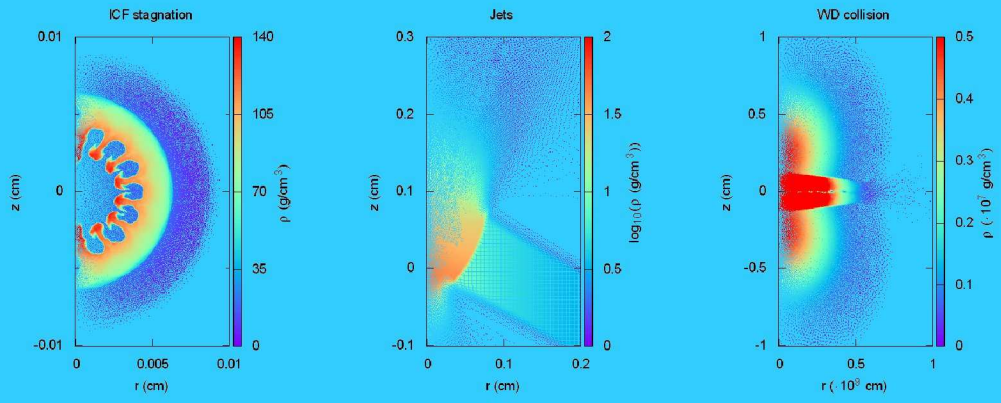

PhD Thesis

Antonio Relaño Castillo

GRUP D'ASTRONOMIA I ASTROFÍSICA

UNIVERSITAT POLITÈCNICA DE CATALUNYA

UNIVERSITAT POLITÈCNICA DE CATALUNYA

DEPARTAMENT DE FÍSICA I ENGINYERIA NUCLEAR

GRUP D'ASTRONOMIA I ASTROFÍSICA

AxisSPH: DEVISING AND VALIDATING AN AXISYMMETRIC SMOOTHED PARTICLE HYDRODYNAMICS CODE

UNIVERSITAT POLITÈCNICA DE CATALUNYA

Memòria presentada per
Antonio Relaño Castillo
per optar al grau de
Doctor en Ciències

Barcelona, Abril de 2012

Programa de Física Computacional i Aplicada

Memòria presentada per **Antonio Relaño Castillo**
per optar al grau de Doctor en Ciències

Director de la tesi

Antonio Relaño Castillo

Dr. Domingo García Senz

A María Ángeles,
Néstor y Raúl

Si viviéramos en un planeta donde nunca cambia nada, habría poco que hacer. No habría nada que explicarse. No habría estímulo para la ciencia. Y si viviéramos en un mundo impredecible, donde las cosas cambian de modo fortuito o muy complejo, seríamos incapaces de explicarnos nada. Tampoco en este caso podría existir la ciencia. Pero vivimos en un universo intermedio...

Carl Sagan, *Cosmos*

-No está muy claro -dijo Etienne.
-No puede estar claro, si lo estuviera sería falso, sería científicamente verdadero quizá, pero falso como absoluto. La claridad es una exigencia intelectual y nada más. Ojalá pudiéramos saber claro, entender claro al margen de la ciencia y la razón. Y cuando digo "ojalá", andá a saber si no estoy diciendo una idiotez. Probablemente la única áncora de salvación sea la ciencia, el uranio 235, esas cosas. Pero además hay que vivir.
-Sí, dijo la Maga, sirviendo café-. Además hay que vivir.

Julio Cortázar, *Rayuela*

Agradecimientos

En primer lugar y de una manera muy especial a María Ángeles por el apoyo y amor recibido desde el principio y durante toda esta larga travesía. Todavía nos quedan otros caminos por recorrer juntos y espero alcanzar muchos otros destinos disfrutando de su compañía.

A Néstor y a Raúl, dos queridísimos polizontes que aunque se embarcaron algo más tarde, me han permitido con su cariño y comprensión llevar a buen puerto esta aventura, pues son muchas las horas que les he robado durante estos años.

Sin la ayuda y la infinita paciencia de Domingo García Senz hubiera sido imposible concluir este trabajo. De él he aprendido mucho y sobre todo que un buen científico nunca debe dejar de buscar, con trabajo y tesón, nuevas estrategias para acercarse a la compresión de la realidad.

Agradecer a Eduard Bravo, Enrique García-Berro y Jordi José la ayuda prestada durante estos años, agradecimiento que hago extensivo al resto de miembros del *Grup d'Astronomia i Astrofísica* y al *Departament de Física i Enginyeria Nuclear* por los medios materiales proporcionados.

En el autodenominado grupo de los astrofísicos he encontrado la complicidad, el compañerismo y también la amistad. Lástima que el nuevo rumbo emprendido por algunos de sus miembros haya disminuido la frecuencia de nuestros encuentros. Muchísimas gracias a todos, en especial a Núria, a Rubén, a Oscar y a Josan.

Y si vuelvo la mirada todavía un poco más atrás, nada podría haber empezado sin el afecto y la protección de mi familia. De Custodia y Vicente, he recibido uno de los mejores regalos de mi vida: aprender el valor del estudio y el esfuerzo. De

Francesc aprendí el amor por el conocimiento a través de la curiosidad; a pesar de la distancia, siempre ha seguido brindándome su ayuda. A Marga agradecerle su continuo e incondicional cariño.

Sinceramente, muchas gracias.

Contents

Chapter 1

Introduction

The first time someone reads the title of this thesis and just has a quick look at the contents of the index it may wonder why spend such amount of effort and time investigating about the axisymmetric version of the numerical technique known as smoothed particle hydrodynamics (SPH). That is a reasonable concern because the technique was originally devised to work in cartesian three dimensions, Gingold and Monaghan [25] and Lucy [37]. Nowadays the technique is in a mature stage and 3D simulations of astrophysical scenarios are routinary conducted worldwide. As the time went on SPH has progressively been applied to other scientific areas, including engineering where two-dimensional (cartesian) simulations using SPH are very common (see for example [40], [49]). Little attention (in comparison) was paid to the development of no cartesian SPH formalisms, and in particular to build a coherent axisymmetric SPH code.

Still, it is surprising the diversity of topics which we were able to model using the novel scheme for the axisymmetric SPH that we present in this thesis. Among them: (1) The growth of hydrodynamic instabilities during the stagnation phase of a microcapsule in Inertial Confinement Fusion (ICF) experiments. (2) Simulations concerning the formation of jets induced by the collision of two streams of gas or by two metallic plates. (3) The head on collision of a pair of white dwarf stars giving birth to a supernova explosion. These are a few examples but the number of applications of an axisymmetric SPH code could be much larger (for instance an axisymmetric code is able to handle rotation around a fixed axis, a topic of great interest to astrophysics and probably to fluid dynamics).

But let's go back for a while to the beginning of this work, many years ago, when we tried to apply the 3D-SPH currently used by our astrophysics group to ICF [66]. Then, we became aware of the difficulties to model the compression process of the capsule even using a very simplified physics. One of the difficulties was the limited resolution of our simulations because even though we manage to follow the compression phase and roughly reproduce the grow of the Rayleigh-Taylor (RT) instability during the stagnation stage the results of the simulations were a bit desappointing because the lack of low scale structure seen in our simulations. There are a lot of physical phenomena involved in standard ICF, perfectly summarized by Nakai and Takabe [51] for the case of confinement by direct laser irradiation (see Fig. 1.1). The flow along the central line of the chart goes through stages that can be handled in spherical symmetry using one-dimensional codes. On the right there are shown the main physical process operating at each stage. Finally multi-dimensional hydrodynamic effects which make the simulation of the phenomena more complicated are depicted on the leftmost part of the diagram. In this thesis we have studied the hydrodynamics during the stagnation phase, using the axisymmetric SPH code with a resolution much higher than that of our previous work [66] and focussed the attention on the quantitative analysis of the RT instability.

Although the spatial and temporal scales of ICF and astrophysics are completely different they share many things. They involve, for example, similar physical processes such as the equation of state (EOS) of dense matter, nuclear reactions, particle transport and convection. The numerical approaches used to study the hydrodynamics of supernova explosions keep many resemblances to that of ICF. Generally speaking the hydrocodes used in ICF studies are grid based codes (such as the adaptive mesh refinement (AMR) or the piecewise parabolic method (PPM)) while in astrophysics the zoo is more varied because we find also SPH codes in many applications. Roughly speaking SPH are used wherever there is a large deformation of the bodies and there is needed a good level of conservation of linear and angular momentum, as in many astrophysical scenarios. On the other hand adaptive Eulerian hydrodynamics (AMR codes for example) give, in many cases, more precise results, as for instance in the treatment of instabilities or shock waves. Nevertheless both family of methods lead to similar results provided a similar resolution is achieved ([30], [80]) but sometimes that would imply a very large number of particles in the case of SPH codes.

Each method has advantages and disadvantages and the choice depends, among

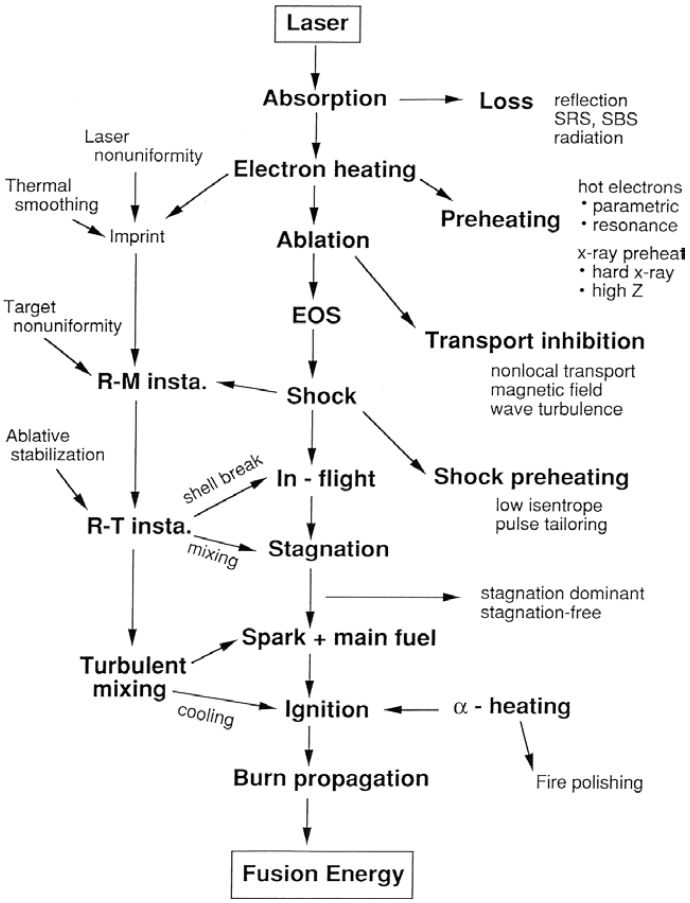

Figure 1.1: The laser fusion physical scenario. The central line is the spherically symmetric implosion and burn scenario (one dimension). The right-hand-side represents the importance of transport issues and high-energy electron production. The processes on the left-hand-side are related to multi-dimensional effects.[Source: Nakai and Takabe(1996) [51].]

other things, on the particular problem to be solved. In SPH the fluid is divided in a set of particles whose motion follows the Lagrangian dynamics in a similar way molecular dynamics work but incorporating forces derived from pressure. In AMR the fluid is modeled by a series of hierarchical meshes in a Eulerian fixed frame. In SPH the fluid properties are calculated at each particle position as a weighted average of the magnitudes attached to the closest particles. SPH can study free-surface flow fenomenae where Eulerian metods can be difficult to aply (see for example [16]). In AMR the fluid properties are calculated evaluating the flow between cells in a rather sophisticated manner. As mentioned AMR based codes have comparatively more resolution in the treatment of shocks and discontinuities because of the im-

plementation of the Riemann solver technique to handle with these problems and because its good adaptive properties. SPH relies in the artificial viscosity formalism to solve shocks and to avoid the numerical oscillations of the rarefaction tail behind the shock. Although there have been notorious improvements in the formulation of that technique ([44],[5]), current implementations of artificial viscosity still smooths in excess the velocity field in regions of strong shear even if they are far from the shock surfaces. Still the artificial technique works reasonably well even in adverse conditions. For example, even though Agertz et al. [1] highlighted the difficulties of SPH to correctly model the Kelvin-Helmholtz instability arising from small perturbations and large density contrasts it was shown that the phenomenon can be simulated by simply adding an artificial heat conduction term to smooth the pressure field [60]. Recently [23] managed to correctly reproduce the KH instability with an alternative formulation of SPH. Another negative point of the SPH formalism is that resolution is proportional to the cubic root of density so that high density regions are better described than rarefied regions. This last point can be overcame by a) increasing the total number of particles to keep the resolution of diluted regions at good level and b) increasing the number of particles only in the low-density regions and using variable mass for them.

Among the virtues of SPH we can cite: (1) Its Lagrangian mesh-free nature (ideal to describe complex geometries). (2) It is fully conservative by construction, (linear an angular momentum and mass are perfectly conserved and energy is also perfectly conserved in isentropic flows). (3) Numerical diffusion is much lower than in Eulerian codes, making it ideally suited to study reactive fluxes. In addition the formulation of SPH and its practical implementation is remarkably simple. That explains why Eulerian codes evolved naturally from two to three dimensions while SPH codes were written in 3D from the beginning and evolved to 2D later.

Axisymmetric hydrocodes takes advantage of the axial symmetry displayed by many processes in nature. Therefore these codes are able to describe three-dimensional phenomena working within any plane which contains the line of symmetry (see Fig. 1.2). This allows to model full 3D phenomena using a 2D-hydrocode with the subsequent enhancement in resolution (sometimes people refer to them as $2\ \frac{1}{2}$ codes). There are a lot of Eulerian codes written using the axisymmetric hypothesis, many of them of AMR type ([47],[86],[53]). In comparison the number of SPH codes which makes use of that approximation is much lower. Moreover, with very few exceptions ([28],[57],[7]), axisymmetric SPH codes have not been used to study

realistic scenarios in both astrophysics, laboratory of astrophysics and ICF. As a consequence we could said that there is still lacking a formulation of SPH subjected to the axisymmetric hypothesis good enough to be applied to realistic complex scenarios. The main goal of this work is to build and test a coherent axisymmetric SPH scheme which can be applied to model realistic physical processes and can compete with the existing Eulerian codes. The first study carried out using that recently developed code called *AxisSPH* has already been published (see [21]) whereas a preliminary version was used in [84].

Many interesting astrophysical processes can be simulated using a set of hydrodynamic equations termed as Euler equations. These equations come from a restricted lecture of the Navier-Stokes equations of a fluid in the approximation of zero viscosity and zero heat conduction

$$\frac{d\rho}{dt} = -\rho \nabla \cdot \mathbf{v}\,, \tag{1.1}$$

$$\frac{d\mathbf{v}}{dt} = -\frac{\nabla P}{\rho} + \mathbf{g}\,, \tag{1.2}$$

$$\frac{d\mathbf{r}}{dt} = \mathbf{v}\,, \tag{1.3}$$

$$\frac{du}{dt} = -\frac{P}{\rho} \nabla \cdot \mathbf{v}\,, \tag{1.4}$$

where ρ is the density, $\mathbf{r}$ and $\mathbf{v}$ are the position and velocity vectors respectively, u is the internal specific energy, P is the pressure and $\mathbf{g}$ is the gravitational force per unit of mass. In these equations the nature of the coordinate system chosen to describe the hydrodynamics constrains the form in which the ∇ operator is written. For instance, in cylindrical coordinates we preferably write ∇P and $\nabla \cdot \mathbf{v}$ as

$$\nabla P = \frac{\partial P}{\partial r}\widehat{r} + \frac{\partial P}{\partial z}\widehat{z}, \tag{1.5}$$

$$\nabla \cdot \mathbf{v} = \frac{v_r}{r} + \frac{\partial v_r}{\partial r} + \frac{\partial v_z}{\partial z}\,, \tag{1.6}$$

where $r = \sqrt{x^2 + y^2}$. These expressions are basically the same as those obtained using cartesian operators but with the additional term v_r/r in the divergence of velocity. The importance of v_r/r depends on the spatial profile of v_r and is therefore problem dependent.

Given the central role played by density in the formulation of the SPH technique it is of crucial importance to have in mind that two different definitions of density are needed in the axisymmetric approach. First we have the two-dimensional density, η, which is the density estimated using the standard SPH interpolation technique in the plane where the simulation runs

$$\eta = \sum_j m_j W_{ij}(r, z)\,, \tag{1.7}$$

where m_j is the mass of the particle and W_{ij} a weighting function called the kernel (see chapter 2 for a precise explanation of these magnitudes). But, secondly, we also have to compute the value of the three-dimensional density ρ because we need it to calculate the pressure and internal energy of the fluid via the EOS. The usual procedure is to deduce ρ from the calculated value of η using

$$\rho = \frac{\eta}{2\pi r}\,, \tag{1.8}$$

this simple relationship comes from the bizarre nature of particles in the axisymmetric geometry which are not mathematical points but rings or hoops with radius r centered around the z-axis (see Fig. 1.2). Therefore the projection of the mass of one of these 3D-rings (with density ρ) into the 2D-working plane of the simulation directly leads to Eq. 1.8.

Using Eq. 1.8 and neglecting the v_r/r in the SPH equations Herant and Benz [28] studied the growth of hydrodynamical instabilities during the early stages of the explosion of supernova SN1987A in an attempt to understand the unexpected observed high-velocity wings of the iron line.

Nevertheless the v_r/r term must be part of the formulation, being of great importance for imploding systems because of the inverse dependence on the distance to the z-axis. Therefore the axisymmetric hypothesis demands the inclusion of that term in the continuity and energy equations (Eqs. 1.1 and 1.4). But the momentum equation has also to be modified to host a similar term. A 2D particle approaching the z-axis can be understood as a string of particles in 3D which forms a converging hoop. As the hoop shrinks its density rises because the ring surface goes down while its mass remains constant. Then the increase of the pressure by this geometrical

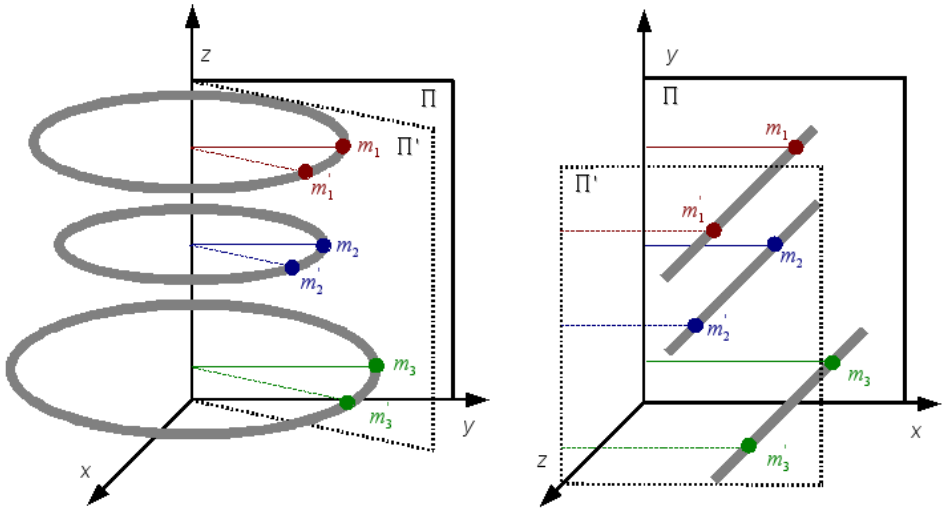

Figure 1.2: Schematic representation of the 2D axisymmetric coordinates (left) and 2D cartesian coordinates (right). A 2D simulation solves a thin film problem of a 3D evolution. In the sketch there are represented three particles m_1,m_2 and m_3 in the plane Π and the same equivalent particles m_1',m_2' and m_3' in the plane Π'. In the axisymmetric approximation all the planes contain the symmetry line (the z-axis) and the particles become 3D loops or hoops. In the cartesian approximation the set of planes are parallel and the particles become slender unlimited cilinders.

mechanism translates to an outward force on the hoop or, equivalently, onto the 2D particle that represents the whole hoop. That force, which is a particular signature of the axisymmetric hypothesis, is usually called the *hoop stress*. Including the hoop stress in the axisymmetric Euler equations not only leads to a much better description of the dynamics but also improves substantially the conservation of the energy. As we will see the hoop stress force is reflected in the r-component of the acceleration equation as a new term $2\pi P/\eta$ ([8],[57]). Notice that the hoop stress can also be a source of numerical troubles because it becomes divergent near the symmetry axis where $\eta \to 0$.

To circumvent the singularity problems introduced by the hoop stress and the v_r/r terms Omang, Borve and Trulsen [54], suggested a different formulation for axisymmetric SPH. They propose to write the Euler equations using standard 2D cartesian coordinates but to change the geometry of the interpolating kernel such as it keeps information about the axisymmetric nature of the simulation. Therefore

in Omang et al. formulation the Euler equations remain simple but the geometrical complexity of interpolations increases. The scheme of Omang et al. has the practical inconvenient that several elliptical integrals have to be computed numerically for each particle at each time step.

In this thesis we extend the formulation of Brookshaw [8] for axisymmetric SPH but incorporating analytical correction functions to avoid divergence problems in the hoop stress related terms when particles move close to the singularity z-axis. These correction terms were obtained from reasonable physical and geometrical statements and are straightforward to implement with no penalty in computer time (see Sec. 2.3, 2.4 and 2.6). Additionally we have also improved many pieces of physics which are necessary to apply the method to solve problems in the real world. Among them we have developed a more exact expression for heat conductive transport, we have completed the artificial viscosity formalism with a hoop-stress related term (never taken into account before) and devised a novel scheme to implement gravity in the calculations [24]. Other minor contributions will be also highlighted as the reading of text progresses.

Hot plasmas with high temperature gradients efficiently conduct or diffuse heat because of the large conductivity and diffusivity coefficients typical of the interior of the stars or in ICF experiments. In particular conductive heat transport demands a new term in the energy equation, (Eq. 1.4)

$$\left(\frac{du}{dt}\right)_{cond} = \frac{1}{\rho}\nabla\cdot(\kappa\nabla T)\,, \tag{1.9}$$

where κ is the conductivity coefficient, often a complex function of the thermodynamic variables and chemical composition. In the axisymmetric approach the divergence of the temperature gradient must also contain geometric corrections in the same line as the divergence of velocity. Our approach (see Sec. 2.7) to the conduction term includes, for first time, these corrections that are especially relevant when the heat flux takes place in the axis neighborhood. On another note the correct implementation of that term could also be of interest to smooth the excess of internal energy which appears during the so called *wall shock conditions*, that is during the supersonic impact of streams of gas. Wall shock conditions are not rare in axisymmetric geometry because many problems of interest which follows that geometry involve strong convergent fluxes of plasma (ICF, stellar collapse, several

types of jets).

The use of the artificial viscosity formulation in SPH is needed to handle with shocks and also to stabilize the scheme by limiting the level of numerical noise. In this work we have implemented the standard recipe of Monaghan [42] for the cartesian part of the gradient of viscous pressure. Nevertheless a coherent formulation of artificial viscosity in the axisymmetric paradigm demands again the inclusion of a new term $\propto v_r/r$ arising from cylindrical geometry. The ability of the complete formulation, given in Sec. 2.9, to handle with strong converging shocks has been demonstrated in many simulations described in different chapters of this thesis.

Self gravity is of course not important in ICF or Laboratory Astrophysics but it can not be neglected in many astrophysical situations. Being a long range force the major difficulty to obtain the gravitational force acting on a particle belonging to a system of N particles is that the number of calculations scales as N^2. In standard 3D SPH gravity is often obtained by combining the multipolar expansion of the gravitational force with the hierarchical organization of the particle sample in clusters of particles of different size. These hierarchical tree methods (Hernquist and Katz [29]) reduces the computational overload to $NlogN$. Unfortunately the ring-like nature of particles in axisymmetric geometry precludes the application of hierarchical tree methods to this case. We have developed a novel and practical procedure to compute gravity by direct particle to particle interaction (see Sec. 2.10). The task is not straightforward, however, because particles are in fact rings of different size which have to be taken into account to describe the interaction. Although the computational overload of the algorithm scales as $\propto N^2$ the calculation is affordable because the relatively low number of particles required in 2D to carry out simulations with good accuracy. Moreover a modified scheme which uses the gravitational potential to calculate the force has also been developed which reduces the computational overload. Several test specifically addressed to check the gravitational module of the code are given in Subsec. 2.10.3 and Sec. 3.5.

The basic tests devised to check the behavior and consistency of the hydrocode have been completed with three more realistic applications taken from different fields of the physics. The goal of these applications is to validate the code in real scenarios where there are present hydrodynamic instabilities (stagnation phase of a ICF capsule), strong shocks (chapter devoted to jets) and complex physics (head on collision of two white dwarfs).

In the first complex application we have carried out a simulation of the stagnation phase of the implosion of a ICF pellet using the same initial conditions as in Sakagami and Nishihara [70]. Although the calculation is still far from the state of art of today numerical simulations it contains worthy pieces of physics such as a more complete equation of state consisting in ions, electrons treated as a partially degenerated gas and radiation. The conductive heat transport was also incorporated. In these simulations we were able to measure the growth rate of the Rayleigh-Taylor instabilities for different wavenumbers.

Collision of supersonic flows of gases, fluids or solids can produce collimated jets, an ubiquitous phenomenon present in many fields of physics, astrophysics and engineering. In the second application we analyze the capability of the proposed axisymmetric SPH code to handle with jets. We report on several simulations of jets born after the geometrical convergence of two conical streams of gas onto the symmetry axis. The results of the tests have been compared to the theoretical model developed by Cantó et al. [11]. Depending on the angle of incidence of the converging flows one or two jets can be observed. For small angles of incidence only one jet appears but above a critical angle θ_c it is possible to have two jets moving along the z-axis in opposite directions. The value of θ_c obtained in our simulations and the general behaviour of the jets is in reasonable agreement with the analytical theory. In addition we have been able to qualitatively reproduce the structure of jets born from the collision of metallic plates using a stiffened gas equation of state.

Finally we present an astrophysical application, the head on collision of two white dwarf stars, which incorporates a good deal of physics. Nowadays this simulation is of considerable interests because the collision of two white dwarfs has been recently invoked as a potential mechanism to explain the origin of some Type Ia supernova explosions ([69],[64]). All simulations done so far were carried out using three dimensional SPH hydrodynamics [63] with limited resolution. However an interesting extreme case can be studied using axisymmetric hydrodynamics: the head on collision of two white dwarfs, and the results compared with a full 3D-SPH simulation to seek for convergence. For this particular calculation we have chosen a couple of $0.7M_{\odot}$+$0.7M_{\odot}$ white dwarfs whose total mass just equals the Chandrasekhar-mass limit. The included physics consists of gravity, a complex EOS (ions with Coulomb corrections, partially-relativistic partially-degenerate electrons and radiation) and nuclear reactions involving a nuclear network of 14 species from helium to zinc. As shown in Sec. 4.3 the axisymmetric SPH is able to successfully cope with this sce-

nario, providing interesting information concerning various observables such as the kinetic energy of the explosion and the approximate chemical composition of the ejected material.

The material included in this work is organized as follows. In Chapter 2 we deduce and write the basic Euler equations in the axisymmetric paradig (they are summarized in Sec. 3.1). In this chapter there is also a lot of discussion concerning the implementation of the necessary physics needed to carry out meaningful realistic simulations (heat conduction, shock handling, gravity). Chapter 3 is devoted to describe and discuss five basic tests aimed at validating the axisymmetric scheme. Three complex applications involving very different scenarios (ICF, jets, and the collision and explosion of twin white dwarfs) are presented in Chapter 4 . Finally, the main conclusions of this thesis as well as the principal lines of future work are outlined in Chapter 5. Additional information concerning technical details of the implementation of the code can be found in the two Appendices at the final pages of the manuscript.

Chapter 2

Axisymmetric SPH

Many times it is possible to assume that the phenomenon to be studied has cylindrical symmetry and use a 2D axisymmetric code to simulate the hydrodynamical evolution of the system. A variety of axisymmetric codes have been successfully used to simulate astrophysical phenomena such accretion discs, rotating stars, and explosive episodes like novae o supernovae (see for example [77], [38]). In inertial confinement fusion scenarios they have been used to study direct-drive implosions, and also in the so called fast ignition provided the heating laser goes along the symmetry axis (see for example [79], [4], [81], [85]).

Although it is very easy to reduce a 3D Cartesian SPH code to a 2D Cartesian SPH code, the resulting nature of the particles (infinite cylinders) is very difficult to conciliate to real astrophysical scenarios. Thus if we want to improve the resolution, changing the dependence of this magnitude from the cube root to a square root of the number of interpolation points, the best solution is to implement a 2D SPH axisymmetric code.

2.1 3D SPH

Before explaining our 2D SPH code in the axisymmetric version, we first review the basic formalism of the SPH technique, a method that was designed from its origins to work in three dimensions by Lucy [37] and Gingold and Monaghan [25] in 1977.

SPH is a gridless lagrangian method, initially introduced in astrophysical simulations to study gas dynamical processes involving large deformations of the bodies, and important spatial changes of physical magnitudes. The gridless nature of SPH avoids the problems associated with mesh tangling and distortion. It is easy to reproduce scenarios with void spaces, or without boundary limits avoiding the waste of unnecessary mesh points. On the other hand, the mathematical formalism of 3D-SPH is conceptually much simpler than grid based methods.

In SPH method the fluid is divided into a sample of N mass points m_j, usually called *particles* that move according to the hydrodynamic equations. Any continuum property of the fluid, $A(\mathbf{r})$, function of the position $\mathbf{r}$, is reconstructed at every step of time, by means of an interpolation procedure

$$A(\mathbf{r}) = \int A(\mathbf{r}')\delta(|\mathbf{r}' - \mathbf{r}|)d\mathbf{r}' \,, \tag{2.1}$$

where δ refers to the Dirac delta function.

For numerical calculations the integral of Eq. 2.1 can be approximated by the summation

$$A_i(\mathbf{r}) = \sum_j^N \frac{m_j}{\rho_j} A_j(\mathbf{r}) W(\mathbf{r}_{ij}, h) \,, \tag{2.2}$$

where m_j and ρ_j are the mass and the density of particle j. The Dirac delta is substituted by a smooth function, $W(\mathbf{r}_{ij}, h)$ called the interpolator kernel with $\mathbf{r}_{ij} \equiv |\mathbf{r}_i - \mathbf{r}_j|$ and h is the spatial range of the interpolator, known as the smoothing-length parameter. Two properties have to be demanded to the interpolating kernel

$$\lim_{h\to 0} W(\mathbf{r}' - \mathbf{r}, h) = \delta(\mathbf{r}' - \mathbf{r}) \,, \tag{2.3}$$

$$\int W(\mathbf{r}' - \mathbf{r}, h)d\mathbf{r}' = 1 \,, \tag{2.4}$$

the first one implies that the kernel must reproduce a Dirac delta function when $h \to 0$ and the second is a normalization condition. There is a wide family of interpolator kernels, for example the Gaussian kernel

$$W(\mathbf{r}_{ij}, h) = \frac{1}{(\sqrt{\pi}h)^3} e^{-\left(\frac{\mathbf{r}'-\mathbf{r}}{h}\right)^2}, \tag{2.5}$$

but probably the most used kernel in the SPH technique is the cubic spline kernel which was initially applied to SPH calculations by Monaghan and Lattanzio [46]

$$W(v,h) = \frac{K}{h^d} \begin{cases} 1 - \frac{3}{2}v^2 + \frac{3}{4}v^3 & 0 \leq v \leq 1 \\ \frac{1}{4}(2-v)^3 & 1 < v \leq 2 \\ 0 & v > 2 \end{cases}, \tag{2.6}$$

where $v = r_{ij}/h$ is a dimensionless distance scaled over the smoothing length, and d is the number of dimensions. $K = \frac{2}{3}$, $\frac{10}{7\pi}$ and $\frac{1}{\pi}$ for one, two and three dimensions respectively. The polynomial nature of this kernel makes it computationally efficient. Another important advantage is that the kernel becomes zero for distances between particles larger than two times the smoothing-length parameter, so the contribution to summations in Eq. 2.2 is reduced from the total number of particles N to a discrete sample of the nearest points, usually called *neighbors particles*.

Therefore an important feature of any SPH code is to include an efficient algorithm to find the neighbors of a given particle. A method that has been widely used to perform this task, and the one we have used in our code, was developed by Hernquist and Katz [29] being based on a hierarchical tree structure.

Although the early SPH simulations used a fixed smoothed-length for all particles, it is more accurate to use a variable smoothing length for each particle at each time step, $h = h(\mathbf{r}, t)$. If a constant value of h is used, isolated particles could have not enough interpolator points and the large number of interpolator particles in zones of high density would smooth the magnitudes in excess. In practice, the procedure to find the value of h for each particle is to choose a constant number of neighbors particles, so that when the density rises, h becomes smaller (see Fig. 2.1). For that reason h is a good parameter to estimate resolution.

In order to improve the results in some situations, as for example when there are intense shocks, several alternative kernels have been proposed. For example Owen et al. [56] used kernels that change the domain from a sphere to an ellipsoid with the minor axis oriented in the shock direction. Recently we proposed

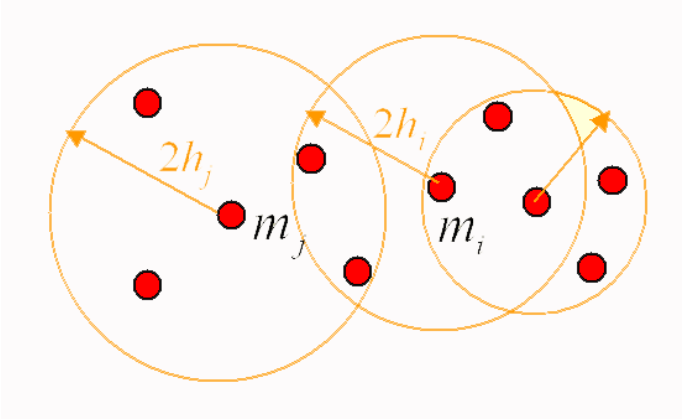

Figure 2.1: Schematic representation of the particles m_i and m_j and its neighbors particles, each particle has the same number of neighbors, thus when the density is larger, the radius $2h$ is lesser.

[10] a one-parameter family of interpolating kernels, with compact support based on harmonic-like functions that covers the whole range of kernels in a continuous manner by simply varying a leading parameter in the adaptive kernels. The shape of the harmonic kernel range from more extend to more centrally condensed profiles as the parameter n increases in order to enhance the local resolution when necessary. The family of interpolators $W_n^H(v,h)$ is written

$$W_n^H(v,h) = \frac{B_n}{h^2}\begin{cases} 1 & v = 0 \\ \left(\frac{\sin\left[\frac{\pi}{2}v\right]}{\frac{\pi}{2}v}\right)^n & 0 < v \leq 2 \\ 0 & v > 2 \end{cases}, \tag{2.7}$$

where B_n is a normalization factor. The parameter n can be dynamically modified during the simulation as a function of hydrodynamic local properties (see the Appendix B for details). We have used $W_n^H(v,h)$ in some applications of Chapter 4.

In SPH the continuity equation takes a particularly simple form putting $A_i(\mathbf{r}) = \rho_i$ into the summation interpolation equation Eq. 2.2

$$\rho_i = \sum_j^N m_j W_{ij}\,, \tag{2.8}$$

where $W_{ij} \equiv W(\mathbf{r}_{ij}, h)$. This equation conserves mass exactly.

One powerful feature of SPH relies in its simplicity for calculating the fist derivatives of any magnitude A_i because the derivative acts on the kernel, which is a differentiable function, and not on the grid as in other methods.

$$\frac{\partial A_i}{\partial x_i} = \sum_j^N m_j \frac{A_j}{\rho_j} \frac{\partial W_{ij}}{\partial x_i} \,. \tag{2.9}$$

However, it is possible to build other expressions for the derivative (see [45]) using the following identity

$$\frac{\partial A}{\partial x} = \frac{1}{\Phi} \left(\frac{\partial (\Phi A)}{\partial x} - A \frac{\partial \Phi}{\partial x} \right) \,, \tag{2.10}$$

which, for $\Phi = 1$ and $\Phi = \rho$ leads to

$$\frac{\partial A_i}{\partial x_i} = \sum_j^N \frac{m_j}{\rho_j} (A_j - A_i) \frac{\partial W_{ij}}{\partial x_i} \,, \tag{2.11}$$

$$\frac{\partial A_i}{\partial x_i} = \frac{1}{\rho_i} \sum_j^N m_j (A_j - A_i) \frac{\partial W_{ij}}{\partial x_i} \,. \tag{2.12}$$

The Euler equation in absence of gravity

$$\frac{d\mathbf{v}}{dt} = -\frac{\nabla P}{\rho} \,, \tag{2.13}$$

can be translated in SPH formalism using Eq. 2.9, 2.11 or 2.12, but it is more useful to consider the following identity

$$\frac{\nabla P}{\rho} = \nabla \left(\frac{P}{\rho} \right) + \frac{P}{\rho^2} \nabla \rho \,, \tag{2.14}$$

therefore, using Eq. 2.9 we can express the momentum equation as

$$\frac{d\mathbf{v}_i}{dt} = -\sum_j^N m_j \left(\frac{P_i}{\rho_i^2} + \frac{P_j}{\rho_j^2} \right) \nabla_i W_{ij} \,, \tag{2.15}$$

where $\nabla_i W_{ij}$ denotes the gradient of W_{ij} with respect to the coordinates of particle i and with perfect linear and angular momentum conservation because the forces between particles i and j are equal and opposite.

The energy equation can be derived from the first law of thermodynamics in an isolated system

$$\frac{du}{dt} = -P\frac{dV}{dt} = \frac{P}{\rho^2}\frac{d\rho}{dt} \,, \tag{2.16}$$

where u refers to the specific internal energy. Using the continuity equation

$$\frac{d\rho}{dt} = -\rho \nabla \cdot \mathbf{v} \,, \tag{2.17}$$

the energy equation can be expressed as

$$\frac{du}{dt} = -\frac{P}{\rho} \nabla \cdot \mathbf{v} \,, \tag{2.18}$$

the translation of this equation to SPH can be done in different ways. For example, using the Eq. 2.12 for each component of the divergence of the velocity

$$\frac{du_i}{dt} = \frac{P_i}{\rho_i^2} \sum_j^N m_j \mathbf{v}_{ij} \cdot \nabla_i W_{ij} \,, \tag{2.19}$$

were $\mathbf{v}_{ij} \equiv \mathbf{v}_i - \mathbf{v}_j$. Again we make use of the following identity

$$\frac{P}{\rho} \nabla \cdot \mathbf{v} = \nabla \cdot \left(\frac{P}{\rho} \mathbf{v} \right) - \mathbf{v} \cdot \nabla \left(\frac{P}{\rho} \right) \,, \tag{2.20}$$

to derive a second expression for the energy equation

$$\frac{du_i}{dt} = \sum_j^N m_j \frac{P_j}{\rho_j^2} \mathbf{v}_{ij} \cdot \nabla_i W_{ij} \,. \tag{2.21}$$

Finally, it is possible to obtain a symmetric version of the energy equation by taking the average of Eq. 2.19 and Eq. 2.21

$$\frac{du_i}{dt} = \frac{1}{2} \sum_j^N m_j \left(\frac{P_i}{\rho_i^2} + \frac{P_j}{\rho_j^2} \right) \mathbf{v}_{ij} \cdot \nabla_i W_{ij} \,. \tag{2.22}$$

In SPH, however, hydrodynamic equations have to include some sort of viscosity, to avoid unphysical oscillations which appear downstream of shocks. In this respect, several different formulations can be used, but one commonly used (see [45]) is to add an artificial viscosity term Π_{ij} to the momentum and energy equations (Eq. 2.15 and Eq. 2.22) in the following manner

$$\frac{d\mathbf{v}_i}{dt} = -\sum_j^N m_j \left(\frac{P_i}{\rho_i^2} + \frac{P_j}{\rho_j^2} + \Pi_{ij} \right) \nabla_i W_{ij} \,, \tag{2.23}$$

$$\frac{du_i}{dt} = \frac{1}{2} \sum_j^N m_j \left(\frac{P_i}{\rho_i^2} + \frac{P_j}{\rho_j^2} + \Pi_{ij} \right) \mathbf{v}_{ij} \cdot \nabla_i W_{ij} \,, \tag{2.24}$$

this new term is evaluated as

$$\Pi_{ij} = \begin{cases} \frac{\alpha \bar{c} \mu_{ij} + \beta \mu_{ij}^2}{\bar{\rho}_{ij}} & \text{if } \mathbf{v}_{ij} \cdot \mathbf{r}_{ij} < 0 \,, \\ 0 & \text{if } \mathbf{v}_{ij} \cdot \mathbf{r}_{ij} \geq 0 \,, \end{cases} \tag{2.25}$$

and

$$\mu_{ij} = \frac{\bar{h}_{ij} \mathbf{v}_{ij} \cdot \mathbf{r}_{ij}}{\mathbf{r}_{ij}^2 + \nu^2} \,, \tag{2.26}$$

where $\bar{h}_{ij} = \frac{1}{2}(h_i + h_j)$, $\bar{\rho}_{ij} = \frac{1}{2}(\rho_i + \rho_j)$ and $\bar{c}_{ij} = \frac{1}{2}(c_i + c_j)$ are the averaged smoothing length, density and speed of sound between particle i and its neighbor j

respectively. The linear part of μ_{ij} represents a bulk viscosity while the quadratic one is the von Neumann-Ritchmeyer viscosity, which prevents particle interpenetration in collisions with high Mach number. The $\nu = 0.1\bar{h}_{ij}$ helps to avoid divergences when $\mathbf{r}_{ij} \to 0$ (see Sec. 2.9 for more details).

2.2 Axisymmetric SPH: existing formulations

Since the first applications, (see [37] and [25]) SPH codes have been preferently used to solve 3D problems in physics and engineering. However the first attempts to work with a consistent 2D-axisymmetric SPH method [28] began around 1990.

In these approximations the equations were based on the standard Cartesian kernel function (the spline kernel, see Eq. 2.6) renormalized by a factor $1/(2\pi r)$, which is needed to transform the 2D density η (the "natural" density in a 2D distribution of points) in a 3D density ρ (the "real" density, with "real" meaning for example that used to compute EOS). The hydrodynamic SPH equations given by Eq. 2.2, Eq. 2.8, Eq. 2.23 and Eq. 2.24 can be translated to their axisymmetric form. They can be found in the Appendix B of [28] are

$$< A > = \sum_{j=1}^{N} m_j \frac{A_j}{\eta_j} W_{ij} \,, \tag{2.27}$$

$$\eta_i = \sum_{j=1}^{N} m_j W_{ij} \,, \tag{2.28}$$

$$\frac{d\mathbf{v}}{dt} = -\sum_{j=1}^{N} \frac{m_j}{2\pi r_j} \left[\frac{P_i}{\rho_i^2} + \frac{P_j}{\rho_j^2} + \Pi_{ij} \right] \nabla W_{ij} \,, \tag{2.29}$$

$$\begin{aligned} \frac{du_i}{dt} = & \frac{P_i}{\rho_i^2} \sum_{j=1}^{N} m_j \left(\frac{\mathbf{v}_i}{2\pi r_i} - \frac{\mathbf{v}_j}{2\pi r_j} \right) \cdot \nabla W_{ij} \\ & + \frac{1}{2} \sum_{j=1}^{N} m_j \Pi_{ij} \left(\frac{\mathbf{v}_i}{2\pi r_j} - \frac{\mathbf{v}_j}{2\pi r_i} \right) \cdot \nabla W_{ij}. \end{aligned} \tag{2.30}$$

for an interpolated function $A(\mathbf{s})$, and for mass, momentum and energy conservation. Benz and Herant [28] use this approach to simulate the Rayleigh-Taylor instabilities of the postexplosion of a supernova (SN 1987A).

The most important difficulty in the expressions above is that they involve the factor $1/(2\pi r)$ which becomes singular in the proximity of the z-axis, when $r \rightarrow 0$. To avoid this situation they only modelled a 60° wedge with periodic boundary conditions, therefore reducing the number of particles close to the z-axis.

A good attempt to improve the above formulation was proposed by Petschek and Libersky in 1993 [57]. In their paper they start from a three dimensional Cartesian representation of SPH. After integrating the angular component they present a coherent description in cylindrical coordinates where particles were treated as if they were a torus. The deduction was extended to include the entire stress tensor. Unfortunately, the formulation was only able to work with a Gaussian interpolation kernel (Eq. 2.5) with an arbitrary cut-off at finite range. The method included the hoop stress and therefore was able to handle with the z-axis but still it had some difficulties to solve impact problems such as the well known wall shock problem [52].

In year 2005, Omang, Børve & Trulsen proposed a new kernel function adapted for cylindrically symmetric problems in the context of SPH, and derived the modified equations of motion using the Lagrangian formalism (see [55]). They obtained satisfactory results in test problems that need good resolution near the z-axis, as for example the Noh infinite shock problem. The underlying problem of that approach is the numerical difficulty (in terms of computational speed) of calculating elliptical integrals at each integration step and for each particle, that are needed to evaluate this new kernel function W_{3C2}

$$W_{3C2}(r', z', r, z; h) = 4 \int_0^{arcsin(min(1, \sqrt{(4-A)/B}))} W_{CS3}(\sqrt{(4 + Bsin^2 \upsilon)}) d\upsilon \,, \qquad (2.31)$$

where $A = ((z' - z)^2 + (r' - r)^2/h^2$, $B = 4r'r7h^2$ and W_{CS3} represents the B-spline function in three dimensional space (the cubic-spline). The equations of motion derived using this formulation are

$$\rho_i = \sum_{j=1}^{N} m_j W_{3C2}\,, \tag{2.32}$$

$$\frac{d\mathbf{v}}{dt} = -\sum_{j=1}^{N} m_j \left[\frac{P_j}{\rho_j^2} + \frac{P_i}{\rho_i^2} + \Pi_{ij}\right] \mathbf{D}_i W_{3C2}\,, \tag{2.33}$$

$$\frac{du_i}{dt} = \sum_{j=1}^{N} m_j \left(\frac{P_i}{\rho_i^2} + \frac{1}{2}\Pi_{ij}\right) \left(v_{rj}\frac{\partial}{\partial r_j} + v_{ri}\frac{\partial}{\partial r_i} + v_{zi}\frac{\partial}{\partial z_i}\right) W_{3C2}\,, \tag{2.34}$$

where $\mathbf{D}_i = \left(\frac{\partial}{\partial r_i}, \frac{\partial}{\partial z_i}\right)$. Later on the same authors improved the formalism using an alternative generic kernel (called W_{A3C}) with analytical solutions (see [54]).

We have also to mention the contribution made by Leigh Brookshaw in 2003, who derived the axisymmetric SPH equations from the minimal action principle. He showed how the hoop-stress terms appear naturally from the relationship between the 2D and 3D densities, $\eta = 2\pi r\rho$.

The corresponding equations are

$$\eta_i = \sum_{j=1}^{N} m_j W_{ij}\,, \tag{2.35}$$

$$\ddot{r}_i = 2\pi\frac{P_i}{\eta_i} - 2\pi\sum_{j=1}^{N}\left[m_j\left(\frac{P_i r_i}{\eta_i^2} + \frac{P_j r_j}{\eta_j^2}\right)\frac{\partial W_{ij}}{\partial r_i}\right]\,, \tag{2.36}$$

$$\ddot{z}_i = -2\pi\sum_{j=1}^{N} m_j\left(\frac{P_i r_i}{{\eta_i}^2} + \frac{P_j r_j}{{\eta_j}^2}\right)\frac{\partial W_{ij}}{\partial z_i}\,, \tag{2.37}$$

$$\frac{du_i}{dt} = -2\pi\frac{P_i\ v_{r_i}}{\eta_i} + 2\pi\frac{P_i\ r_i}{\eta_i^2}\sum_{j=1}^{N} m_j(\mathbf{v_i} - \mathbf{v_j})\cdot\mathbf{D}_i\ W_{ij}\,, \tag{2.38}$$

where $\mathbf{s} = (r, z)$ are the cylindrical coordinates treated as if they were cartesian and $W(\mathbf{s} - \mathbf{s}'; h)$ is the cartesian interpolating kernel. The proposal of Brookshaw was easier to be implemented but again it was difficult to handle points in the vicinity of the line of symmetry when $r \to 0$.

2.3 Approximating the density

Given the difficulties of the above schemes to correctly represent the gas dynamics in axis converging flows we have derived a new formalism which preserves many of the virtues but avoids the disadvantages of these methods. Firstly, in our scheme it is not necessary to modify the interpolation kernel as in Omang et al. Therefore it is possible to use any of the existing kernels. We have used mainly the cubic spline kernel as well as the adaptive kernel (Eq. 2.7) proposed by Cabezón et al. [10]. But it would be also possible to make use of other kernels, as for example, elliptic kernels (see [56]).

Another important feature of our approximation is the use of reflective particles. That is, each ring is divided in two identical parts, one moves with the radial coordinate $r > 0$ and the other, the symmetric one (denoted by a s superindex) moves as the specular image of the first

$$\begin{aligned} r^s &= -r\,, \\ z^s &= z\,, \\ m^s &= m\,, \\ v_r^s &= -v_r\,, \\ v_z^s &= v_z\,. \end{aligned} \tag{2.39}$$

Notice that only those symmetric particles moving near the z-axis at distance lesser than 2h are relevant to the calculation of the density. In this case the particle can have neighbors with $r > 0$ and $r < 0$. This method avoids the underestimation of the neighbors particles located near the z-axis. Using this scheme we have a continuous and isotropic distribution of particles when $r \to 0$.

The addition of these particles is complemented with a correction factor f_1 that only affects particles moving at a distance lesser than $2h$ from the z-axis. This factor reduces the value of η_i when $\zeta_i = \frac{r_i}{h_i} \leq 2$ to ensure that $\eta \to 0$ when $r \to 0$. In the following section (Sec. 2.4) we show that the corrected density $\widehat{\eta}_i$ can be written as

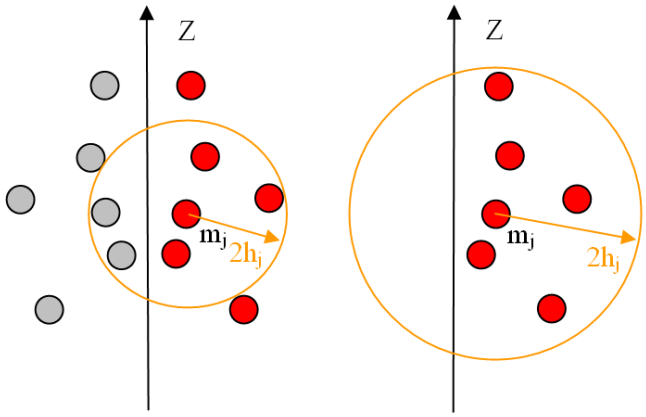

Figure 2.2: Schematic representations of the particle m_j and its neighbors particles. In the first sketch some neighbors particles have $r < 0$ while in the second one all neighbors are "real" particles which leads to a larger value of h_j and an anisotropic distribution of the density near the z-axis.

$$\widehat{\eta}_i = \sum_{j=1}^{N} m_j W_{ij} \times f_1^i = \eta_i \times f_1^i \,. \tag{2.40}$$

The expression of f_1^i for the cubic spline kernel (Eq. 2.6) is

$$f_1^i(\zeta) = \begin{cases} \left[\frac{7}{15}\zeta_i^{-1} + \frac{2}{3}\zeta_i - \frac{1}{6}\zeta_i^3 + \frac{1}{20}\zeta_i^4\right]^{-1} & \text{if } 0 < \zeta_i < 1 \\ \left[\frac{8}{15}\zeta_i^{-1} - \frac{1}{3} + \frac{4}{3}\zeta_i - \frac{2}{3}\zeta_i^2 + \frac{1}{6}\zeta_i^3 - \frac{1}{60}\zeta_i^4\right]^{-1} & \text{if } 1 < \zeta_i < 2 \\ 1 & \text{if } \zeta_i > 2 \end{cases} . \tag{2.41}$$

A plot of the function $f_1^i(\zeta)$ can be seen in Fig. 2.6.

At this point it is useful to introduce a couple of algebraic rules

$$\widehat{A}_i = \sum_j m_j \frac{A_j}{\widehat{\eta}_j} W_{ij} \,, \tag{2.42}$$

$$\widehat{\eta A}_i = f_1^i \sum_j m_j A_j W_{ij} \,, \tag{2.43}$$

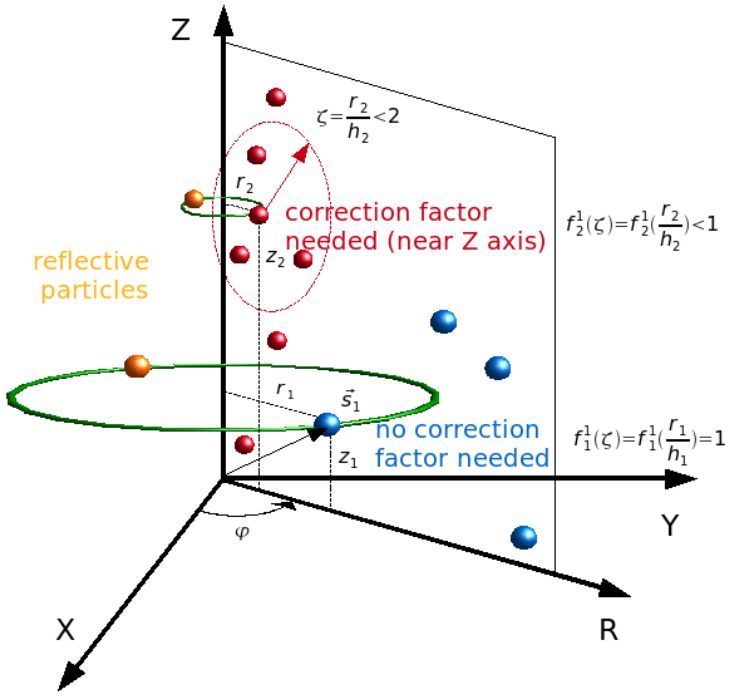

Figure 2.3: Sketch of our 2D axisymmetric approximation. The green ring represents the real nature of a particle in cylindrical axisymmetric coordinates. The ring is "splitted" in two semicircumferences. The first is in the plane Z-R and the second represents the reflected particle (yellow particle). Also it is denoted in red those particles that need a correction factor (near the z-axis, $\zeta < 2$) and the uncorrected particles because $\zeta > 2$ (blue particles).

which are valid as long as the magnitude A has a weak dependence in the r-coordinate in the axis vicinity. In particular, setting $A = 1$ in equation Eq. 2.43 leads to Eq. 2.40.

2.4 Calculation of the correction factor f_1^i for the density

In axisymmetric SPH, the interpolation particles are rings centered in the z-axis. The relation between the real 3D density ρ and the 2D density η, is

$$\rho_i = \frac{\eta_i}{2\pi r_i}, \tag{2.44}$$

so taking $r_i \to 0$ may give rise to singularity problems near the z-axis.

We start taking a linear expansion of the 3D density ρ for particles near the z-axis where $r \to 0$:

$$\rho(r', z') = \rho(0, z) + \left(\frac{\partial \rho}{\partial r'}\right)_{r'=0} (r' - 0) + \left(\frac{\partial \rho}{\partial z'}\right)_{z'=z} (z' - z)\,, \tag{2.45}$$

due to the symmetry around the z-axis (ρ is a even function) we have

$$\left(\frac{\partial \rho}{\partial r'}\right)_{r'=0} = 0\,, \tag{2.46}$$

so we can write

$$\rho(r', z') = \rho(0, z) + \left(\frac{\partial \rho}{\partial z'}\right)_{z'=z} (z' - z) \simeq \rho(z')\,, \tag{2.47}$$

On the other hand, the SPH estimation of any magnitude A in 2D is

$$< A(\mathbf{s}) >= \int_{2D} A(\mathbf{s}') W^{2D}(\frac{|s - s'|}{h}) d\mathbf{s}'\,, \tag{2.48}$$

where $\mathbf{s} = (r, z)$ is the position vector in cylindrical coordinates and $W^{2D}(\frac{|s-s'|}{h})$ is the interpolating kernel. Taking $A(\mathbf{s}) = \eta(r, z)$ and using Eq. 2.44 we have

$$< \eta(r,z) >= \int_{-\infty}^{\infty}\int_{-\infty}^{\infty} 2\pi|r'|\rho(r',z')W^{2D}(\frac{|s-s'|}{h})dr'dz' \,. \tag{2.49}$$

Hereafter we denote $< \eta(r,z) >$ simply by η. To compute the 2D density we select an interpolation kernel that can be expressed as a product of two functions depending on only one variable, thus it is possible to write

$$W^{2D}\left(\frac{|s-s'|}{h}\right) = K^{2D}W_r(u_r)W_z(u_z)\,, \tag{2.50}$$

where K^{2D} is the normalization constant of the kernel in two dimensions, $u_r = \frac{|r-r'|}{h}$ and $u_z = \frac{|z-z'|}{h}$. These features are fulfilled by the Gaussian Kernel

$$W^{2D}\left(\frac{|s-s'|}{h}\right)_{gausian} = K^{2D}\exp\frac{-|r-r'|^2}{h^2}\exp\frac{-|z-z'|^2}{h^2}\,. \tag{2.51}$$

Using the approximation given by Eq. 2.47 for particles near the z-axis the Eq. 2.49 is written as

$$\begin{aligned}\eta &= \int_{-\infty}^{\infty}\rho(z')W_z(u_z)dz' \int_{-\infty}^{\infty} 2\pi|r'|W_r(u_r)dr' \\ &= \frac{K^{2D}}{K^{1D}}\cdot\left(K^{1D}\int_{-\infty}^{\infty}\rho(z')W_z(u_z)dz'\right)\cdot\int_{-\infty}^{\infty}2\pi|r'|W_r(u_r)dr'\,,\end{aligned} \tag{2.52}$$

where the expression inside the parenthesis represents $\rho(z)$.

It is well known that for the Gaussian kernel the relation between the normalization constants is

$$\frac{K_G^{2D}}{K_G^{1D}} = \frac{(\sqrt{\pi}h)^2}{\sqrt{\pi}h} = K_G^{1D}\,, \tag{2.53}$$

and for the cubic spline

$$\frac{K_s^{2D}}{K_s^{1D}} = \frac{\frac{10\cdot h^2}{7\pi}}{\frac{2\cdot h}{3}} = \frac{15h}{7\cdot\pi} \simeq K_s^{1D}\,, \tag{2.54}$$

with a difference around 2-3 % from K_s^{1D}.

Thus with a reasonable accuracy Eq. 2.52 can be expressed as follows

$$\begin{aligned}\eta &= 2\pi K^{1D}\rho(z)\int_{-\infty}^{\infty}|r'|W_r(u_r)dr' \\ &= \eta(z)\cdot\left(\frac{K^{1D}}{|r|}\int_{-\infty}^{\infty}|r'|W_r(u_r)dr'\right)\,,\end{aligned} \tag{2.55}$$

defining a new variable $\zeta = r/h$ the expression inside the parenthesis can be considered a function $f_1(\zeta)$ that can be calculated analytically. Thus finally we express Eq. 2.55 as

$$\eta = \frac{\widehat{\eta}}{f_1(\zeta)}\,, \tag{2.56}$$

where $\widehat{\eta} = 2\pi r\rho(z)$ is the corrected two-dimensional density. Hereafter a hat over any magnitude represents the corrected quantity. The brackets of any magnitude, as for example, the two-dimensional density $<\eta(r,z)>$ is calculated in the standard way of SPH. Implementing the integral as a summation over the neighbors particles we get the following expression

$$\widehat{\eta}_i = f_1^i(\zeta)\cdot\sum_{j=1}^{N} m_j W(|\mathbf{s_i}-\mathbf{s_j}|,h_i)\,. \tag{2.57}$$

Finally it is necessary to know the analytical expression of the function $f_1(\zeta)$, that can be obtained from its definition Eq. 2.55

$$\frac{1}{f_1(\zeta)} = \frac{K^{1D}}{|r|}\int_{-\infty}^{\infty}|r'|W_r(u_r)dr'\,. \tag{2.58}$$

INTEGRATION LIMITS	$\lvert r'\rvert$	$\lvert r-r'\rvert$	$W_r(u_r)$
$(r-2h, r-h)$	$-r'$	$r-r'$	W_b
$(r-h, 0)$	$-r'$	$r-r'$	W_a
$(0, r)$	r'	$r-r'$	W_a
$(r, r+h)$	r'	$r'-r$	W_a
$(r+h, r+2h)$	r'	$r'-r$	W_b

Table 2.1: Integration intervals, and interpolation functions when $0 < \frac{r}{h} < 1$ needed to calculate f_1 in Eq. 2.58. W_a and W_b are defined in Eq. 2.61 and Eq. 2.62. See also Fig. 2.4.

Because its simplicity and efficiency an useful choice for $W_r(u_r)$ is the cubic-spline kernel in 1D

$$W_r(u_r) = \frac{2}{3h}\begin{cases} 1-\frac{3}{2}u_r^2+\frac{3}{4}u_r^3 & 0 \le u_r \le 1 \\ \frac{1}{4}(2-u_r)^3 & 1 < u_r \le 2 \\ 0 & v > 2 \end{cases} . \tag{2.59}$$

Notice that to evaluate the integral of Eq. 2.58, the dependence of the kernel on the absolute value of the distance $|r-r'|$

$$W_r(u_r) = W_r\left(\frac{|r-r'|}{h}\right) , \tag{2.60}$$

has to be into account. To solve the integral we must consider two intervals. First for points close to the z-axis, $0 < \frac{r}{h} < 1$, the integral of Eq. 2.58 can be expressed as a sum of integrals with the intervals of integration and the interpolation functions $W_r(u_r)$ summarized in Tab. 2.1. An sketch of the different intervals can be seen in Fig. 2.4 where W_a and W_b represent the first and second parts of the cubic spline of Eq. 2.59, that is

$$W_a = 1 - \frac{3}{2}\frac{|r-r'|^2}{h^2} + \frac{3}{4}\frac{|r-r'|^3}{h^3} , \tag{2.61}$$

$$W_b = \frac{1}{4}\left(2-\frac{|r-r'|}{h}\right)^3 , \tag{2.62}$$

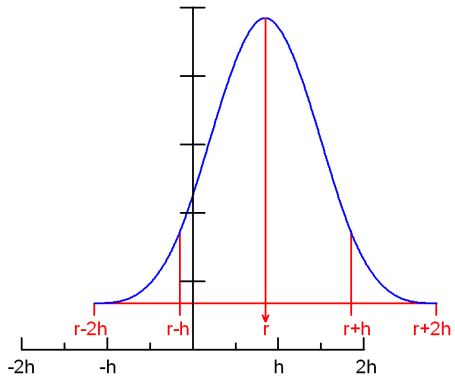

Figure 2.4: Strategy for integrating Eq 2.58 in the interval $0 < \frac{r}{h} < 1$. The blue line represents the kernel function (cubic spline). The integral in Eq 2.58 can be divided in the five intervals shown in Tab. 2.1.

INTEGRATION LIMITS	$\lvert r'\rvert$	$\lvert r - r'\rvert$	$W_r(u_r)$
$(-2h + r, 0)$	$-r'$	$r - r'$	W_b
$(0, -h + r)$	r'	$r - r'$	W_a
$(-h + r, r)$	r'	$r - r'$	W_a
$(r, r + h)$	r'	$r' - r$	W_a
$(r + h, r + 2h)$	r'	$r' - r$	W_b

Table 2.2: Integration intervals, and interpolation functions when $1 < \frac{r}{h} < 2$ needed to calculate f_1 using Eq. 2.58. W_a and W_b are defined in Eq. 2.61 and Eq. 2.62. See also Fig. 2.5.

The second case to be considered is when the normalized distance is in the range $1 < \frac{r}{h} < 2$. In this case, the new intervals of integration are summarized in Tab. 2.2 and the corresponding diagram can be seen in Fig. 2.5.

Finally, after some algebra the expression of $f_1(\zeta)$ given by Eq. 2.41 is obtained.

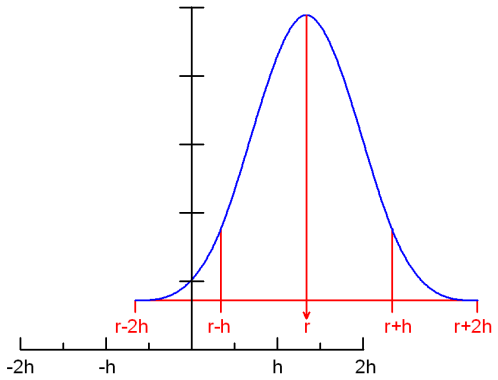

Figure 2.5: Strategy for integrating Eq. 2.58 in the interval $1 < \frac{r}{h} < 2$. The blue line represents the kernel function (cubic spline). The integral of Eq. 2.58 can be divided in the five intervals shown in Tab. 2.2.

2.5 The momentum equation modified by the corrected density

We express now the momentum equation modified by the corrected density (see Eq 2.40). The r-component of the momentum equation is

$$\ddot{r} = -\frac{1}{\rho}\frac{\partial P}{\partial r}\,, \tag{2.63}$$

which is calculated using the following identities

$$\frac{\partial(rP)}{\partial r} = P + r\frac{\partial P}{\partial r} \quad \Rightarrow \quad \frac{\partial P}{\partial r} = \frac{1}{r}\left(\frac{\partial(rP)}{\partial r} - P\right)\,, \tag{2.64}$$

$$\frac{\partial}{\partial r}\left(\frac{rP}{\eta}\right) = \frac{1}{\eta}\frac{\partial(rP)}{\partial r} - \frac{1}{\eta^2}rP\frac{\partial \eta}{\partial r} \quad \Rightarrow \quad \frac{1}{\eta}\frac{\partial(rP)}{\partial r} = \frac{\partial}{\partial r}\left(\frac{rP}{\eta}\right) + \frac{rP}{\eta^2}\frac{\partial \eta}{\partial r}\,, \tag{2.65}$$

and using the corrected 2D density $\widehat{\eta}$ we can express Eq. 2.63 as

$$\ddot{r} = \frac{2\pi}{\widehat{\eta}}\left[P - \frac{\partial(rP)}{\partial r}\right] = 2\pi\frac{P}{\widehat{\eta}} - \frac{2\pi rP}{\widehat{\eta}^2}\frac{\partial \widehat{\eta}}{\partial r} - \frac{\partial}{\partial r}\left(\frac{2\pi rP}{\widehat{\eta}}\right)\,. \tag{2.66}$$

When $r \rightarrow 0$ the particle approaches the z-axis where symmetry enforces the last term on the right side to vanish for spherically symmetric kernels. The first term on the right hand side is the hoop stress term which should be exactly balanced by the central term when $r \rightarrow 0$, because the r-component of the acceleration should be zero at the symmetry axis. Nevertheless, this does not happen unless the correction factor $f_1(\zeta)$ is taken into account during the calculation of the gradient of $\widehat{\eta}$

$$\frac{\partial \widehat{\eta}}{\partial r} = \frac{\partial(\eta \cdot f_1(\zeta))}{\partial r} = f_1(\zeta)\frac{d\eta}{dr} + \eta\frac{\partial f_1(\zeta)}{\partial r}\,, \tag{2.67}$$

and applying the standard SPH procedure to make derivatives

$$\frac{d\eta_i}{dr_i} = \sum_{j=1}^{N} m_j \frac{\partial W_{ij}}{\partial r_i}\,, \tag{2.68}$$

$$\frac{\partial}{\partial r_i}\left(\frac{2\pi r_i P_i}{\widehat{\eta}_i}\right) = \sum_{j=1}^{N} m_j \frac{2\pi r_j P_j}{\widehat{\eta}_j^2}\frac{\partial W_{ij}}{\partial r_i}\,, \tag{2.69}$$

finally the expression of the corrected momentum equation for the r-coordinate

$$\begin{aligned}\ddot{r}_i = 2\pi\frac{P_i}{\widehat{\eta}_i} - 2\pi\sum_{j=1}^{N}\left[m_j\left(\frac{P_i r_i}{\widehat{\eta}_i^2}\times f_1^i(\zeta_i) + \frac{P_j r_j}{\widehat{\eta}_j^2}\right)\frac{\partial W_{ij}}{\partial r_i}\right] \\ - \left(\frac{2\pi P_i\ r_i}{\widehat{\eta}_i \times f_1^i}\right)\ \frac{df_1^i(\zeta_i)}{dr_i}\,.\end{aligned} \tag{2.70}$$

Similarly, we can obtain the z-component, but this time considering that there is no hoop stress term and

$$\frac{\partial \widehat{\eta}}{\partial z} = f_1(\zeta)\frac{\partial \eta}{\partial z}\,, \tag{2.71}$$

thus, the expression for the z-component of momentum equation can be written as

$$\ddot{z}_i = -2\pi\sum_{j=1}^{N} m_j\left(\frac{P_i r_i}{\widehat{\eta}_i^{\,2}}\times f_1^i(\zeta_i) + \frac{P_j r_j}{\widehat{\eta}_j^{\,2}}\right)\frac{\partial W_{ij}}{\partial z_i}\,. \tag{2.72}$$

For particles far from the symmetry axis $f_1^i = 1$ and $\frac{df_1^i}{dr} = 0$ (see Fig. 2.6) and momentum equations (Eq. 2.70, and Eq. 2.72) became the same as those proposed by Brookshaw (Eq. 2.36, and Eq. 2.37). In order to evaluate the pressure at each time step the 3D-density has to be calculated

$$\widehat{\rho} = \frac{\widehat{\eta}}{2\pi r}\,. \tag{2.73}$$

Notice that close to the z-axis the components of momentum equation (Eq. 2.70, and Eq. 2.72) are non symmetric against the exchange of indexes i and j. Nevertheless, the r-component of the momentum is preserved owing to the reflexive boundary conditions. Hence, only the z-component is affected but it affects a very tiny amount of mass.

Using the Lagrangian formulation and assuming isentropic flow it is possible to derive the r-component of the momentum equation which takes into account the correction factors to density. The total kinetic and thermal energies in SPH are calculated directly from the N particles of the system,

$$\mathcal{L} = \sum_{j=1}^{N} m_j \left(\frac{1}{2} r_j^2 + \frac{1}{2} z_j^2 - E(\widehat{\rho}_j) \right)\,, \tag{2.74}$$

so the Lagrangian equation for the r-component can be written

$$m_i \ddot{r}_i + \sum_{j=1}^{N} m_j \frac{\partial E(\widehat{\rho}_j)}{\partial r_i} = 0\,, \tag{2.75}$$

and expanding the summation

$$m_i \ddot{r}_i + m_i \frac{P_i}{\widehat{\rho}_i^2} \frac{\partial \widehat{\rho}_i}{\partial r_i} + \sum_{j \neq i}^{N} m_j \frac{P_j}{\widehat{\rho}_j^2} \frac{\partial \widehat{\rho}_j}{\partial r_i} = 0\,, \tag{2.76}$$

now it is necessary to calculate the partial derivatives of the corrected density, taking into account the dependences on r expressed in Eq 2.73 and Eq. 2.40

$$\begin{aligned}\frac{\partial\widehat{\rho}_i}{\partial r_i} &= -\frac{1}{2\pi r_i^2}\widehat{\eta}_i + \frac{1}{2\pi r_i}\frac{\partial}{\partial r_i}(f_1^i \cdot \eta_i) \\ &= -\frac{1}{2\pi r_i^2}\widehat{\eta}_i + \frac{\eta_i}{2\pi r_i}\frac{\partial f_1^i}{\partial r_i} + \frac{1}{2\pi r_i} f_1^i \sum_{j=1}^{N} m_j \frac{\partial W_{ij}}{\partial r_i}\,,\end{aligned} \tag{2.77}$$

the corrected density of the particle j has a simple expression

$$\frac{\partial\widehat{\rho}_j}{\partial r_i} = \frac{1}{2\pi r_j}\frac{\partial}{\partial r_i}(f_1^j \cdot \eta_j) = \frac{1}{2\pi r_j} f_1^j m_i \frac{\partial W_{ji}}{\partial r_i}\,, \tag{2.78}$$

finally, replacing the expressions Eq. 2.77 and Eq. 2.78 in Eq. 2.76 and after some algebra, the final expression for the r-component of the equation of motion is written

$$\begin{aligned}\ddot{r}_i = 2\pi\frac{P_i}{\widehat{\eta}_i} - 2\pi\sum_{j=1}^{N}\left[m_j\left(\frac{P_i r_i}{\widehat{\eta}_i^2}\times f_1^i(\zeta_i) + \frac{P_j r_j}{\widehat{\eta}_j^2}\times f_1^j(\zeta_j)\right)\frac{\partial W_{ij}}{\partial r_i}\right] \\ - \left(\frac{2\pi P_i\ r_i}{\widehat{\eta}_i \times f_1^i}\right)\ \frac{df_1^i(\zeta_i)}{dr_i}\,.\end{aligned} \tag{2.79}$$

Following the same procedure for the z-component, the ensuing equation is

$$\ddot{z}_i = -2\pi\sum_{j=1}^{N} m_j\left(\frac{P_i r_i}{\widehat{\eta_i}^{\,2}}\times f_1^i(\zeta_i) + \frac{P_j r_j}{\widehat{\eta_j}^{\,2}}\times f_1^j(\zeta_j)\right)\frac{\partial W_{ij}}{\partial z_i}\,. \tag{2.80}$$

Despite the non-symmetric structure of Euler equations, conservation laws were fulfilled to a large extent, as shown in the test described in the next chapter.

2.6 The energy equation modified by the corrected density

We are now ready to deduce the modified energy equation including effects of axis correction factors. The energy equation can be expressed as

$$\frac{du}{dt} = -\frac{P}{\rho}\nabla\mathbf{v}\,, \tag{2.81}$$

if we transform it using the continuity equation

$$\frac{\partial\rho}{\partial t} = -\rho\nabla\mathbf{v}\,, \tag{2.82}$$

and write the result in terms of η

$$\begin{aligned}\nabla\mathbf{v} &= -\frac{1}{\rho}\frac{\partial\rho}{\partial t} = -\frac{2\pi r}{\eta}\frac{\partial}{\partial t}\left(\frac{\eta}{2\pi r}\right) = \\ &= -\frac{r}{\eta}\left(\eta\frac{\partial}{\partial t}\left(\frac{1}{r}\right) + \frac{1}{r}\frac{\partial\eta}{\partial t}\right) = \\ &= \frac{v_r}{r} - \frac{1}{\eta}\frac{\partial\eta}{\partial t}\,,\end{aligned} \tag{2.83}$$

putting the last expression of these identities in Eq. 2.81, and using the corrected 2D density $\widehat{\eta}$, we can write the energy conservation as

$$\frac{du}{dt} = -2\pi\frac{P}{\widehat{\eta}}\,v_r + 2\pi\frac{Pr}{\widehat{\eta}^2}\frac{d\widehat{\eta}}{dt}\,. \tag{2.84}$$

At this point it is necessary to know the temporal evolution of the corrected 2D density $\widehat{\eta}$. Using Eq. 2.83 and Eq. 1.6 we get

$$\frac{d\widehat{\eta}}{dt} = \widehat{\eta}\left(\frac{v_r}{r} - \nabla\mathbf{v}\right) = -\widehat{\eta}\left(\frac{\partial v_r}{\partial r} + \frac{\partial v_z}{\partial z}\right)\,, \tag{2.85}$$

and using

$$\frac{\partial(\widehat{\eta v_r})}{\partial r} = \widehat{\eta}\frac{\partial v_r}{\partial r} + v_r\frac{\partial\widehat{\eta}}{\partial r}\,, \tag{2.86}$$

we can rewrite Eq. 2.85 as

$$\frac{d\widehat{\eta}}{dt} = \left[v_r \frac{\partial \widehat{\eta}}{\partial r} - \frac{\partial(\widehat{\eta v_r})}{\partial r} \right] + \left[v_z \frac{\partial \widehat{\eta}}{\partial z} - \frac{\partial(\widehat{\eta v_z})}{\partial z} \right] , \tag{2.87}$$

to complete the deduction of the energy equation it is necessary to calculate the magnitudes labeled with a widehat. The corrected density, $\widehat{\eta}$ can be expressed as $\widehat{\eta} = \eta \times f_1$ (see Eq. 2.40) where the expression f_1 (Eq. 2.41) has been calculated in Sec. 2.4. To evaluate the expressions $\widehat{\eta v_r}$ and $\widehat{\eta v_z}$ we proceed in a similar way as in the deduction of the function f_1.

Expanding the components of the velocity of a particle near the z-axis as linear functions

$$v_z(r', z') = v_z(0, z) + \left(\frac{\partial v_z}{\partial r'} \right)_{r'=0} (r' - 0) + \left(\frac{\partial v_z}{\partial z'} \right)_{z'=z} (z' - z) , \tag{2.88}$$

if v_z is a weakly depending function of the r-coordinate we can write

$$v_z(r', z') = v_z(0, z) + \left(\frac{\partial v_z}{\partial z'} \right)_{z'=z} (z' - z) \simeq v_z(z') , \tag{2.89}$$

redoing the same calculations we can exchange η by ηv_z and derive a similar equation as Eq. 2.56

$$< \eta v_z >= \frac{\widehat{\eta v_z}}{f_1(\zeta)} . \tag{2.90}$$

The r-component of the velocity needs a new correction function that we call f_2. Returning to the Taylor series we write

$$v_r(r', z') = v_r(0, z) + \left(\frac{\partial v_r}{\partial r'} \right)_{r'=0} (r' - 0) + \left(\frac{\partial v_r}{\partial z'} \right)_{z'=z} (z' - z) , \tag{2.91}$$

symmetry enforces the radial velocity to be zero at the z-axis close to the axis the radial velocity can be expressed as $v_r = Cr$ where

$$C = \left(\frac{\partial v_r}{\partial r'}\right)_{r'=0} , \tag{2.92}$$

using this approximation and proceeding as in the deduction of Eq. 2.55 we easily arrive to the following expression

$$< \eta v_r >= \eta(z) v_z \cdot \left(\frac{K^{1D}}{r^2} \int_{-\infty}^{\infty} r' |r'| W_r(u_r) dr' \right) , \tag{2.93}$$

thus we can express

$$< \eta v_r >= \frac{\widehat{\eta v_r}}{f_2(\zeta)} , \tag{2.94}$$

where $\zeta = r/h$ and defining f_2 as

$$\frac{1}{f_2(\zeta)} = \frac{K^{1D}}{r^2} \int_{-\infty}^{\infty} r' |r'| W_r(u_r) dr' . \tag{2.95}$$

As in the case of magnitude f_1, this integral can be evaluated analytically for the cubic-spline kernel, leading to

$$f_2^i(\zeta) = \begin{cases} \left[\frac{14}{15}\zeta_i^{-1} + \frac{4}{9}\zeta_i - \frac{1}{15}\zeta_i^3 + \frac{1}{60}\zeta_i^4\right]^{-1} & \text{if } 0 < \zeta_i < 1 \\ \left[-\frac{1}{45}\zeta_i^{-2} + \frac{16}{15}\zeta_i^{-1} - \frac{1}{3} + \frac{8}{9}\zeta_i - \frac{1}{3}\zeta_i^2 + \frac{1}{15}\zeta_i^3 - \frac{1}{180}\zeta_i^4\right]^{-1} & \text{if } 1 < \zeta_i < 2 \\ 1 & \text{if } \zeta_i > 2 \end{cases} . \tag{2.96}$$

Going back to Eq. 2.87 and using $\widehat{(\eta v_z)} = (\eta v_z) \times f_1$ (Eq. 2.90), $\widehat{(\eta v_r)} = (\eta v_r) \times f_2$ (Eq. 2.94) and noticing that f_1 and f_2 are independent of the z coordinate

$$\begin{aligned} \frac{d\widehat{\eta}}{dt} = & \left[v_r f_1 \frac{\partial \eta}{\partial r} + v_r \eta \frac{\partial f_1}{\partial r} - f_2 \frac{\partial (\eta v_r)}{\partial r} - (\eta v_r) \frac{\partial f_2}{\partial r} \right] + \\ & + \left[f_1 v_z \frac{\partial \eta}{\partial z} - f_1 \frac{\partial (\eta v_z)}{\partial z} \right] , \end{aligned} \tag{2.97}$$

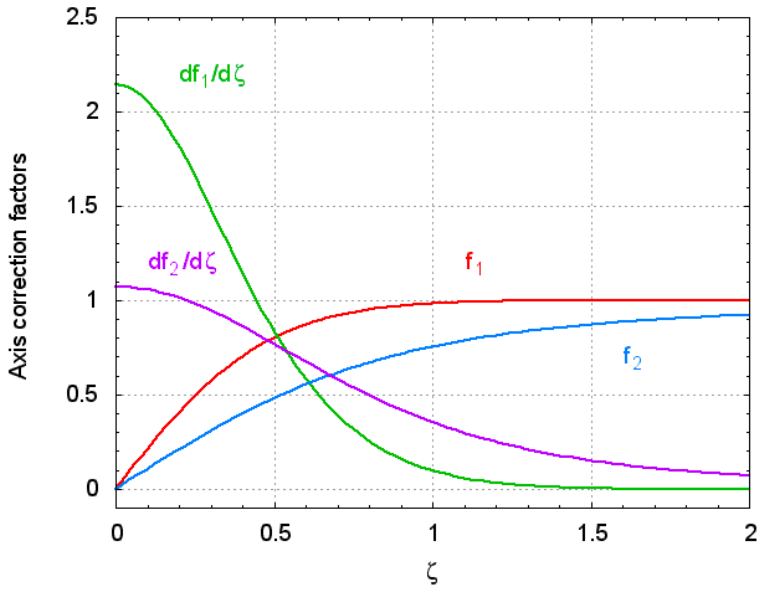

Figure 2.6: Correction factors f_1 and f_2 and their derivatives as function of $\zeta = r/h$.

and, writing the different terms on the right side as a finite summations

$$\eta_i = \sum_{j=1}^{N} m_j W_{ij} \,, \tag{2.98}$$

$$(\eta_i v_{ri}) = \sum_{j=1}^{N} m_j v_{rj} W_{ij} \,, \tag{2.99}$$

$$\frac{\partial \eta_i}{\partial r_i} = \sum_{j=1}^{N} m_j \frac{\partial W_{ij}}{\partial r_i} \,, \tag{2.100}$$

$$\frac{\partial (\eta_i v_{r_i})}{\partial r_i} = \sum_{j=1}^{N} m_j v_{rj} \frac{\partial W_{ij}}{\partial r_i} \,, \tag{2.101}$$

therefore the continuity equation finally writes

$$\begin{aligned} \frac{\partial \widehat{\eta_i}}{\partial t} = & \sum_{j=1}^{N} m_j \left(f_1^i v_{r_i} - f_2^i v_{r_j} \right) \frac{\partial W_{ij}}{\partial r_i} + \sum_{j=1}^{N} m_j \left(\frac{\partial f_1^i}{\partial r_i} v_{r_i} - \frac{\partial f_2^i}{\partial r_i} v_{r_j} \right) W_{ij} \\ & + f_1^i \sum_{j=1}^{N} m_j \left(v_{z_i} - v_{z_j} \right) \frac{\partial W_{ij}}{\partial z_i} \,. \end{aligned} \tag{2.102}$$

Note that f_1^i, f_2^i and their derivatives are only function of the current radial coordinate of the particle and its smoothing length. Thus, they can easily be computed and stored in a vector without introducing any significant computational overload. Eq. 2.102 is used to evaluate the energy equation, using Eq. 2.84 for each particle i

$$\frac{du_i}{dt} = -2\pi \frac{P_i}{\widehat{\eta}_i}\ v_{r_i} + 2\pi \frac{P_i r_i}{\widehat{\eta}_i{}^2} \frac{d\widehat{\eta}_i}{dt}\,. \tag{2.103}$$

2.7 An approach to the conduction term

Including a heat conduction term in the energy equation is necessary to solve two kind of problems. Firstly, to account for real physical heat fluxes arising from sources or sinks of energy (for example the energy released by nuclear reactions, absorption or emission in processes of excitation or deexcitation, etc). We can find interesting examples in astrophysics as for example in cosmological simulations of cluster formation (see for example [31], [74]). In the Inertial Confinement Fusion and Laboratory Astrophysics context it is necessary to include at least the electron heat flux which is the most dominant energy transport term before the nuclear reactions take over ([6],[18]).

An additional benefit of including a conduction term in the energy equation has to do with the artificial smoothing of the excess of heat introduced by the artificial viscosity known as "wall heating" (see ([52]). For example when two streams of gas collide it is usual to find an artificial spike in the internal energy which can be smoothed including a conductivity coefficient adequately scaled to spread the excess of heat (see the wall heating shock and the collision of two jets tests in Sec. 3.3 and Sec. 4.2).

In both cases the equation which has to be solved is

$$\left(\frac{du}{dt}\right)_{cond} = \frac{1}{\rho}\nabla \cdot (\kappa \nabla T)\,, \tag{2.104}$$

where κ is the conductivity coefficient which is a function of the thermodynamical variables and chemical composition of the material or a function of the local sound velocity and of the local velocity gradient in the context of wall heating.

As we can see Eq. 2.104 requires the calculation of a second derivative to compute the heat flux. Although in SPH it is possible to calculate second derivatives by simply differentiating the kernel twice, as for example (in one dimension)

$$\left(\frac{d^2T}{dx^2}\right)_i = \sum_{j=1}^{N} \frac{m_j T_j}{\rho_j} \frac{d^2 W_{ij}}{dx_i^2} \,, \tag{2.105}$$

it is not a good choice because usually it is too sensible to the numerical noise present in disordered systems. Also the above procedure can lead to unphysical results (i.e. heat flux from low to high temperature regions) because the sign of the second derivative can change depending on the distance of the particles. An alternative expression has been proposed, for example by Brookshaw or Monaghan ([8],[45]), using an integral expression that relies in the first derivative of the interpolation kernel (see for example [31]). In cartesian coordinates it leads to

$$\left(\nabla^2 Y\right)_i = 2 \sum_{j=1}^{N} \frac{m_j}{\rho_j} \frac{Y_j - Y_i}{r_{ij}^2} \mathbf{r}_{ij} \cdot \nabla_{\mathbf{i}} W_{ij} \,, \tag{2.106}$$

where $\mathbf{r}_{ij} = \mathbf{r}_i - \mathbf{r}_j$. To adapt this expression to 2D cylindrical coordinates we can use the following expression

$$\nabla^2 Y = \nabla \cdot (\nabla Y) = \frac{\left(\frac{\partial Y}{\partial r}\right)}{r} + \frac{\partial}{\partial r}\left(\frac{\partial Y}{\partial r}\right) + \frac{\partial}{\partial z}\left(\frac{\partial Y}{\partial z}\right) \,. \tag{2.107}$$

Since the Laplacian of a scalar magnitude is the same as the divergence of the gradient of the magnitude it is clear that a term depending on $1/r$ must appear. As we will see in the next section, this first term on the right is important to reproduce the detailed evolution of a thermal wave. This new term has not been considered in past 2D axisymmetric approximations (see for example the artificial thermal conduction proposed by Brookshaw in [8]).

Now, for simplicity, we can rewrite the above expression as

$$\nabla^2 Y = \nabla \cdot (\nabla Y) = \frac{\left(\frac{\partial Y}{\partial r}\right)}{r} + \mathbf{D}^2 Y \,, \tag{2.108}$$

where the operator $\mathbf{D}$ has the same expression as the Cartesian one

$$\mathbf{D} = \left(\frac{\partial}{\partial r}, \frac{\partial}{\partial z} \right) . \tag{2.109}$$

Now let us introduce an useful relationship

$$\nabla \cdot (\kappa \nabla T) = \frac{1}{2} \left[\nabla^2(\kappa T) - T\nabla^2 \kappa + \kappa \nabla^2 T \right] , \tag{2.110}$$

where the three terms on the right hand can be expressed using Eq. 2.108 and Eq. 2.106 as

$$\nabla^2(\kappa_i T_i) = \frac{1}{r_i} \frac{\partial(\kappa_i T_i)}{\partial r_i} + 2 \sum_{j=1}^{N} \frac{m_j}{\widehat{\eta}_j} \frac{\kappa_j T_j - \kappa_i T_i}{s_{ij}^2} \mathbf{s}_{ij} \cdot \mathbf{D}_i W_{ij} , \tag{2.111}$$

$$T_i \nabla^2(\kappa_i) = \frac{T_i}{r_i} \frac{\partial(\kappa_i)}{\partial r_i} + 2 \sum_{j=1}^{N} \frac{m_j}{\widehat{\eta}_j} \frac{\kappa_j T_i - \kappa_i T_i}{s_{ij}^2} \mathbf{s}_{ij} \cdot \mathbf{D}_i W_{ij} , \tag{2.112}$$

$$\kappa_i \nabla^2(T_i) = \frac{\kappa_i}{r_i} \frac{\partial(T_i)}{\partial r_i} + 2 \sum_{j=1}^{N} \frac{m_j}{\widehat{\eta}_j} \frac{\kappa_i T_j - \kappa_i T_i}{s_{ij}^2} \mathbf{s}_{ij} \cdot \mathbf{D}_i W_{ij} , \tag{2.113}$$

where $\mathbf{s} = (r, z)$ is the position vector in cylindrical coordinates. Using the following equality

$$\kappa_i T_i - \kappa_i T_j + \kappa_j T_i - \kappa_j T_j = (\kappa_i + \kappa_j)(T_i - T_j) , \tag{2.114}$$

and adding the three contributions above, we can express the Eq. 2.104 as

$$\begin{aligned} \left(\frac{du_i}{dt} \right)_{cond} = & \frac{1}{2\rho_i} \left\{ \frac{1}{r_i} \frac{\partial(\kappa_i T_i)}{\partial r_i} - \frac{T_i}{r_i} \frac{\partial \kappa_i}{\partial r_i} + \frac{\kappa_i}{r_i} \frac{\partial T_i}{\partial r_i} \right\} - \\ & \frac{1}{\rho_i} \sum_{j=1}^{N} \left(m_j \frac{\kappa_i + \kappa_j}{\widehat{\eta}_j} (T_i - T_j) \frac{\mathbf{s}_{ij}}{s_{ij}^2} \cdot \mathbf{D}_i W_{ij} \right) . \end{aligned} \tag{2.115}$$

The part inside the brackets are the new terms related to the hoop stress. According to Monaghan [45] we can express the derivative of a function, A, as

$$\frac{\partial A_i}{\partial r_i} = \sum_j \frac{m_j}{\widehat{\eta}_j}(A_j - A_i)\frac{\partial W_{ij}}{\partial r_i}\,, \tag{2.116}$$

which guarantees that a constant function has zero derivative. After a little algebra we can express the final form of the conduction term as

$$\begin{aligned}\left(\frac{du_i}{dt}\right)_{cond} &= -\pi \sum_{j=1}^{N} m_j \frac{(\kappa_i + \kappa_j)}{\widehat{\eta}_i \widehat{\eta}_j}(T_i - T_j)\frac{\partial W_{ij}}{\partial r_i} \\ &+ 2\pi r_i \sum_{j=1}^{N} m_j \frac{\kappa_i + \kappa_j}{\widehat{\eta}_i \widehat{\eta}_j}(T_i - T_j)\frac{\mathbf{s}_{ij}}{s_{ij}^2} \cdot \mathbf{D}_i W_{ij}\,,\end{aligned} \tag{2.117}$$

where the first term on the right is the one related to the hoop-stress. The factor $(T_i - T_j)$ of both terms of Eq. 2.117 ensures that there is not heat flux between different parts of an isothermal system. Although the presence of the r_i multiplier in the second term of the right side of Eq. 2.117 does not ensure complete conservation of the heat flux, the total energy losses in the numerical test simulating a thermal wave evolution (see Sec. 3.2) were negligible. Of course Eq. 2.117 can be symmetrized by taking the arithmetical mean $\bar{r}_{ij} = 0.5(r_i + r_j)$ instead of r_i but in that case we found that the evolution of the thermal wave was not so well reproduced.

2.8 Entropy equation in *AxisSPH*

We are ready to deduce the variation with time of the total entropy S of a system in axisymmetric coordinates. For a group of N particles we can evaluate the total variation of entropy as (see [45])

$$\frac{dS}{dt} = \sum_{j=1}^{N} m_j \frac{ds_j}{dt} = \sum_{j=1}^{N} \frac{m_j}{T_j}\frac{dq_j}{dt}\,, \tag{2.118}$$

where s_j represents the entropy/mass, q_j represents the heat content/mass of particle j and T_j is the temperature.

For the sake of simplicity it is better to express the change of entropy in two parts (as in Eq. 2.117) one related to the hoop stress involving $\partial/\partial r$, which is important for particles near the z-axis, and another related to the Cartesian operator $\mathbf{D}$ (see Eq. 2.109)

$$\frac{dS}{dt} = \left(\frac{dS}{dt}\right)_{axis} + \left(\frac{dS}{dt}\right)_{cartesian} . \tag{2.119}$$

Now considering the first term of Eq. 2.117 we can write

$$\left(\frac{dS}{dt}\right)_{axis} = -\pi \sum_{i=1}^{N}\sum_{j=1}^{N} \frac{1}{T_i}\frac{m_i m_j}{\widehat{\eta}_i\widehat{\eta}_j}(\kappa_i + \kappa_j)(T_i - T_j)\frac{\partial W_{ij}}{\partial r_i} , \tag{2.120}$$

if we interchange the indexes in the above expression, and using the antisymmetry properties of $\partial W_{ij}/\partial r_i$ we get a similar expression as Eq. 2.120 for the entropy change. Then, averaging both expressions we obtain

$$\left(\frac{dS}{dt}\right)_{axis} = -\frac{\pi}{2} \sum_{i=1}^{N}\sum_{j=1}^{N} \frac{m_i m_j}{\widehat{\eta}_i\widehat{\eta}_j}(\kappa_i + \kappa_j)(T_i - T_j)\left(\frac{1}{T_i} + \frac{1}{T_j}\right)\frac{\partial W_{ij}}{\partial r_i} . \tag{2.121}$$

We can do the same deduction for $\left(\frac{dS}{dt}\right)_{cartesian}$ just changing

$$\frac{\partial W_{ij}}{\partial r_i} \rightarrow -2r_i\left(\frac{\mathbf{s}_{ij}\cdot\mathbf{D}_i W_{ij}}{s_{ij}^2}\right) , \tag{2.122}$$

in Eq. 2.120 and noticing that the factor in brackets on the right term of the above expression is symmetric we can write

$$\left(\frac{dS}{dt}\right)_{cartesian} = \pi \sum_{i=1}^{N}\sum_{j=1}^{N} \frac{m_i m_j}{\widehat{\eta}_i\widehat{\eta}_j}(\kappa_i + \kappa_j)(T_i - T_j)\left(\frac{r_i}{T_i} - \frac{r_j}{T_j}\right)\frac{\mathbf{s}_{ij}\cdot\mathbf{D}_i W_{ij}}{s_{ij}^2} . \tag{2.123}$$

Putting Eqs. 2.121 and 2.123 into Eq. 2.119 the final expression for the variation of the total entropy of a system of N particles is written

$$\frac{dS}{dt} = -\frac{\pi}{2}\sum_{i=1}^{N}\sum_{j=1}^{N}\frac{m_i m_j}{\widehat{\eta}_i\widehat{\eta}_j}(\kappa_i+\kappa_j)(T_i-T_j)\left(\frac{1}{T_i}+\frac{1}{T_j}\right)\frac{\partial W_{ij}}{\partial r_i}+ \\ \pi\sum_{i=1}^{N}\sum_{j=1}^{N}\frac{m_i m_j}{\widehat{\eta}_i\widehat{\eta}_j}(\kappa_i+\kappa_j)(T_i-T_j)\left(\frac{r_i}{T_i}-\frac{r_j}{T_j}\right)\frac{\mathbf{s}_{ij}\cdot\mathbf{D}_i W_{ij}}{s_{ij}^2}\,. \tag{2.124}$$

As in the entropy equation devised by Monaghan [45] using cartesian coordinates, the Eq. 2.124 also predicts entropy increasing but the existence of the negative term on the right makes the demonstration less trivial. However, a sufficient condition for entropy increasing is that

$$\frac{r_i}{r_i-r_j} > \frac{1}{2}\,, \tag{2.125}$$

which is fulfilled in a large domain of the system. The exception could be the axis vicinity where $r_i \to 0$. Nevertheless close to the z-axis symmetry enforces the heat flux to be negligible and entropy would remain unchanged. Therefore, in general, entropy is expected to increase although it is not excluded a marginal decrease if resolution is poor and strong heat fluxes were present close to $r = 0$. We have monitored the evolution of total entropy in the numerical test simulating a thermal wave evolution (see Sec. 3.2) and found no indications of entropy decreasing during the simulation.

2.9 Artificial viscosity

A feature shared by all SPH hydrocodes is that they incorporate the artificial viscosity (AV) formalism to handle with shocks. Because SPH has some similarity with Monte Carlo methods the inclusion of the AV also helps to control the level numerical noise inherent to these statistical methods. Artificial viscosity is an old topic of fluid mechanics. It was devised around 1940 by John von Neumann at Los Alamos National Laboratory to simulate the propagation of strong shocks which

appear during atomic explosions. It is basically a simple algorithm which converts kinetic energy into heat in regions with size close to the resolution achieved by the hydrocode. Although still in use, it has been progressively replaced by other more efficient (and sophisticated) schemes based on Riemann-solvers, especially in multidimensional calculations using Eulerian codes. Nevertheless because of the similarities of SPH and molecular dynamics AV is still currently being used in most of SPH applications where such sort of viscosity acts mimicking the real viscosity among atoms and molecules. Although there exists a formulation of artificial viscosity developed in a Riemann-solver style [44] we have adapted the most standard formulation of AV, as given for instance in Rosswog 2009 [68] to the peculiarities of *AxisSPH*

First, a phenomenological viscosity term Q is added to the true pressure, P, in the momentum equation. That "viscous" pressure is a function of the divergence of velocity so that it becomes high during compressions. To better handle with strong shocks and smooth the post-shock oscillations of the fluid it is usual to define also a quadratic viscous pressure Q_q proportional to the square of velocity divergence. The artificial viscous pressure is then

$$Q = Q_{bulk} + Q_q \,, \tag{2.126}$$

where

$$Q_{bulk} = -\alpha \rho l c_s \nabla \mathbf{v} \,, \tag{2.127}$$

$$Q_q = \beta \rho l^2 \left(\nabla \mathbf{v}\right)^2 \,, \tag{2.128}$$

where α, β are free adjustable parameters of order unity, c_s is the sound speed and l is the typical length scale over the shock is spread, $l \simeq h$. To incorporate Q into the standard SPH equations of momentum and energy a term Π_{ij}^{3D} is usually defined (see for instance Hernquist & Katz [29])

$$\Pi_{ij}^{3D} = \begin{cases} \frac{Q_i}{\rho_i^2} + \frac{Q_j}{\rho_j^2} & \text{if } \mathbf{v}_{ij} \cdot \mathbf{r}_{ij} < 0 \\ 0 & \text{if } \mathbf{v}_{ij} \cdot \mathbf{r}_{ij} \geq 0 \end{cases} , \tag{2.129}$$

where

$$Q_i = \begin{cases} \alpha\rho_i c_i h_i |\nabla \mathbf{v}|_i + \beta\rho_i h_i^2 |\nabla \mathbf{v}|_i^2 & \text{if } \mathbf{v}_{ij}\cdot\mathbf{r}_{ij} < 0 \\ 0 & \text{if } \mathbf{v}_{ij}\cdot\mathbf{r}_{ij} \geq 0 \end{cases}, \tag{2.130}$$

where the value of $|\nabla \mathbf{v}|_i$ is borrowed from the continuity equation, expression Eq. 2.131 to obtain

$$|\nabla \mathbf{v}|_i = -\frac{1}{\rho_i}\sum_j^N m_j \mathbf{v}_{ij}\cdot\nabla_i W_{ij}\,. \tag{2.131}$$

This form represents a combination of bulk and quadratic viscosity. Note that for divergent flows $Q_i = 0$. Although this formulation of viscosity has proven useful it still leads to numerical oscillations in the post shock region during strong shocks. The most used version of the artificial viscosity substitutes the calculation of Eq. 2.131 by an estimation of the velocity divergence closest to that of molecular dynamics

$$\mu_{ij} = \frac{\bar{h}_{ij}\mathbf{v}_{ij}\cdot\mathbf{r}_{ij}}{r_{ij}^2 + \nu^2}\,, \tag{2.132}$$

and the magnitude Π_{ij}^{3D} is then expressed as,

$$\Pi_{ij}^{3D} = \begin{cases} \frac{\alpha\bar{c_{ij}}\mu_{ij} + \beta\mu_{ij}^2}{\bar{\rho}_{ij}} & \text{if } \mathbf{v}_{ij}\cdot\mathbf{r}_{ij} < 0 \\ 0 & \text{if } \mathbf{v}_{ij}\cdot\mathbf{r}_{ij} \geq 0 \end{cases}, \tag{2.133}$$

where $\bar{h}_{ij} = \frac{1}{2}(h_i + h_j)$, $\bar{\rho}_{ij} = \frac{1}{2}(\rho_i + \rho_j)$ and $\bar{c}_{ij} = \frac{1}{2}(c_i + c_j)$ are the averaged smoothing length, density and speed of sound between particle i and its neighbor j respectively. The above expression Eq. 2.133 can be used in any SPH code with independence of the dimensionality of the problem provided it is written in cartesian coordinates. The $\nu = 0.1\bar{h}_{ij}$ helps to avoid divergences when $\mathbf{r}_{ij} \to 0$ and the parameters α and β are of order unity. With this expression of the artificial viscosity the viscous acceleration is

$$\mathbf{a}_i^{vis}(3D) = \sum_{j=1}^{N} m_j \Pi_{ij}^{3D} \nabla_i W_{ij} \,, \tag{2.134}$$

and the momentum and energy conservation are rewritten as in Eq 2.23 and Eq 2.24. This viscosity has some advantages: it is Galilean invariant, conserves total linear and angular momenta and it vanishes for rigid body rotation. Nevertheless it can generate spurious viscosity, specially in pure shear flows or in regions with large vorticity. Balsara [5] proposed a modification to Eq. 2.132 in the form

$$\mu_{ij} = \begin{cases} \frac{h_{ij}\mathbf{v}_{ij}\cdot\mathbf{r}_{ij}}{r_{ij}^2+\nu^2}\frac{f_i+f_j}{2} & \text{if } \mathbf{v}_{ij}\cdot\mathbf{r}_{ij} < 0 \\ 0 & \text{if } \mathbf{v}_{ij}\cdot\mathbf{r}_{ij} \geq 0 \end{cases} , \tag{2.135}$$

where f_i is defined by

$$f_i = \frac{|\nabla \mathbf{v}|_i}{|\nabla \mathbf{v}|_i + |\nabla \times \mathbf{v}|_i} \,, \tag{2.136}$$

where $|\nabla \mathbf{v}|_i$ is given by Eq. 2.131, and

$$|\nabla \times \mathbf{v}|_i = \frac{1}{\rho_i} \sum_{j}^{N} m_j \mathbf{v}_{ij} \times \nabla_i W_{ij} \,, \tag{2.137}$$

The Balsara viscosity has the advantage that dissipation in shear layers is suppressed, because f_i acts as a switch. If compression dominates in the flow ($|\nabla \mathbf{v}|_i \gg |\nabla \times \mathbf{v}|_i$), $f_i \to 1$ and the expression Eq. 2.132 is recovered.

On the other hand, $f_i \to 0$ when the compression in the fluid is low and the vorticity is high ($|\nabla \mathbf{v}|_i \ll |\nabla \times \mathbf{v}|_i$) and the viscosity is suppressed.

Because Π_{ij}^{3D} given by Eq. 2.133 implicitly contains the divergence of the velocity we can adapt it to the axisymmetric geometry just by adding an extra term accounting for the geometrical convergence of the flux towards the symmetry axis,

$$\Pi_{ij}^{2D} = \Pi_{ij}^{(1)} + \Pi_{ij}^{(2)} \,. \tag{2.138}$$

The term $\Pi_{ij}^{(1)}$ is accounting for the cartesian part of viscosity whereas $\Pi_{ij}^{(2)}$ describes the convergence of the flux towards the symmetry axis in cylindrical coordinates. This new term, $\Pi_{ij}^{(2)}$ has to be proportional to v_r/r (the non cartesian part of velocity divergence in cylindrical coordinates) and it has not been included in the existing formalisms of axisymmetric SPH insofar. Due to its inverse dependence on r its inclusion may be crucial to handle implosions or any application involving axis converging fluxes.

The easiest way to write the Cartesian contribution of the artificial viscosity $\Pi_{ij}^{(1)}$ to the momentum and energy equations in an axisymmetric code is by changing the mass of the particles according to their distance to the z-axis, $m \to m/2\pi r$. The viscous acceleration becomes

$$\mathbf{a}_i^{vis}(2D) = \sum_{j=1}^{N} \frac{m_j}{2\pi \bar{r}_{ij}} \Pi_{ij}^{3D} \mathbf{D}_i W_{ij} \,, \tag{2.139}$$

where $\bar{r}_{ij} = (r_i + r_j)/2$. In particular taking $\bar{\rho}_{ij} = \bar{\eta}_{ij}/(2\pi \bar{r}_{ij})$ in equation Eq. 2.133 removes the explicit dependence on r_{ij} in the viscous acceleration formula, which now reads

$$\mathbf{a}_i^{vis}(1) = \sum_{j=1}^{N} m_j \Pi_{ij}^{(1)} \mathbf{D}_i W_{ij} \,, \tag{2.140}$$

where $\Pi_{ij}^{(1)}$ is

$$\Pi_{ij}^{(1)} = \begin{cases} \frac{-\alpha_0 \bar{c_{ij}} \mu_{ij} + \beta_0 \mu_{ij}^2}{\bar{\bar{\eta}}_{ij}} & \text{if } \mathbf{v}_{ij} \cdot \mathbf{s}_{ij} < 0 \\ 0 & \text{if } \mathbf{v}_{ij} \cdot \mathbf{s}_{ij} \geq 0 \end{cases} , \tag{2.141}$$

where μ_{ij} is now written

$$\mu_{ij} = \frac{\bar{h}_{ij} \mathbf{v}_{ij} \cdot \mathbf{s}_{ij}}{s_{ij}^2 + \nu^2} \,. \tag{2.142}$$

An explanation about the origin of $\Pi_{ij}^{(2)}$ and its dependence on hv_r/r can be drawn on simple geometrical basis. Any particle with mass m in axisymmetric

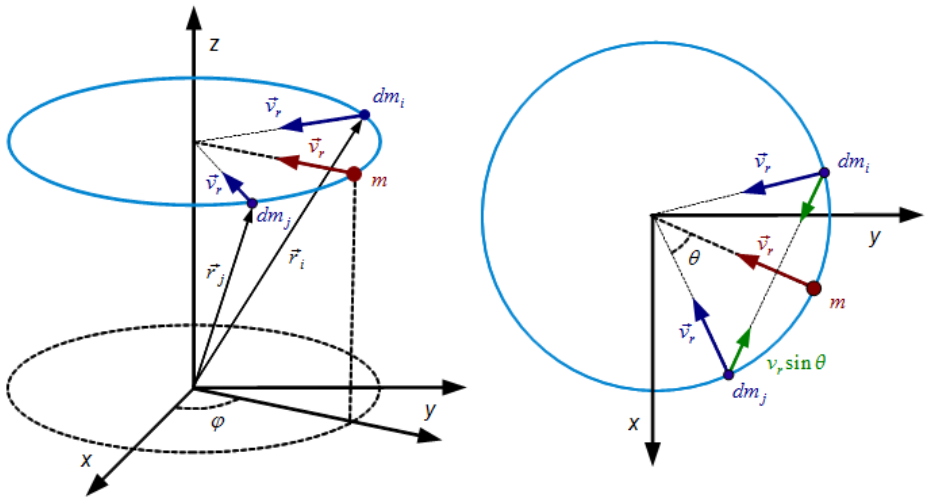

Figure 2.7: Schematic representation of a 2D Axisymmetric SPH particle of mass m (red particle) approaching to the z axis with radial component velocity $\mathbf{v}_r$. The blue hoop represents the real nature of this particle seen in 3D dimensions, that could be "divided" in a set of 3D particles, two symmetric ones are represented in blue color dm_i and dmj. On the left is represented the projection of the right sketch in plane XY. The green vector represents the projection of $\mathbf{v}_r$ on $\mathbf{r}_{ij} = \mathbf{r}_i - \mathbf{r}_j$.

geometry represents a hoop in 3D which can be imagined as a string of k particles carrying a mass m/k. When a 2D particle (the red colored particle m in Fig. 2.7) moves toward the z-axis with radial velocity v_r, the hoop reduces its radius which is equivalent to a convergent flow of 3D particles. The contribution of a symmetric pair of these 3D particles belonging to the hoop (labeled as dm_i and dm_j in Fig. 2.7) to the artificial viscosity can be calculated using Eq. 2.132

$$\mu_{ij} = \frac{\bar{h}_{ij}\mathbf{v}_{ij}\cdot\mathbf{r}_{ij}}{r_{ij}^2} = \frac{\bar{h}_{ij}2v_r sin\theta}{r_{ij}}\,, \tag{2.143}$$

where $\mathbf{r}_{ij} = \mathbf{r}_i - \mathbf{r}_j$ are 3D vectors. Writing the above expression in terms of the cylindrical coordinate r leads to

$$\mu_{ij} = \frac{\bar{h}_{ij}v_r}{r}\,. \tag{2.144}$$

Therefore the interpretation above supports the inclusion of a term proportional to $\bar{h}_{ij}v_r/r$ in $\Pi_{ij}^{(2)}$. Therefore we propose the following expression for the

axis-converging part of the artificial viscosity

$$\Pi_{ij}^{(2)} = \begin{cases} \frac{-\alpha_1 \bar{c_{ij}} q_{ij} + \beta_1 q_{ij}^2}{\bar{\bar{\eta}}_{ij}} & \text{if } v_{r_i} < 0 \quad \wedge \quad v_{r_j} < 0 \\ 0 & \text{other cases} \end{cases} , \tag{2.145}$$

where

$$q_{ij} = \frac{1}{2}\left(\frac{h_i v_{r_i}}{r_i} + \frac{h_j v_{r_j}}{r_j}\right) , \tag{2.146}$$

This form of $\Pi_{ij}^{(2)}$ has several interesting properties:

(1) For homologous contractions the viscous acceleration associated to this term is negligible because $v_r \propto r$, thus $q_{ij} \simeq const$ and the gradient vanishes.

(2) It conserves momentum because it is symmetric with respect particles i and j.

(3) Far enough from the axis it becomes much lower than the cartesian part of the artificial viscosity $\Pi_{ij}^{(1)}$.

(4) It vanish for those particles with $v_r > 0$ (i.e. divergent fluxes), and only the cartesian part of the viscosity matters. Therefore constants α_0 and β_0 of $\Pi_{ij}^{(1)}$ should remain close to their standard values $\alpha_0 \simeq 1$ and $\beta_0 \simeq 1$. For the axis converging part the simplest option is to take $\alpha = \alpha_0$ and $\beta = \beta_0$ (all simulations presented in this thesis were carried out using $\alpha_1 = \alpha_0 = 1$ and $\beta_1 = \beta_0 = 2$).

The resulting viscous acceleration writes

$$\mathbf{a}_i^{vis}(2D) = \sum_{j=1}^{N} m_j \Pi_{ij}^{2D} \mathbf{D}_i W_{ij} , \tag{2.147}$$

Each component of Eq. 2.147 has to be added to the momentum equations Eq. 2.79 and Eq. 2.80.

The Eq. 2.147 is formally similar to that used in 3D-SPH. Thus one can benefit from the well known features of the artificial viscosity in 3D, which can be directly

translated to the axisymmetric version. For example we have used the corrections to the AV of Balsara [5] in various simulations of the stagnation phase of the ICF capsules (see Subsec. 4.1.4) with good results. Alternative formulations of AV such as that proposed by Monaghan [44] inspired in Riemann solver schemes can be easily accommodated in *AxisSPH*. The similarity of cartesian and cylindrical formulations also allows to write a suitable energy equation for the artificial viscosity contribution

$$\left(\frac{du_i}{dt}\right)_{vis} = \frac{1}{2}\sum_{j=1}^{N} m_j \Pi_{ij}^{2D}(\mathbf{v_i} - \mathbf{v_j}) \cdot \mathbf{D}_i W_{ij}\,, \tag{2.148}$$

which has to be added to the right-hand side of Eq. 2.103.

2.10 Self-gravity in *AxisSPH*

In many astrophysical applications self-gravity can not be ignored. In principle, to calculate the gravitational force related to the particle i it is necessary to sum the contributions of the all the remaining particles, leading to a N^2 calculation that it is not feasible when the number of particles is high, as in current SPH astrophysical simulations.

To make the calculation feasible several interesting approaches have been developed. One of the most used, based in hierarchical-tree methods, was developed by Hernquist and Katz [29]. This method preserves the gridless nature of SPH and reduces the time calculation from $\propto N^2$ to $\propto NlogN$. Basically it works by grouping the neighbors particles to clusters, neigbors clusters to clusters of clusters, and so on. Then forces of distant particles are approximated by a multipole expansion of the force of the cluster where these particles are located.

Unfortunately that method does not work well in the two-dimensional axisymmetric approach because particles are, in fact, rings of different sizes. For the majority of particles the ratio between the radius of these rings and the distance to the point where the force needs to be calculated is too large to permit the multipolar approximation. Therefore a different approach has to be taken.

2.10.1 Direct gravitational force calculation

The good resolution achieved in two dimensions using a low or moderate number of particles N, makes the direct calculation of gravity affordable in many cases.

The gravitational force per unit of mass in a point P created by any distribution of mass is

$$\mathbf{g} = G \int_V \frac{\rho dV}{w^3} \mathbf{w} \,, \tag{2.149}$$

where $\mathbf{w}$ represents the vector connecting the point P to the differential element in the volume integration.

Placing the point P in the plane ZY with coordinates $(0, y_p, z_p)$, and considering that the differential elements of volume are rings with symmetry around the Z axis, we can reduce the integration to the azimuthal φ angle. So, according to Fig. 2.8 we can express $\mathbf{w} = \mathbf{R} - \mathbf{s'}$, and $\mathbf{g}_p$ can be rewritten as

$$\mathbf{g}_p = G \int_0^{2\pi} \frac{\rho R d\varphi}{(R^2 + s'^2 - 2y_p R \sin\varphi)^{3/2}} \times [(R\sin\varphi - y_p)\mathbf{j} + (z - z_p)\mathbf{k}] \,, \tag{2.150}$$

where $\mathbf{j}$ and $\mathbf{k}$ are the Cartesian orthogonal unit vectors and because

$$(R^2 + s'^2 - 2y_p R \sin\varphi)^{3/2} = (R^2 + s'^2)^{3/2} \left[1 - \tau sin\varphi\right]^{3/2} \,, \tag{2.151}$$

the denominator can be expressed in terms of the parameter τ

$$\tau = \frac{2y_i R_j}{R_j^2 + s'^2_i} \,. \tag{2.152}$$

So we can write the gravitational force acting onto the i^{th}-particle as

$$\mathbf{g}_i = \frac{G}{2\pi} \sum_{j=1}^{N} \frac{m_j}{(R_j^2 + s'^2_i)^{3/2}} \times [(R_j I_1 - y_i I_2)\mathbf{j} + (z_j - z_i) I_2 \mathbf{k}] \,, \tag{2.153}$$

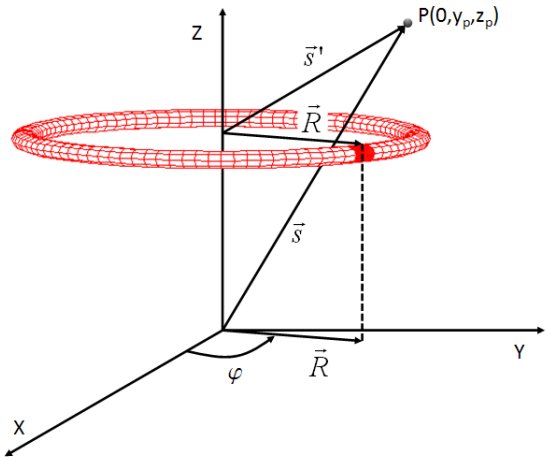

Figure 2.8: Schematic representation of the 2D-cylindrical coordinate system. The torus represents the actual 3D shape of the particles in this axisymmetric system. Point P belongs to the YZ-plane.

where $s'^2_i = y_i^2 + (z_j - z_i)^2$ and m_j is the mass of the particle associated to the j^{th}-ring. Integrals I_1 and I_2 are defined by

$$I_1 = \int_0^{2\pi} \frac{\sin\varphi d\varphi}{(1-\tau\sin\varphi)^{3/2}}\,, \tag{2.154}$$

$$I_2 = \int_0^{2\pi} \frac{d\varphi}{(1-\tau\sin\varphi)^{3/2}}\,, \tag{2.155}$$

in terms of the parameter τ defined by Eq. 2.152.

Unfortunately, the elliptical integrals I_1 and I_2 (Eq. 2.154 and Eq. 2.155) can not be solved analytically. It can be shown, however, that the value of τ is always inside $\tau\epsilon[0,1)$, although for $\tau \to 1$ the integrals I_1 and I_2 become divergent.

A practical procedure to compute gravity using the direct force calculation which we have successfully used in the simulations is the following:

(1) Build a table for I_1 and I_2 as a function of τ. A table with 10^4 rows with values $0 \leq \tau \leq 0.9999$ evenly spaced is sufficient. In the left panel of Fig. 2.9 we have represented these values.

(2) To increase the speed do not interpolate from that table but take just the row which is closest to the actual value of τ calculated using Eq. 2.152.

(3) Note that parameter τ is symmetric with respect to any pair of particles, $\tau_i = \tau_j$, thus $I_1(\tau_i) = I_1(\tau_j)$ and similarly for I_2. Therefore only a half of the interactions have to be calculated and hence the computational load scales as $N(N-1)/2$.

If the algorithm is well optimized, this scheme is able to provide the exact value of the self-gravity for several dozens of thousand particles in today desktop computers. In many applications using $\approx 50,000$ particles in 2D is enough to guarantee a good resolution.

2.10.2 Calculation of gravity using the gravitational potential

Taking the gradient of the gravitational potential is another route to calculate the gravity. It is more efficient that the evaluation of the Eq. 2.153 because calculating the potential V involves a lower number of operations. As gravity is calculated taking the SPH gradient of V it can be computed in the same loop used to calculate density. Additionally this method avoids undesirable numerical divergences when a pair of particles becomes too close, due to the smoothing effect of the kernel interpolation.

The contribution of the j-ring with mass m_j in the position of the i-particle to the gravitational potential is

$$\begin{aligned} V_i &= -G \int_0^{2\pi} \frac{\rho R d\varphi}{w} \\ &= -G \int_0^{2\pi} \frac{\rho R d\varphi}{(R^2 + s'^2 - 2y_p R \sin\varphi)^{1/2}} \,, \end{aligned} \tag{2.156}$$

we can rewrite the denominator in the same way as in Eq. 2.151, but now the angular contribution is related to I_3 defined as

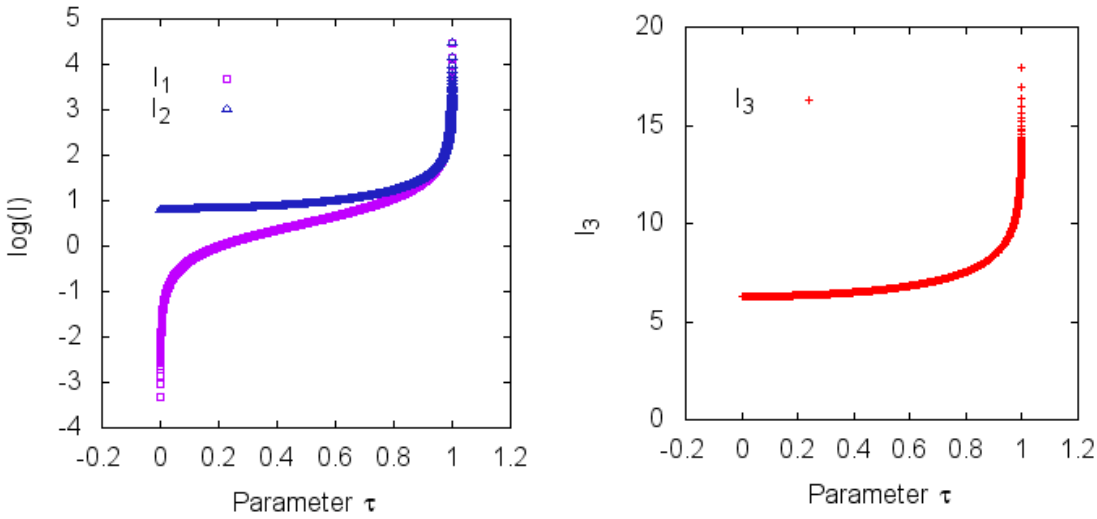

Figure 2.9: Values of the integrals I_1 (Eq. 2.154), I_2 (Eq. 2.155) and I_3 (Eq. 2.157) as a function of the parameter τ (Eq. 2.152).

$$I_3 = \int_0^{2\pi} \frac{d\varphi}{(1-\tau\sin\varphi)^{1/2}}\,, \tag{2.157}$$

In the right panel of Fig. 2.9 it is represented the value of the definite integral I_3 in function of the parameter τ (Eq. 2.152), taking values from 0 to 1 in intervals of $\Delta\tau = 10^{-4}$. Then we can write the potential of the i-particle as

$$V_i = -\frac{G}{2\pi}\sum_{j=1}^{N}\frac{m_j}{(R_j^2+s_i'^2)^{1/2}}I_3\,. \tag{2.158}$$

The gravitational energy U, of the system can be evaluated in the usual way as

$$U = \frac{1}{2}\sum_{j=1}^{N} m_j V_j\,, \tag{2.159}$$

which is useful to check total energy conservation.

Having V, we compute the gravitational force per unit of mass as

$$\mathbf{g_i} = -(\mathbf{D}V)_i \,, \tag{2.160}$$

which can be obtained using Eq. 2.116, the corrected density $\hat{\eta}$, and the operator $\mathbf{D}_i$ (Eq. 2.109)

$$\mathbf{g_i} = \sum_{j=1}^{N} \frac{m_j}{\hat{\eta}_j} \left(V_i - V_j\right) \mathbf{D}_i W_{ij} \,, \tag{2.161}$$

or (see also subsection *"First derivatives"* of [45])

$$\mathbf{g_i} = \frac{1}{\hat{\eta}_i} \sum_{j=1}^{N} m_j \left(V_i - V_j\right) \mathbf{D}_i W_{ij} \,, \tag{2.162}$$

We have obtained the value of the derivative using one of the "golden rules" of SPH that recommends to make the derivative with the density placed inside the operator.

$$\mathbf{D}_i V_i = \frac{1}{\widehat{\eta_i}} \left[\mathbf{D}_i (\widehat{\eta_i V_i}) - V_i \mathbf{D}_i \widehat{\eta_i} \right] \,, \tag{2.163}$$

and using the following approximation (see Eq. 2.43)

$$\widehat{\eta_i V_i} = f_1^i \sum_{j=1}^{N} \, m_j V_j W_{ij} \,, \tag{2.164}$$

before applying the operator $\mathbf{D}_i$, where f_1 is the correction factor given by Eq. 2.41. To obtain the first component $\frac{\partial}{\partial r}$ of the corrected density $\widehat{\eta_i}$ we must remember Eq. 2.67 that includes the derivative of f_1. After easy algebra we can write

$$\mathbf{g_i} = \frac{f_1^i}{\widehat{\eta_i}} \sum_{j=1}^{N} m_j (V_i - V_j) \mathbf{D}_i W_{ij} + \frac{\left(\frac{df_1^i}{dr}\right)}{\widehat{\eta_i}} \sum_{j=1}^{N} m_j (V_i - V_j) W_{ij} \cdot \mathbf{u}_r \,, \tag{2.165}$$

where $\mathbf{u}_r$ represents the unit vector in the r-axis.

Notice that when particles are far from the z-axis, $f_1 \to 1$, $\frac{df_1^i}{dr} \to 0$ (see Fig.2.6), and the above equation becomes Eq. 2.162.

2.10.3 The free fall collapse with and without rotation

In order to check the ability of Eq. 2.165 to evaluate the gravitational force we present a simple test with analytical solution: the free fall collapse of a uniform sphere of mass M_0 and radius R_0 for which pressure and viscosity forces were set to zero, and the momentum equation is just governed by the gravitational force. The evolution during the free-fall is highly non-linear, so it has become a standard test to check the ability of any algorithm devised to compute the gravitational force.

The solution (see for example [15]) gives the radial position $r(t)$ of any fluid element as a function of its radial position a $t = 0$ s

$$\frac{t}{t_{ff}} = 1 - \frac{2}{\pi}\left\{\sin^{-1}\left[\left(\frac{r}{r_0}\right)^{\frac{1}{2}}\right] - \left(\frac{r}{r_0}\right)^{\frac{1}{2}}\left(1 - \frac{r}{r_0}\right)^{\frac{1}{2}}\right\}, \tag{2.166}$$

where t_{ff} is the free-fall time defined as

$$t_{ff} = \frac{\pi}{2}\left(\frac{R_0^3}{2GM_0}\right)^{\frac{1}{2}}, \tag{2.167}$$

We have taken $M_0 = M_\odot$ and $R = R_\odot$ and 15,396 particles, initially placed in a square lattice.

In Fig. 2.10 it is depicted the evolution of a particle placed at $r_0 = \frac{2}{3}R_\odot$ from $t = 0$ until $t \simeq t_{ff}$. The analytical solution given by Eq. 2.166 is very well reproduced.

As it is well known, rotation is present in many real scenarios, particularly in the astrophysical context: stars, planets and similar bodies spin around their axes, and sometimes, it is possible to idealize them as rigid bodies (for example rotating neutron stars). Other times rotation involves a more complex dynamics as for example accretion discs around stars or stellar remnants belonging to a compact binary system, or black holes in the center of spiral galaxies where the orbiting material loses angular momentum and fall onto the central massive object. Generally there

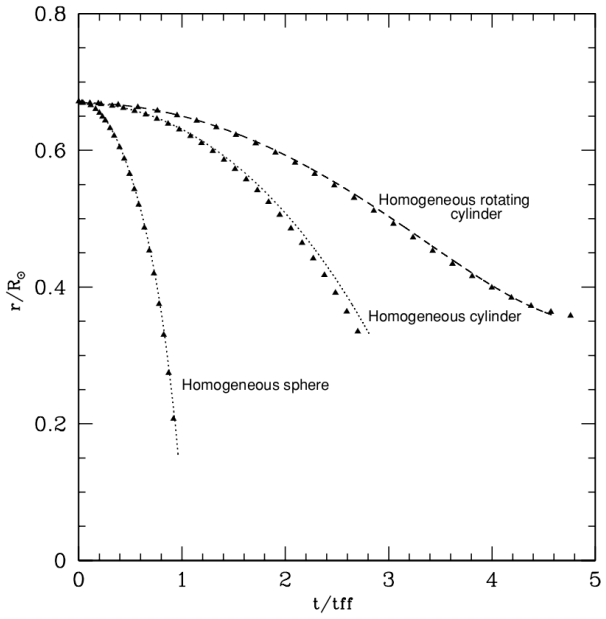

Figure 2.10: Evolution of a particle ($r_0 = 2/3R_\odot$, $z_0 = 0$) in a free fall test in three cases: for a non rotating sphere and a rotating and non rotating cylinder (dots). The analytical solution is represented with full triangles.

is differential rotation due to the coupling effect of viscosity. Nevertheless if the characteristic dynamical time is much shorter than the viscous coupling time the effect of viscosity can be neglected.

In the 2D axisymmetric codes rotation can be easily implemented by adding a centrifugal force to the r-component of the gravity. The viscous term is set to zero and the time-dependent angular velocity of each particle can be inferred just applying angular momentum conservation.

For this viscosity free case we have chosen a slender rotating cylinder of uniform density represented with $N = 70,000$ particles spread in a square lattice which rotates with the same initial angular velocity. The total mass is $M_{cyl} = M_\odot$, and size $R_{cyl} = R_\odot$, $Z_{cyl} = 20R_{cyl}$. We study the radial evolution of a particle at $z \simeq 0$, and initial distance to the z-axis, $r_0 = 2/3R_\odot$.

The specific angular momentum conservation implies $L_z(r_0) = L_z(r,t)$ and the centrifugal acceleration of the particle can be expressed as

$$a_c = \frac{L_z^2(r,t)}{r^3} = \frac{L_0^2}{r^3}\,, \tag{2.168}$$

where $L_0 \equiv L_z(r_0)$. On the other hand, the Gauss law guarantees that the radial gravitational acceleration g depends only on the mass m enclosed by the cylinder defined by the radial position of the particle, r. The relation of g with its initial value g_0 is

$$\frac{g}{g_0} = \frac{mr_0}{m_0 r}\,, \tag{2.169}$$

because of $m = m_0$ (particles does not change their mass), and adding both contributions to the radial acceleration, we finally write

$$\ddot{r} = -g + a_c = -g_0\frac{r_0}{r} + \frac{L_0^2}{r^3}\,, \tag{2.170}$$

Integrating, and using $\dot{r}|_{t=0} = 0$, we obtain the radial velocity of the particle

$$\dot{r} = -\left[-2g_0 r_0 \ln\left(\frac{r}{r_0}\right) + L_0^2\left(\frac{1}{r_0^2} - \frac{1}{r^2}\right)\right]^{\frac{1}{2}}\,. \tag{2.171}$$

Integrating again we get the radial evolution of the particle. However this second integral has to be solved numerically once r_0 and L_0 are specified

$$t(r) = -\int_{r_0}^{r}\left[-2g_0 r_0 \ln\left(\frac{r'}{r_0}\right) + L_0^2\left(\frac{1}{r_0^2} - \frac{1}{r'^2}\right)\right]^{-\frac{1}{2}} dr'\,. \tag{2.172}$$

Such semianalytical solution is depicted in Fig. 2.10 (full triangles, *"Homogeneous rotating cylinder"*) for $r_0 = 2/3R_{cyl}$ and $L_0 = \sqrt{0.5 g_0 r_0^3}$, so that the centrifugal force at r_0 its a half of the gravitational force. A comparison to the SPH simulation with pressure and artificial viscosity set to zero can be seen in the same figure. The agreement is not as good as in the spherical case for $t > t_{ff}$. This is not surprising because the boundary effects at cylinder edges progressively affect gravity at current particle test position and its evolution is very sensible to small variations of gravity force.

Because pressure forces were set to zero the cylinder is initially compressed by the gravity action. As collapse ensues the angular velocity must be increased to preserve angular momentum, resulting in a increase of the centrifugal force. When $t \approx 5t_{ff}$ the two forces become similar and r tends to a constant value.

The effect of rotation can be better understood by comparing the evolution of the same cylinder without angular velocity. The analytical solution and the simulated positions are also depicted in Fig. 2.10 (*"homogeneous cylinder"*). In this case the match of both curves is not as good as in the previous case because the particle evolution is only driven by gravity, which is sensible to the finite size of the cylinder and is not smoothed by the centrifugal term.

Chapter 3

Basic Tests

The formalism developed in the precedent chapters needs to be validated using different tests. These tests were carefully chosen to check one or a few pieces of physics included in the algorithm of calculation. In some cases the tests have an analytical solution to directly compare with the output of *AxisSPH*. Other tests cases corresponds to situations for which there is not an avalaible analytical solution but the system has spherical symmetry so that the output of the SPH code can be compared to the results of standard 1D lagrangian hydrodynamics. Tests belonging to the first group are the evolution of a thermal continuity, aimed at checking the heat conduction equation, and the wall heating shock test intended to check the ability of the code to handle with strong shock waves. For the second group we have chosen the implosion of a homogeneous capsule induced by the ablation of its surface, a simplified problem related to interesting applications, and the gravitational collapse of a polytrope. This last case is obviously oriented to check the gravitational module included in *AxisSPH*. Finally an intrinsic 2D test with axial symmetry, the supersonic collision of two streams of gas, was discussed. In this case the study was focussed on the detailed evolution of momentum and energy of the two bubbles. A summary of the main features of many of the calculated models is provided in Tab. 3.1.

Once *AxisSPH* has successfully passed these basic tests it will be applied to a more sophisticated (and realistic) systems in Chapter 4.

3.1 Summary of equations

Hereafter the Euler equations used in the different tests and applications are:

(1) Mass conservation.

$$\widehat{\eta}_i = \sum_{j=1}^{N} m_j W_{ij} \times f_1^i = \eta_i \times f_1^i \,. \tag{3.1}$$

(2) Momentum conservation.

$$\begin{aligned} \ddot{r}_i = 2\pi \frac{P_i}{\widehat{\eta}_i} - 2\pi \sum_{j=1}^{N} \left[m_j \left(\frac{P_i r_i}{\widehat{\eta}_i^2} \times f_1^i(\zeta_i) + \frac{P_j r_j}{\widehat{\eta}_j^2} + \Pi_{ij}^{2D} \right) \frac{\partial W_{ij}}{\partial r_i} \right] \\ - \left(\frac{2\pi P_i \; r_i}{\widehat{\eta}_i \times f_1^i} \right) \; \frac{df_1^i(\zeta_i)}{dr_i} \,. \end{aligned} \tag{3.2}$$

$$\ddot{z}_i = -2\pi \sum_{j=1}^{N} m_j \left(\frac{P_i r_i}{\widehat{\eta}_i^{\,2}} \times f_1^i(\zeta_i) + \frac{P_j r_j}{\widehat{\eta}_j^{\,2}} + \Pi_{ij}^{2D} \right) \frac{\partial W_{ij}}{\partial z_i} \,. \tag{3.3}$$

(3) Energy conservation.

$$\frac{du_i}{dt} = -2\pi \frac{P_i}{\widehat{\eta}_i} \; v_{r_i} + 2\pi \frac{P_i r_i}{\widehat{\eta}_i^{\,2}} \frac{d\widehat{\eta}_i}{dt} + \frac{1}{2} \sum_{j=1}^{N} m_j \Pi_{ij}^{2D} (\mathbf{v_i} - \mathbf{v_j}) \cdot \mathbf{D}_i W_{ij} \,. \tag{3.4}$$

$$\begin{aligned} \frac{d\widehat{\eta}_i}{dt} = \sum_{j=1}^{N} m_j \left(f_1^i v_{r_i} - f_2^i v_{r_j} \right) \frac{\partial W_{ij}}{\partial r_i} + \sum_{j=1}^{N} m_j \left(\frac{\partial f_1^i}{\partial r_i} v_{r_i} - \frac{\partial f_2^i}{\partial r_i} v_{r_j} \right) W_{ij} \\ + f_1^i \sum_{j=1}^{N} m_j \left(v_{z_i} - v_{z_j} \right) \frac{\partial W_{ij}}{\partial z_i} \,. \end{aligned} \tag{3.5}$$

(4) Correction factors for the cubic spline kernel (for the one-parameter family of interpolating kernels $W_n^H(v,h)$ see Appendix B)

$$f_1^i(\zeta) = \begin{cases} \left[\frac{7}{15}\zeta_i^{-1} + \frac{2}{3}\zeta_i - \frac{1}{6}\zeta_i^3 + \frac{1}{20}\zeta_i^4 \right]^{-1} & \text{if } 0 < \zeta_i < 1 \\ \left[\frac{8}{15}\zeta_i^{-1} - \frac{1}{3} + \frac{4}{3}\zeta_i - \frac{2}{3}\zeta_i^2 + \frac{1}{6}\zeta_i^3 - \frac{1}{60}\zeta_i^4 \right]^{-1} & \text{if } 1 < \zeta_i < 2 \\ 1 & \text{if } \zeta_i > 2 \end{cases} . \tag{3.6}$$

$$f_2^i(\zeta) = \begin{cases} \left[\frac{14}{15}\zeta_i^{-1} + \frac{4}{9}\zeta_i - \frac{1}{15}\zeta_i^3 + \frac{1}{60}\zeta_i^4\right]^{-1} & \text{if } 0 < \zeta_i < 1 \\ \left[-\frac{1}{45}\zeta_i^{-2} + \frac{16}{15}\zeta_i^{-1} - \frac{1}{3} + \frac{8}{9}\zeta_i - \frac{1}{3}\zeta_i^2 + \frac{1}{15}\zeta_i^3 - \frac{1}{180}\zeta_i^4\right]^{-1} & \text{if } 1 < \zeta_i < 2 \\ 1 & \text{if } \zeta_i > 2 \end{cases} . \tag{3.7}$$

(5) Artificial viscosity.

$$\Pi_{ij}^{2D} = \Pi_{ij}^{(1)} + \Pi_{ij}^{(2)} . \tag{3.8}$$

$$\Pi_{ij}^{(1)} = \begin{cases} \frac{-\alpha_0 \bar{c_{ij}} \mu_{ij} + \beta_0 \mu_{ij}^2}{\bar{\rho}_{ij}} & \text{if } \mathbf{v}_{ij} \cdot \mathbf{s}_{ij} < 0 \\ 0 & \text{if } \mathbf{v}_{ij} \cdot \mathbf{s}_{ij} \geq 0 \end{cases} , \tag{3.9}$$

where

$$\mu_{ij} = \frac{\bar{h}_{ij} \mathbf{v}_{ij} \cdot \mathbf{s}_{ij}}{s_{ij}^2 + \nu^2} . \tag{3.10}$$

$$\Pi_{ij}^{(2)} = \begin{cases} \frac{-\alpha_1 \bar{c_{ij}} q_{ij} + \beta_1 q_{ij}^2}{\bar{\rho}_{ij}} & \text{if } v_{r_i} < 0 \quad \wedge \quad v_{r_j} < 0 \\ 0 & \text{other cases} \end{cases} , \tag{3.11}$$

where

$$q_{ij} = \frac{1}{2}\left(\frac{h_i v_{r_i}}{r_i} + \frac{h_j v_{r_j}}{r_j}\right) . \tag{3.12}$$

3.2 Thermal wave

As in the r-component of the momentum equation (Eq. 3.2) the heat transfer equation in the axisymmetric approach includes an additional term which accounts for the geometrical convergence of the flux towards the symmetry axis (Eq. 2.117). Such new term is relevant to simulate heat fluxes in the axis neighborhood as it could be the case of heat diffusion from a pointlike region. In the following test we describe the evolution of a thermal discontinuity initially seeded at the center of a two dimensional distribution of 57,908 particles until the initial thermal content has been

considerably smeared by diffusive conduction. The evolution of the internal energy was compared to the analytical prediction.

The initial model was obtained by setting the particles evenly in a square lattice. The mass of the particles was conveniently adjusted to reproduce a previously chosen density profile. For example, to obtain the distribution with constant density $\rho_0 = 1\ g/cm^3$ considered in this test it was necessary to give the particles a mass proportional to their r-coordinate. During the calculation we left the particles at rest so that the energy equation, Eq. 3.4, reduces to the heat transport equation Eq. 2.104. The initial pointlike discontinuity in energy was smoothed using a sharp Gaussian of characteristic width a few times the smoothing length parameter. Such delta-like jump in internal energy originates a thermal wave front which evolves according to[1]

$$u(r,z,t) = \frac{A}{(4\pi\alpha t)^{\frac{3}{2}}} \exp\left(-\frac{r^2+z^2}{4\alpha t}\right) + u_0\,, \tag{3.13}$$

where α is the thermal diffusivity, k is the thermal conductivity $k = \alpha c_v \rho$ and c_v is the specific heat capacity. The following set of values were taken $A = 10^5\ erg\ cm^3/g$, $u_0 = 10^3\ erg/g$ and $\alpha = 1\ cm^2/s$. The initial internal energy profile was that given by Eq. 3.13 for $t = 1\ s$, which was taken as the initial time ($t_0 = 0\ s$) for the SPH simulation. The evolution of the thermal signal is then uniquely controlled by the heat conduction equation.

In Fig. 3.1 (left) it is depicted the profile $u(r)$ of the specific internal energy at several times. As we can see the profiles obtained using *AxisSPH* fit the analytical solution almost perfectly. As times goes on the peak of the signal and its slope decreases due to heat diffusion. The initial discontinuity is rapidly smeared out by thermal diffusion and soon a thermal wave is born which moves to higher r-coordinates, equalizing the internal energy of the system. At $t = 5\ s$ the profile of the internal energy is rather flat and the system is approaching thermal equilibrium. At $t = 5\ s$ the total internal energy was conserved up to $|\Delta E|/E_0 \simeq 2 \cdot 10^{-6}$.

In Fig. 3.1 (right) we show the evolution of the internal energy profile obtained when the first term on the right side of Eq. 2.117 is removed. In this case the

[1] I would like to take this opportunity to correct a typographical error which appears in Eq. (52) of [24] where the factor $c_v k$ has to be α as in Eq. 3.13

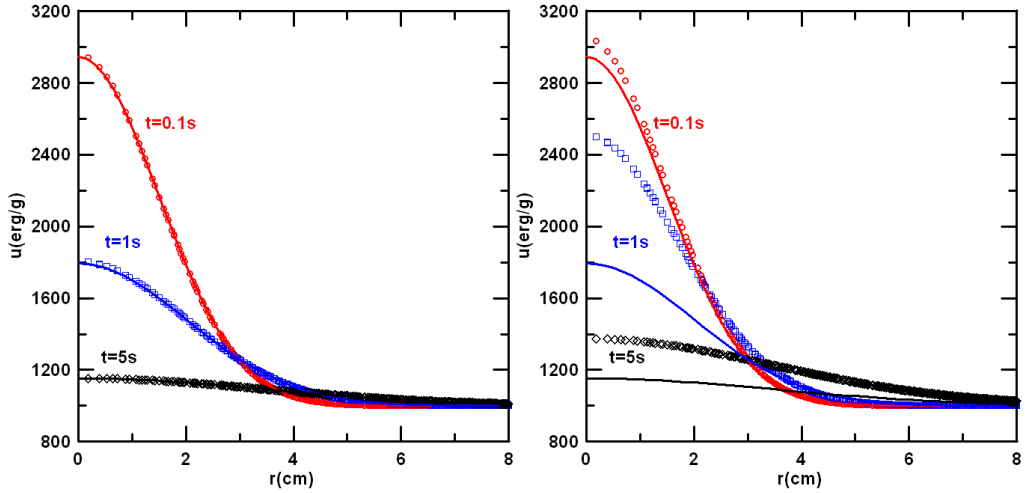

Figure 3.1: Evolution of a thermal discontinuity initially seeded around the symmetry axis. The profile of the internal energy at different times is well reproduced by the SPH when the hoop-stress term is included (left). However when that term is neglected the result does not match the analytical solution represented by the continuum line (right).

deviation from the analytical solution is large. Therefore it is important to include that new term, especially in those calculations dealing with strong thermal gradients, at or near, the symmetry axis.

3.3 The Wall Heating shock Test

The so called wall heating shock test, [52], was especially devised to check the ability of hydrocodes to handle with strong shocks. In this test a sphere or a cylinder implode by conveniently setting a converging initial velocity profile to the computational cells. For these geometries, simulations can be compared to the predictions of an analytical approach to the evolution of thermodynamical variables as a function of the initial conditions. Although the gross features of the event are correctly captured by SPH simulations it is well known that schemes which rely in artificial viscosity have difficulties to give a detailed description of the wall heating test. The reason is that artificial viscosity spreads the shock over several computational cells, inducing an unphysical rise of internal energy ahead the shock. For converging flows a large artificial spike in internal energy is observed around the convergence region. As a consequence a pronounced dip in the density profile appears to keep the pres-

sure field smooth. Both, the dip and the spike are numerical artefacts which can be smoothed with an adequate level of heat conduction to spread the excess of internal energy on the adjacent computational cells (or particles). On the other hand the inclusion of a good amount of artificial viscosity is mandatory to handle the shock.

The wall heating shock is of particular relevance to check *AxisSPH* because:

(1) The implosion impels material just towards the singularity axis and therefore the inclusion of both, the hoop-stress terms and corrective f_1 and f_2 terms in Eq. 3.5 and Eq. 3.4 become crucial to handle the shock.

(2) The inclusion of the axis-converging part of artificial viscosity, Eq. 3.11, is also necessary.

(3) Heat conductive diffusion, Eq. 2.117, has to be kept in the energy equation to reduce the extent of the artificial spike in internal energy, especially for particles which move close to the singularity axis.

As in the previous test we have spread $N = 50,334$ particles in a square lattice with their mass conveniently crafted to reproduce an homogeneous system with initial radius $R_0 = 1\ cm$. The initial conditions were taken from Noh [52]: $\rho(s,0) = 1\ g/cm^3$; $v(s,0) = -1\ cm/s$; $u(s,0) = 0\ erg/g$. The exact solution at time $t = 0.6\ s$ for $\gamma = 5/3$ is shown in Fig 3.2 (dashed lines). The analytical profile is characterized by a constant post state until distance $s = 0.2\ cm$, followed by a rapid decrease in density and internal energy. In the shocked zone the density achieves a rather high, though constant, value of $\rho = 64\ g/cm^3$ while the internal energy was $u = 0.5\ erg/g$. The simulation of the implosion using *AxisSPH* without including heat diffusion leads to the density and energy profiles depicted in Fig. 3.2 (left). As we can see, the resulting profiles compare poorly with the analytical estimation in the shocked region. The error bars in the plot give the 1σ dispersion for these variables with respect to its main value in the shell. The dispersion is high, especially at low radius, a clear signature for the presence of numerical noise. Close to the axis we see the typical, but artificial, combination of a density dip and internal energy spike. The maximum density value was $\rho \simeq 58\ g/cm^3$, which is around 10 per cent lower than the exact value. The quality of the simulation is clearly improved when heat conduction is included in the energy equation, Fig. 3.2 (right). Recipes to set the artificial viscosity in SPH to better handle the wall heating test were given by

Monaghan [43] and Brookshaw [8]. We have used the recipe of Monaghan after adapting it to the particular features of the axisymmetric SPH defining an artificial conductivity for the i-particle

$$\kappa_i = \bar{\rho}_{ij}\bar{c}_{vij}(\bar{h}_{ij}\bar{c}_{ij} + 4|\mu_{ij}|)\,, \tag{3.14}$$

where $\bar{c}_{vij} = \frac{1}{2}(c_{vi} + c_{vj})$ is the symmetrized specific heat and μ_{ij} is the artificial viscosity parameter given by Eq. 2.142. Notice that expression Eq. 3.14 is symmetric so that $\kappa_i = \kappa_j$. As shown in Fig. 3.2 (right) the inclusion of the artificial heat conduction term leads to a significant improvements of the results. The dip in density is considerably reduced and the profiles, in density and internal energy, show a much lesser dispersion. Nevertheless the maximum peak in density still remains below the analytical expectation. In this respect, the only secure way to improve the results is to increase the number of particles, although the use of adaptive kernels (Owen et al. [56]; Cabezón et al. [10]), may also help to enhance the results.

3.4 Implosion of a homogeneous capsule

Another test which demands a careful handling of physics in the neighborhood of the symmetry axis is the implosion of a sphere induced by the ablation of its surface. This is a similar problem as the above described wall heating shock test but probably of greater interest because its close relation to ICF studies. Thus our third test deals with the implosion of a homogeneous spherical capsule of size $R_0 = 1\ cm$ and density $1\ g/cm^3$, induced by the ablation of its surface. The ablation of the capsule was triggered by the instantaneous deposition of energy in the outermost layers of the capsule. The added external energy was supposed to be totally stored as internal energy of the gas. The energy deposition profile was taken linear from $s = 0.8\ cm$ to $s = R_0 = 1\ cm$ so that the ratio of internal energies at these two fiducial points was $E_1(s = 1)/E_2(s = 0.8) = 10^4$. Below $s = 0.8\ cm$ a flat profile of internal energy was assumed. The rocket effect caused by the evaporation of the surface layers forms a strong shock wave which compresses the interior of the capsule. The convergence of the shock at the central region of the sphere increases the density and internal energy in a large factor. In Fig. 3.3 we show the density and radial velocity profiles at four different times resulting from the SPH calculation. These profiles are compared with

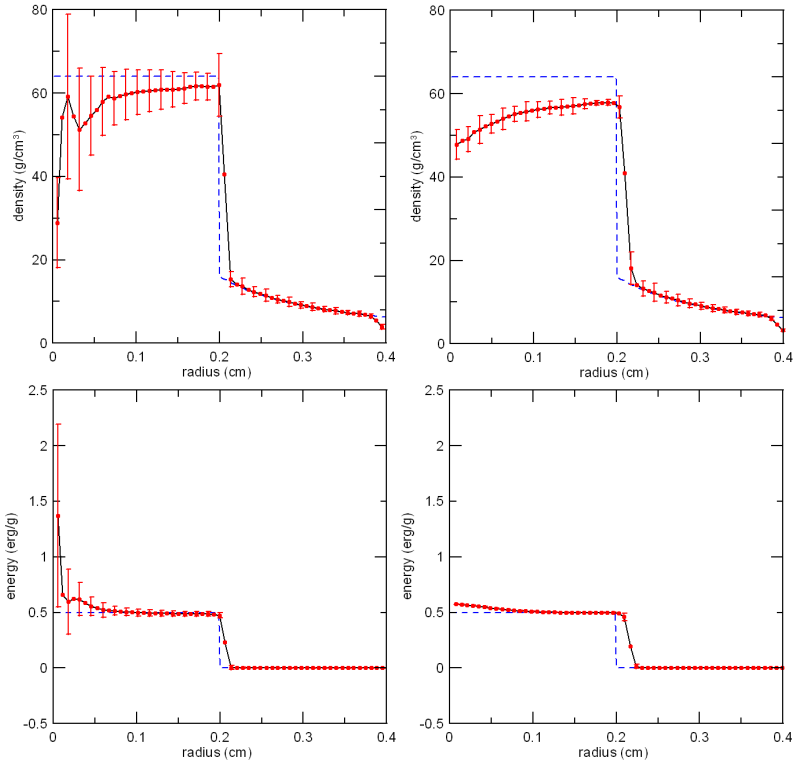

Figure 3.2: Results of the Noh test at $t = 0.6s$. Upper left-and right-hand side: averaged density profiles without and with the artificial heat conduction. Bottom-left and right-hand side: same but for internal energy. Dispersion around the averaged values is given by the error bars. The analytical solution is represented with dashed lines.

those obtained using a standard onedimensional lagrangian hydrocode [15] in the same figure (solid lines). A summary of the evolution of the capsule is as follows. Shortly after the initial energy deposition a pair of shock waves moving in opposite directions show up. Both waves are clearly visible in the profile corresponding to a time $t = 0.0044\ s$. As the reverse shock approaches the center it gains strength owing to the spherical convergence (profiles at $t = 0.0087\ s$ in Fig. 3.3). A maximum compression of the central region with $\rho_{max} = 32\ g/cm^3$ is achieved at $t = 0.0111\ s$, and then the wave reflects. Afterwards the decompression of the capsule is fast. At $t = 0.0150\ s$, the density peak has already dropped to 7 g/cm^3 and most of the material of the capsule is expanded homologously. At $t = 0.0264\ s$ the material of the capsule has undergone a severe dilution, $\rho(r) << 1\ g/cm^3$ and the radial velocity profile consists of two homologously expanding zones separated by a transition region at $s \simeq 1\ cm$. When the elapsed time was $t = 0.0264\ s$ the outermost layer of the sphere has expanded until $s = 10\ cm$, ten times the original size of the capsule. The

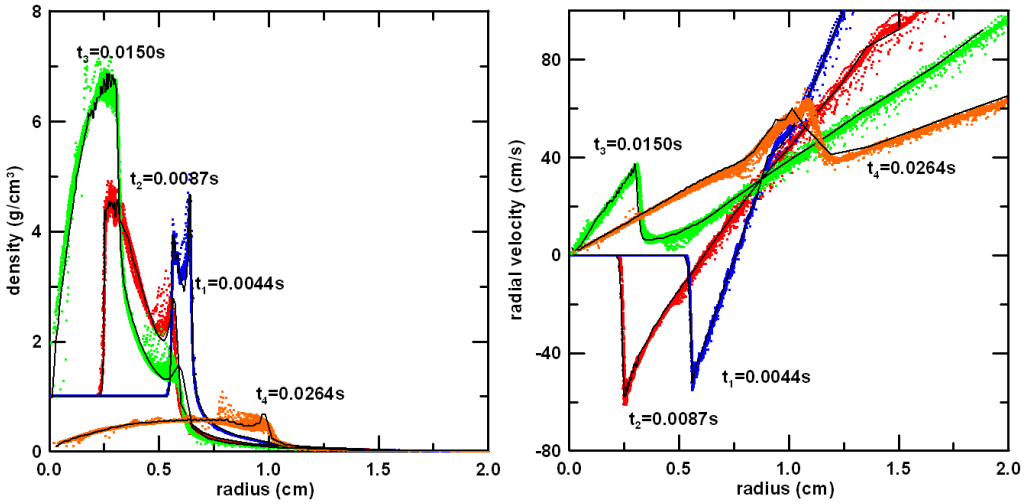

Figure 3.3: Density profile (left) and radial velocity (right) during the implosion and further rebound of a small capsule at different times. The black continuum line is the profile calculated using a one-dimensional hydrocode of similar resolution.

calculation carried out with *AxisSPH* matches quite well the one-dimensional results. The value of the central density at the moment of maximum compression is almost the same in both calculations (see Tab. 3.1). The conservation of momentum is very good, close to machine precision (Columns 5 and 6 in Tab. 3.1), while total energy was preserved better than 1% (last column in Tab. 3.1). On the negative side we see in Fig. 3.3 that there is a slight loss of the spherical symmetry, probably because of the initial distribution of particles in a regular lattice, which acts as a source of the so called hour-glass instability. Such instability arise from the preferred directions along the grid through which the stress propagates. The strong deceleration of the capsule during the compression phase amplifies the size of the hour-glass instability. Another point of small discrepancy between 1D and 2D calculations is that the SPH calculation is a bit delayed with respect its one-dimensional counterpart. For instance, the times at which the maximum central densities are achieved are $t_{1D} = 0.01095\ s$ and $t_{2D} = 0.0111\ s$, so that the relative difference was around 1-2 per cent. Such percent level of discrepancy remained approximately constant during the calculation.

Test	Particles	$\left(\frac{\rho_{max}}{\rho_0}\right)_{1D}$	$\left(\frac{\rho_{max}}{\rho_0}\right)_{2D}$	$\frac{\lvert\Delta\bar{r}\rvert}{R}$	$\frac{\lvert\Delta\bar{z}\rvert}{R}$	$\frac{\lvert\Delta E\rvert}{E_0}$
Polytrope	51,408	2.43	2.49	$5 \cdot 10^{-15}$	10^{-11}	$5 \cdot 10^{-3}$
Capsule implosion	30,448	29	32	$4 \cdot 10^{-14}$	10^{-11}	$8 \cdot 10^{-3}$
Noh test	50,334	64†	58	$6 \cdot 10^{-14}$	$3 \cdot 10^{-8}$	$2 \cdot 10^{-3}$

† Analytical value

Table 3.1: Main features of test models described in Sections 3.5, 3.4 and 3.3. Conservation of momentum is given by the displacement of the center of mass components $\Delta\bar{r} = [(\bar{r}(t) - \bar{r}_0) - \bar{v}_r^0 t]$ and $\Delta\bar{z} = [(\bar{z}(t) - \bar{z}_0) - \bar{v}_z^0 t]$ divided by the radius of the configuration at that time (columns 5 and 6). Momentum and energy conservation correspond to the last calculated model shown in Figures 3.6, 3.3, 3.2.

3.5 Gravitational collapse of a polytrope

The free fall test discussed in Subsec. 2.10.3 was devised to specifically check the algorithm implemented to calculate gravity. It is time now for a more complete test of *AxisSPH* by including the reaction of pressure forces against the collapsing gravity force. A spherically symmetric Sun-like polytrope was suddenly unstabilized by removing the 20% of its internal energy so that the structure implodes under the force of gravity. At some point the collapse in the central zone is halted and an accretion shock forms which moves through the incoming material to ultimately eject the surface layers of the polytrope. Several episodes of recontraction followed by mass loss ensued until the star sets in a new equilibrium state (see Fig. 3.4). Even though the scenario is not realistic, it contains several pieces of physics of great interest because accretion shocks and pulsational instabilities are very common in astrophysics. Conservation of the spherical symmetry after the first rebound is also a rather good test for the code. An additional advantage of considering an spherically symmetric initial model is that the evolution calculated with *AxisSPH* can be checked using standard Lagrangian hydrodynamics in one dimension.

The initial model was a $1M_{\odot}$ spherically symmetric polytrope of index $n = 3$. The radius was set equal to $1R_{\odot}$ so that the central density was $\rho_c = 77\ g/cm^3$. The one-dimensional equilibrium model was built by integrating the corresponding Lane-Endem equation of the polytrope [14]. The spherically symmetric density profile was then used to set the appropriate two-dimensional distribution of particles to be used

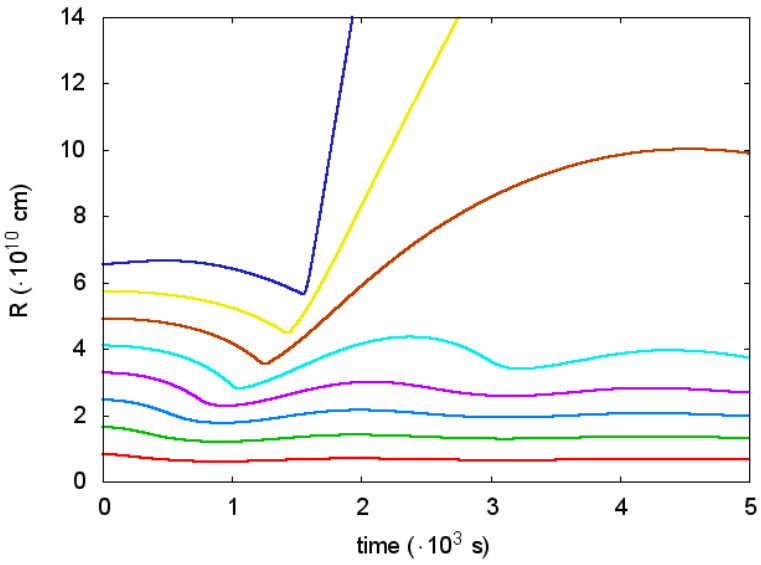

Figure 3.4: Temporal evolution of the position of different layers of a sun-like polytrope when 20% of its internal energy is removed. The calculation was carried out using a one-dimensional hydrocode.

in the SPH calculation. A sample of $N = 51,408$ particles was evenly distributed in a square lattice with their mass conveniently adjusted to reproduce the density profile of the polytrope. The EOS was that of an ideal gas with $\mu_i = 0.7$. In Fig. 3.5 there are shown the density (top) and gradient of pressure (bottom) profiles at t=0 s for all the mass points (dots) used in the simulation. These magnitudes have been calculated with and without the corrective term f_1, given by Eq. 2.41, in the *AxisSPH* code respectively. As we can see, the inclusion of the corrective term is crucial to get satisfactory profiles of gravity and gradient of pressure forces, enhancing the stability of the initial model. Only a handful of particles, representing a very small amount of mass, located at the surface of the star do not follow the one-dimensional profile.

Once the initial model was built it was perturbed by reducing the temperature everywhere in a 20% of its equilibrium value. Afterwards the evolution was followed with *AxisSPH*, from the implosion to the first pulsation, and compared to that obtained with the one-dimensional Lagrangian hydrocode [15]. In Tab. 3.1 and Fig. 3.6 there are shown the most relevant features of the evolution of the model. Soon after the model was destabilized, the polytrope started to collapse. The maximum compression of the central zone took place at $t = 960\ s$ with a density peak

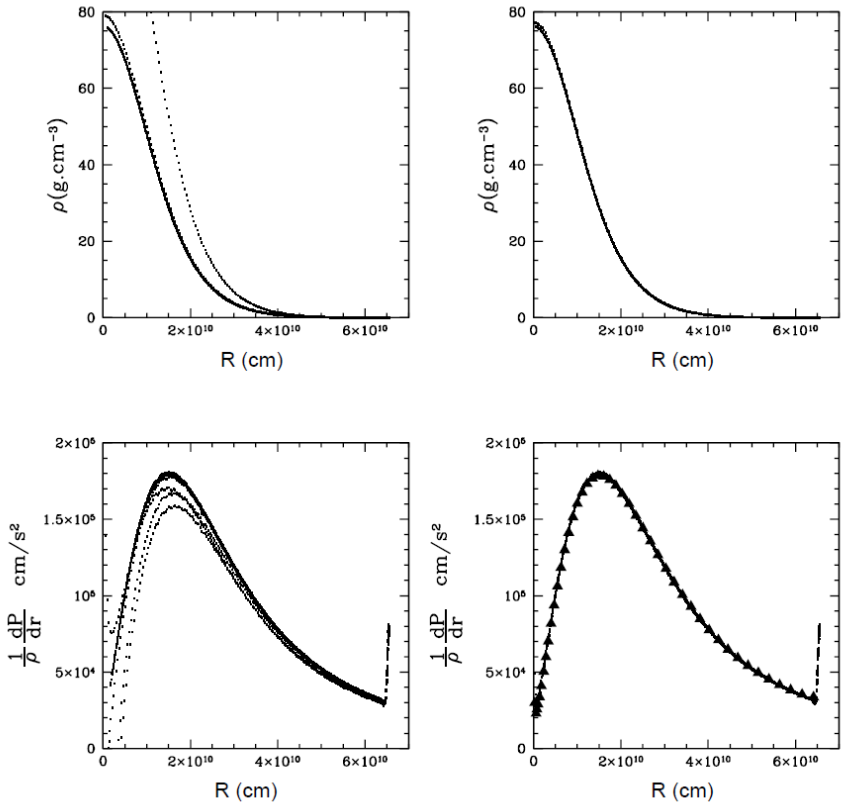

Figure 3.5: Density, gravity and pressure gradient profiles of the polytrope. Upper-left and right: density profile without and with axis corrections respectively. Bottom-left and right: the same but for the pressure gradient. The absolute value of gravity computed using the gradient of the gravitational potential calculated using Eq. 2.165 is marked with full triangles (bottom-right). All mass points of the polytrope have been represented. Neglecting axis corrections leads to a much larger dispersion in the profiles.

of $\rho_{max} = 192.8\ g/cm^3$. A slightly lower value, $\rho^{1D}_{max} = 187.1\ g/cm^3$ was obtained using the 1D code. The profiles of density and radial velocity at different times are depicted in Fig. 3.6. As we can see, the evolution calculated in one and two dimensions is very similar and, in general, both profiles are in good agreement. At the last calculated time, $t = 1,545\ s$, the shock is already breaking out the surface of the polytrope. Shortly after that time, some mass is ejected from the surface and, as the one dimensional calculation shows, the star embarks in a long pulsational stage (see Fig. 3.4).

Therefore we conclude that the numerical scheme is able to handle with this sort

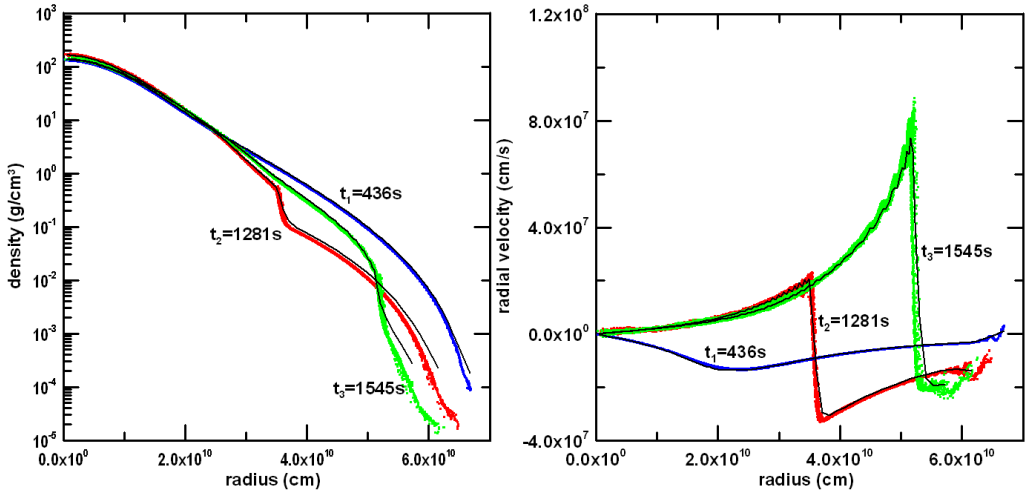

Figure 3.6: Density profile (left) and radial velocity (right) during the implosion and further rebound of the polytrope at different times. The black continuum line is the profile calculated using a one-dimensional hydrocode of similar resolution. At t=1,545 s the shock wave is breaking the surface of the star. In the figure all particles used during the calculation are shown.

of scenarios. The algorithm devised to calculate gravity, Eq. 2.165, was working adequately. The artificial viscosity module was also able to keep track with the shocks although, at some stages, the post-shock region showed a small amount of spurious oscillation (see the radial velocity profile at $t = 1,545\ s$ in Fig. 3.6). On the other hand there is an excellent momentum conservation, close to machine precision, whereas the conservation of energy was more modest, $|\Delta E|/E_0 \simeq 0.5\%$. The spherical symmetry was well preserved during the calculation. As in the implosion of the homogeneous capsule (Sec. 3.4) we found a small time-delay between the one and two-dimensional calculations (for example the maximum density is not achieved exactly at the same elapsed time in both codes). The relative shift in time remained approximately constant, around a 1.5 per cent, during the evolution. For the sake of clarity, the elapsed times shown in Fig. 3.6 were that of the SPH simulation and the times of the 1D simulation were conveniently shifted to better fit the density and radial velocity profiles.

3.6 Collision of two streams of gas

The supersonic collision of two bubbles of gas of different size and mass is a test specifically addressed to check momentum conservation in a very anisotropic situation. It is also a true multidimensional problem in the sense that the problem has neither spherical nor cylindrical symmetry. It can, however, be handled with *Axis-SPH* in the special case of head on collision of the bubbles because the problem has the adequate symmetry around the line of impact joining the center of both bubbles. A similar, but much complex, situation will be analyzed in the chapter of this Thesis devoted to study the collision of a pair of white dwarfs stars (Sec. 4.3). Therefore the results presented in this section have a great interests for astrophysics because the head on collision of streams of gas is a limiting case of collision of astronomical bodies.

The homogeneous spherical clouds of gas have different radius and masses $R_1 = 1\ cm$, $R_2 = 3\ cm$, $M_1 = 4\pi/3\ g$ and $M_2 = 36\pi\ g$ respectively, so that they have the same density $\rho_1 = \rho_2 = 1\ g/cm^3$. The initial thermal content of the bubbles was supposed to be negligible, $u_1^0 = u_2^0 = 10^{-3}\ erg/g$. The biggest sphere is at rest with its center located at the coordinate origin $(0, 0)\ cm$ while the center of the smaller one was located at $(0, -5)\ cm$ and moves towards the bigger with velocity $v_z^0 = 10\ cm/s$. The EOS of both clouds obeys an ideal gas law with adiabatic index $\gamma = 5/3$. The number of particles in each sphere is $N_1 = 5,480$ and $N_2 = 50,334$, respectively, settled in a square lattice. With that initial conditions the Mach number is $M_s^0 = 300$, thus the impact is highly supersonic.

In Fig. 3.7 there is depicted a color map of the evolution of density during the collision. In the second image we see the high increase in density due to the face on impact of the two clouds. The impact is so strong that it becomes difficult even to distinguish the shape of the smaller sphere in the last snapshot. Therefore the large mass contrast leads to the complete deformation of the smaller sphere which, in the end transfers most of its initial linear momentum to the larger bubble. In order to better understand the evolution of momentum and the balance between the kinetic and thermal energies of both structures the whole process can be roughly divided in three stages, represented in Fig. 3.7 and Fig. 3.8:

(1) For $0 \leq t \leq 0.5\ s$, the incoming smaller cloud deforms while a large fraction of

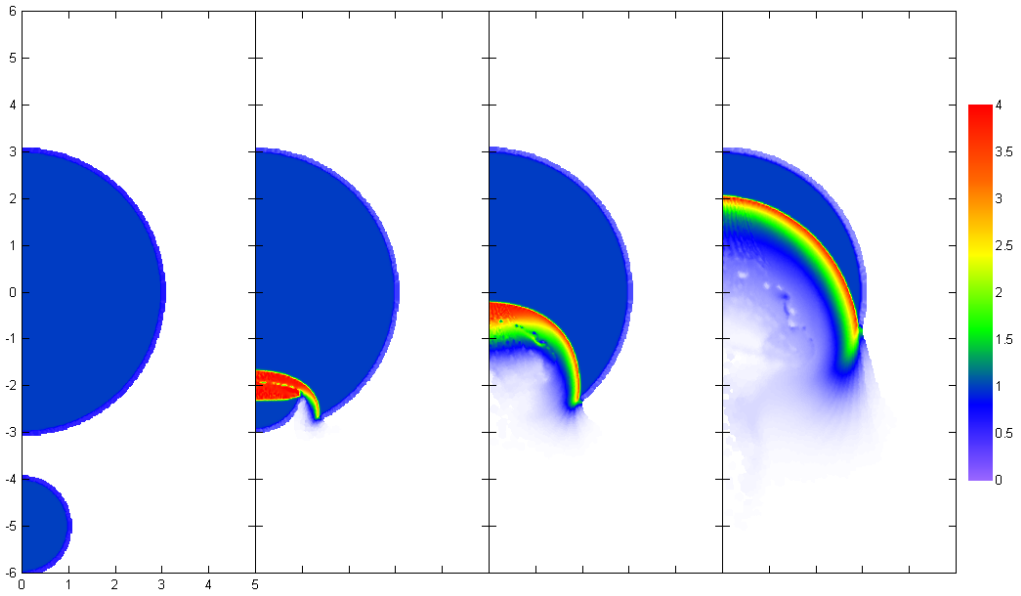

Figure 3.7: Density color map of the collision of two streams of gas at times $t = 0, 0.31, 0.69$ *and* 1.41 s. Axis units are in cm.

its kinetic energy is deposited as internal energy around the collision region. A shock wave is launched into the larger bubble.

(2) Between $0.5 \leq t \leq 1$ s, the total internal energy does no change so much. At $t = 1$ s, the velocity of the center of mass of both structures was practically the same.

(3) For $t > 1$ s, the energy stored as internal energy is again restored to the system. At larger times, the velocity of the smaller bubble became negative while the bigger cloud acquired a positive velocity to preserve total momentum.

Although the entire phenomenon produces big changes in the velocities of the spheres the velocity of the center of mass of the whole system remains practically unaltered, as it can be seen in Fig. 3.8. The last calculated model shows acceptable values of conservation of momentum and energy. The level of conservation of these magnitudes is, however, worse than in the previous tests. At the final time, $t = 1.4s$, the deviation of the z-coordinate of center of mass position with respect to the value expected from $\bar{v}_z^0 t$ was $\simeq 10^{-3}$ (see Tab. 3.1), while conservation of the radial component was several orders of magnitude better.

In order to understand the origin of the discrepancy relative to momentum con-

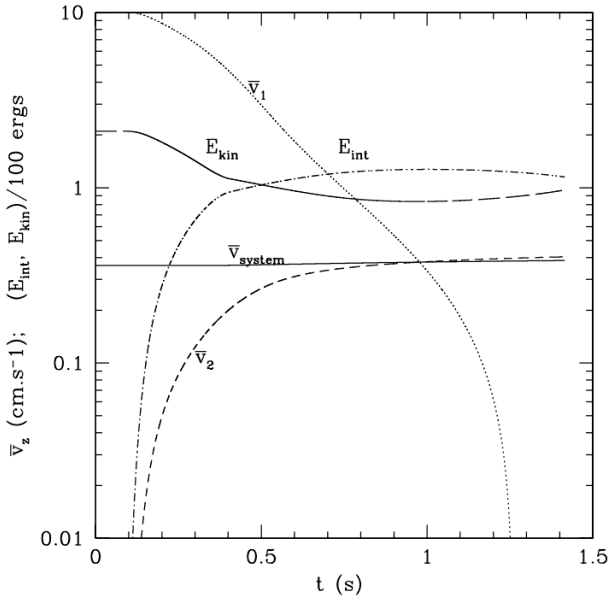

Figure 3.8: Evolution of total kinetic energy E_{kin} and internal energy E_{int} of two homogeneous spherical clouds of gas of different size and mass in a supersonic collision. It is also plotted the evolution of the z component of the velocity of the center of mass of the system, $\bar{v}_{system}$, of the smaller cloud, $\bar{v}_1$, and of the larger one, $\bar{v}_2$.

servation in the z-direction, we can analyze in detail the symmetry of the momentum equation Eq. 3.3. Near (but not at) the z-axis the correction factor f_1 in Eq. 3.6 is not zero. Therefore the z-component of momentum is not symmetric by exchanging particles i and j. On the other hand total momentum is exactly preserved in the radial direction because of the imposed reflective particles across the z-axis. One may thing that a possible cure is to symmetryze Eq. 3.3 multiplying the term $P_j r_j/\widehat{\eta}_j^2$ by f_1^j,

$$\ddot{z}_i = -2\pi \sum_{j=1}^{N} m_j \left(\frac{P_i r_i}{\widehat{\eta}_i^{\,2}} \times f_1^i(\zeta_i) + \frac{P_j r_j}{\widehat{\eta}_j^{\,2}} \times f_1^j(\zeta_j) \right) \frac{\partial W_{ij}}{\partial z_i} \,. \tag{3.15}$$

There was no significant changes. We then conclude that strict total momentum conservation in the z-direction is not possible because of the interaction between real and reflected particles. Such interaction takes place in a small band around the symmetry axis, acting as an external force which modifies momentum of real particles. However, that force cannot be balanced by an opposite force acting in

the left semiplane because, in the z-direction, reflected particles are obliged to move exactly as real particles do. Therefore, if strong directional anisotropies appear in the vertical displacements of the mass points we can not expect a perfect momentum conservation. Eventually, momentum conservation should improve as the number of particles increase because the amount of mass localized in the axis neighborhoods is lower.

Chapter 4

Applications

In the previous chapter we have presented several basic tests aimed at checking the general validity of *AxisSPH* and to be sure that the several routines representing pieces of physics were properly working. Now time is ripe to check the robustness of the code in more real and complex situations which demands also the implementation of a more sophisticated physics. We have chosen three different scenarios of undoubtable interest in many areas of physics, astrophysics and engineering:

(1) The growth of hydrodynamic instabilities during the final phase of the compression of a microcapsule subjected to ICF.

(2) The formation of jets arising from the collision of two streams of gas. Jets born after the impact of metallic plates were also considered in this section.

(3) The numerical simulation of the collision of two white dwarfs, as a possible scenario to explain the origin of type Ia supernova explosions.

4.1 Simulating the stagnation phase of ICF capsules

One of the most important difficulties to achieve a good compression of the pellet in standard confinement fusion is the existence of hydrodynamic instabilities during different stages of the process. The growth of several kinds of instabilities:

Rayleigh-Taylor (RT), Kelvin-Helmholtz (KH) or Ritchmyer-Meskov (RM) leads to the degradation of the spherical symmetry and, therefore, to the viability of an efficient ignition.

We have focussed our attention on the simulation of the final stages of the ICF implosion, where the growth of the RT instability has been recognized as one of the biggest difficulties to achieve a healthy ignition ([3],[34],[50]). Given the multidimensional nature of hydrodynamic instabilities the one-dimensional simulations only provide a qualitative description of these phenomena. Therefore, to understand the details of the ICF process it is obliged to carry out the simulations in more than one dimension. Nowadays all hydrocodes devised to study ICF are grid based codes, some of of them including a rather complete physics (for an extensive report of different ICF codes see [58]). In particular two-dimensional axisymmetric codes have been around since 1990, (for example the ILESTA-2D [79] and MULTI-2D [62] codes). Efficient 3D-codes have been developed roughly since 2000 (for example [39] and [65]).

Despite the success of SPH to study stellar explosions ([22] on type Ia SN, [19], [20], [17] on SNII) there have been very few attempts to adapt the SPH technique to conduct studies of ICF ([66], [67]). As it has been remarked SPH is a fully lagrangian method, free of numerical diffusion, which avoids the problems associated to mesh tangling an distortion due to its gridless nature. Therefore SPH is especially suited to handle dynamical processes involving large deformations of the bodies and the quick changes of scale associated to implosions/explosions. It also avoids to waste a large number of mesh points to cover very diluted regions, such as those found during the evolution of ICF targets.

4.1.1 Physics of ICF

In the standard inertial confinement fusion scheme the nuclear fusion of deuterium and tritium of a small pellet can be achieved [3] when, in a short lapse of time ($\sim 10^{-10}\ s$), very high densities are achieved ($\sim 10^{26}\ particles\ cm^{-3}$) during the final steps of the implosion.

The high compression is produced by the shockwave launched into the inner material of the capsule. The strong shockwave moves inward to conserve momentum,

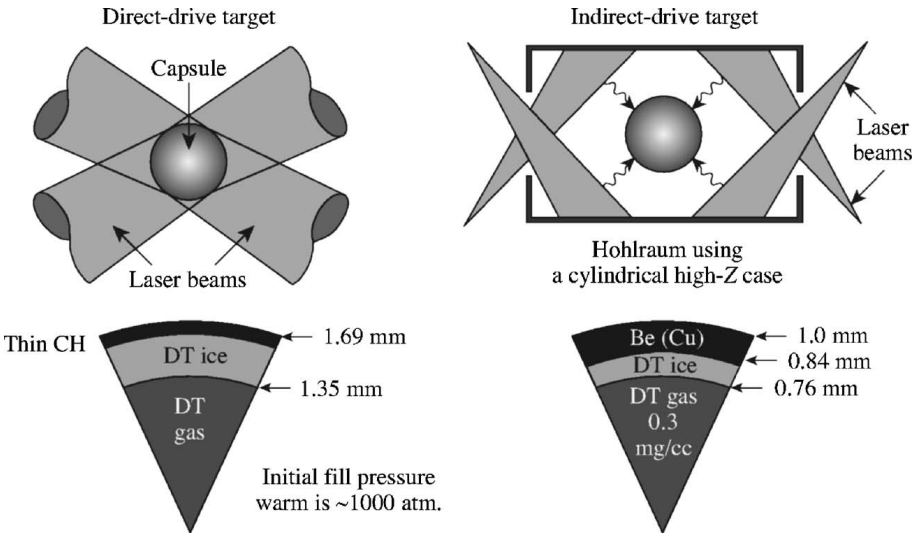

Figure 4.1: Sketch of the drive concept and capsule design for both direct- and indirect-drive ignition targets. [Source: [73]].

as a reaction to the ablation of the outer part of the capsule.

There are different mechanisms and drivers to inject the energy required to ablate the surface of the capsule (intense laser or beams of ions, see Fig. 4.1). In the direct drive implosion the capsule is directly irradiated while in the indirect-drive implosion the driver energy is first converted to soft x-rays and absorbed on the surface of the fuel to generate ablation pressure.

The configuration and design of the capsule depends on the direct or indirect scheme and to the particular driver used to deliver the energy, but it is basically a spherical shell filled with a deuterium-tritium (D-T) equimolar gas. The shell is composed by solid D-T (the main fuel layer or the pusher) and coated by the capsule ablator (examples can be seen in Fig. 4.1).

Different ignition schemes have been proposed to achieve high gain implosions. In the conventional or standard approach the fuel achieves an isobaric configuration after the initial adiabatic compression. Such isobaric configuration is basically made of two regions: a central hot spot or spark region at low density surrounded by a cold dense main fuel region (see Fig 4.2). Once this configuration is achieved the fusion begins in the spark region and the α-particles produced in the fusion of the deuterium and tritium carry its energy to the main fuel producing a nuclear detonation wave that burns the remaining of the shell. This configuration is possible with a tailored

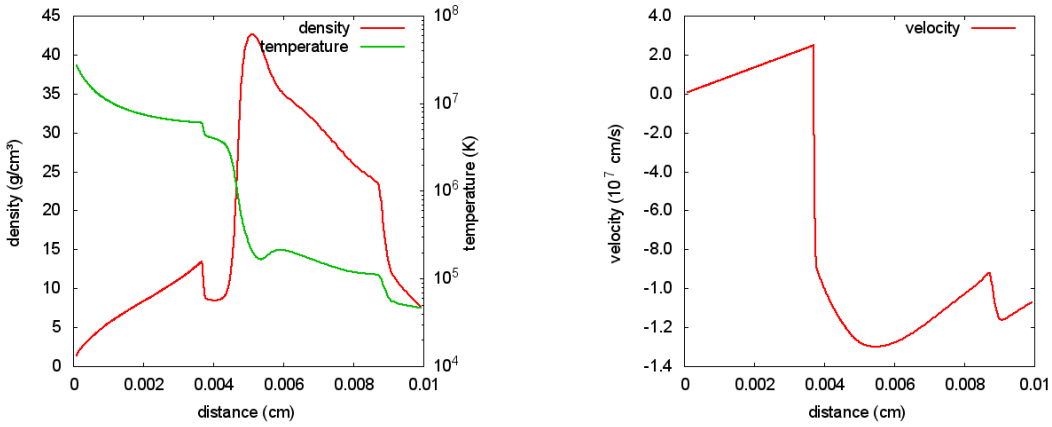

Figure 4.2: Initial profiles of the velocity and the density at the beginning of the stagnation phase obtained with a one-dimensional hydrocode.

deposition of energy which keeps the increase of entropy as low as possible.

In the 90's, an new ignition scheme was proposed [78] called the *fast ignition*, in which once a central compressed region forms, a fast heating ultra intense pulse is injected to produce the ignition, this time in a off-center hot spark. For this mechanism to work the pulse length must be shorter than the expansion time of the compressed region ($t < 10^{-11}\ s$). One of the most remarkable advantages of this approach is that the compression and the fast heating can be performed separately.

4.1.2 Hydrodynamic instabilities

The Rayleigh-Taylor (RT) and Kelvin-Helholtz (KH) hydrodynamic instabilities [12] can appear in two critical moments during the ICF process. The first one during the ablation of the surface of the pellet and the second during the stagnation phase when the shell is decelerated by the hot spot.

As it is well known the RT instabilities grow when a denser fluid with density ρ_2 is accelerated by a lighter fluid with density ρ_1, $\rho_1 < \rho_2$, that is when the pressure and density gradients satisfy $\nabla P \cdot \nabla \rho < 0$. In these conditions a small perturbation δ_0 at the interface will grow exponentially, $\delta = \delta_0 \exp(\gamma t)$ with a *classical* growth rate [12]

$$\gamma = \sqrt{A_t k g}\,, \tag{4.1}$$

where $A_t = (\rho_2 - \rho_1)/(\rho_2 + \rho_1)$ is the Atwood number, k is the wave number of the perturbation and g is the acceleration of the interface.

At the beginning the RT instabilities are produced in the ablation front where the implosion of the denser and cold shell is accelerated inwards by the hot and low-density plasma produced by the laser beam or by the x-ray irradiation. The small initial irregularities of the target finish and the non-uniformity of the deposition of energy can break the spherical symmetry inducing the grow of the RT instabilities.

Afterwards the shell reaches its maximum velocity and the acceleration becomes zero. During this in-flight stage, the capsule is not unstable but, later on, when the shock produced by the ablative implosion is reflected at the center of the target and the stagnation phase begins there is a second chance for hydrodynamic instabilities. The hot spot decelerates the incoming denser shell, so the fuel-pusher interface is again subjected to the RT instabilities. The amplification of small irregularities in the denser shell can lead to its break up reducing the viability of the ignition.

Several experimental and numerical simulations (see for example [72] and [2]) have shown that the classical growth rate (Eq. 4.1) has to be modified at the ablation front, because it neglects corrections due to density gradients, thermal conduction and ablation. Several different expressions have been proposed, but one of the most used is

$$\gamma = \alpha\sqrt{\frac{gk}{1 + kL_m}} - \beta k v_a\,, \tag{4.2}$$

which is known as the modified Takabe expression. L_m is the minimum of the density scale-length L at the ablation front ($L = \rho/\nabla\rho$), v_a is the ablation velocity and α and β are numerical parameters ($\alpha \simeq 0.9; \beta \simeq 1 - 4$) fitting experiments. Notice that an increase of v_a or L_m produce a reduction effect of RT growth rate γ. Some authors ([75],[35]) have shown that Eq. 4.2 can also be applied during the stagnation phase. In this stage, the dense and cold material of the shell is ablated by the energy flux carried by electron conduction and by diffusion of α-particles generated in the hot spot, producing beneficial reduction of the linear growth rate.

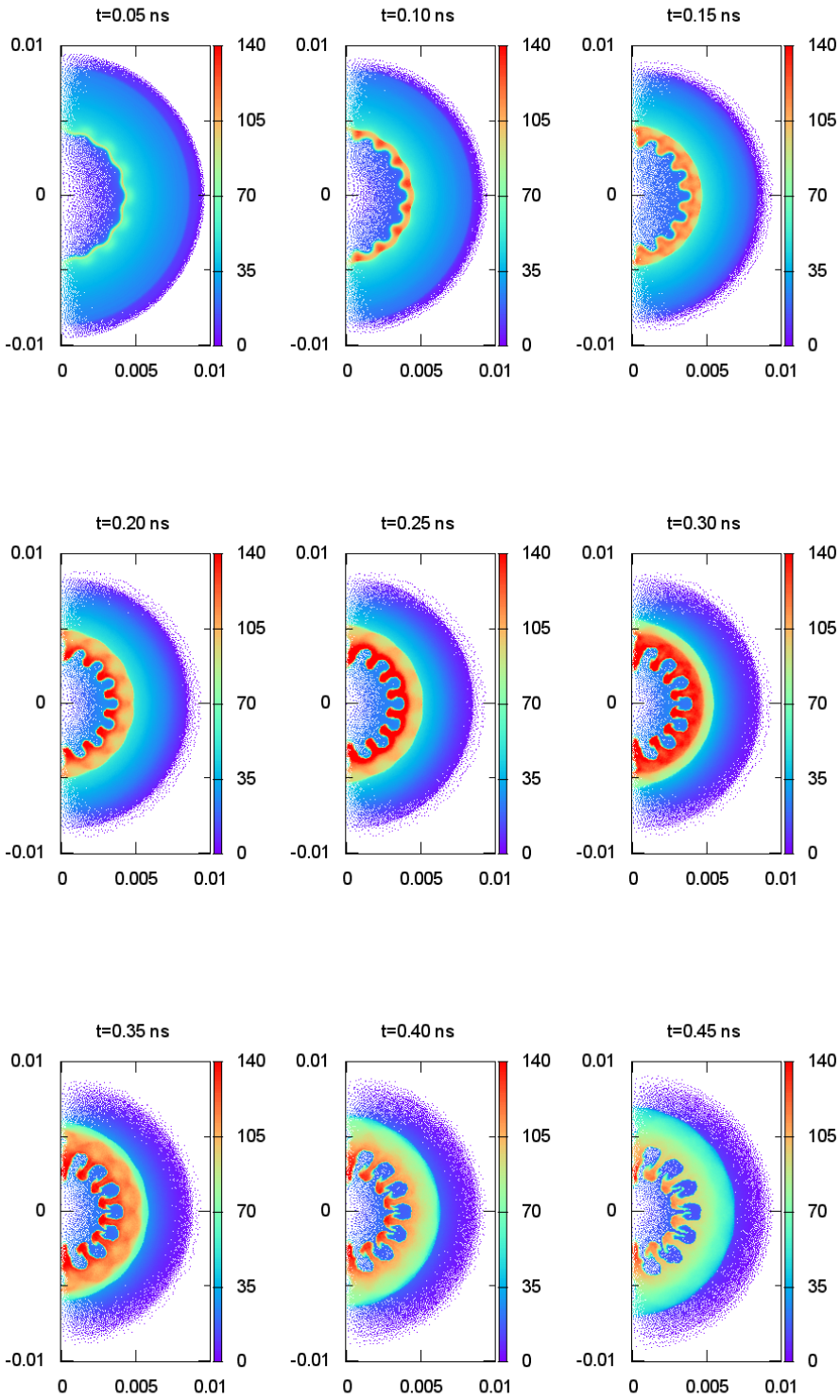

Figure 4.3: Hydrodynamical evolution during the stagnation phase for the mode perturbation $m = 16$. Color represents density in g/cm^3.

Once the amplitude of the perturbation, δ, grows enough to become similar to the wavelength λ of a single mode perturbation ($\delta \sim \lambda$) the instability enters in the non-linear regime characterized by the rising of light bubbles and falling spikes of dense matter. During this stage the amplitude of the perturbation grows in time following a free-falling law $\delta \propto \eta g t^2$ where η is the free-falling coefficient which remains almost constant.

During this non-linear phase the KH instability can also appear driven by the shear flow between the asymmetric large-bubble and thin-spike evolution. The pressure gradient is due to the shock wave front while the density gradient is normal to the contact surface, with different directions. The effect of this instability is the apparition of the roll-up of the spike tips.

The complete evolution of a single mode perturbation can be approximated as [70]

$$\delta = \begin{cases} \delta_0 \exp(\gamma t) & \text{if } \delta < \lambda/2 \\ \delta_1 + \eta g (t - t_1)^2 & \text{if } \delta > \lambda/2 \end{cases}, \tag{4.3}$$

where the subindex 1 of δ_1 and t_1 are the values of δ and t when $\delta \simeq \lambda/2$. Nevertheless, in real devices instabilities are not generated as a single mode and many modes can grow simultaneously increasing the possibility of generate turbulence. The modelization of the whole sample of unstable modes with different amplitudes is beyond the scope of this work but could be an interesting objective in the future.

4.1.3 The stagnation phase using 2D axisymmetric SPH

In this subsection we present the study of the development of the RT hydrodynamic instability during the stagnation stage of the implosion of an ICF implosion using the *AxisSPH* code.

The results of our simulations are compared with those carried out by other authors who made use of different hydrocodes (Sakagami and Nishihara use a 2D fully Eulerian Code, [70]) or 3D codes ([83],[71]).

The initial conditions of our simulations are similar to those used by Sakagami

	$Radius(cm)$	$Density(g/cm^3)$	$Pressure(Mbar)$	$Velocity(cm/s)$
$Fuel$	< 0.013	0.5	10	0
$Pusher$	$0.013 - 0.19$	5.0	10	$1.5 \cdot 10^7$
$Ablator$	> 0.19	0.5	10	$1.5 \cdot 10^7$

Table 4.1: Initial conditions for the 1D simulation.

and Nishihara ([70], or [83]), that is, the fuel is at rest and the pusher and the ablator have the same constant velocity (see Tab. 4.1). We first made use of a one dimensional hydrocode to simulate the conditions of the ICF capsule before the beginning of stagnation.

The one-dimensional profiles (see Fig. 4.2) are used to create a 2D-distribution of 177,120 mass-particles (similar profiles were obtained using the initial conditions of Tab. 4.1 using 2D-SPH code from the beginning). To do this, first we create an angular mesh dividing in sectors the Y-Z plane. Secondly, for each shell, particles are distributed randomly along the intersections following the previous mass profile. Finally the system is relaxed to reduce the unbalanced lateral pressure gradients due to the random distribution (see details in Appendix A).

Different single mode perturbations were seeded at the beginning of each 2D simulation. They were centered at $s_c = 0.0469cm$ (distance to the center of the capsule), the region where the value of $\nabla P \cdot \nabla \rho$ becomes most negative and the Rayleigh-Taylor instability is stronger. At $t = 0\ s$ the 1D velocity profile was perturbed by adding a small perturbation δv to the spherically symmetric radial profile. This is done according to the following recipe

$$v = v_0 + \delta v\,, \tag{4.4}$$

$$\delta v = A \cdot v_0 \cdot \sin(m\theta)\,, \tag{4.5}$$

$$A = A_0 \cdot \exp\left(-\left(\frac{s - s_c}{\varsigma}\right)^2\right)\,, \tag{4.6}$$

where m is the spherical mode number, related with the location of the contact surface through the wave number $k = m/s_c$. A_0, and ς are parameters which control the initial amplitude of the perturbation and the width of the Gaussian

function around the s_c where the perturbation is applied. Similar simulations but seeding the perturbation in the density profile can be found in [67].

The set of conservation equations for mass (Eq. 3.1), momentum (Eq. 3.2 and Eq. 3.3) and total energy (Eq. 3.4) are solved using a two-step centered scheme with second order accuracy. Self-gravity and nuclear reactions are not included in this test. The equation of state includes the contributions of an ideal gas of ions, a partially degenerate electron gas and radiation in thermal equilibrium at a unique temperature T. The one-parameter family of interpolating kernels $W_n^H(v,h)$ are used to run these simulations (see Appendix B for details).

In several tests the electron thermal conduction was included in the energy equation by adding the conduction term Eq. 2.117 where κ_i is the well known form of Spizer-Härm thermal conductivity [76].

In order to test the influence of the artificial viscosity, we have run various simulations using the artificial viscosity (Eq. 3.8); reducing the viscosity parameters α_0 and β_0 of Eq. 3.9 and α_1, and β_1 of Eq. 3.11, and also using the form function f_i (Eq. 2.136) proposed by Balsara [5] which suppress the artificial viscosity wherever strong shear flow is present.

4.1.4 Results of the simulations

We have analyzed the hydrodynamic evolution of the stagnation phase for different modes, m, and with different conditions of viscosity, conduction and initial amplitude, A_0. In Table 4.2, there are summarized the initial conditions, the numerical growth rate γ, obtained using *AxisSPH* and the theoretical value γ_{theor}.

The viscosity parameters are set to $\alpha_0 = \alpha_1 = 1, \beta_0 = \beta_1 = 2$ for those simulations labeled with "*yes*" in the second column of Table 4.2. For the "*Less*" cases the viscosity parameters are reduced to an a half. In all cases $\varsigma = 5 \cdot 10^{-4} cm$ (Eq. 4.6).

An example of the hydrodynamics of a representative simulation is depicted in Fig. 4.3, where all particles are represented at different evolutive times (color represents density in units of g/cm^3). The initial values of the perturbation are $m = 16$, $A_0 = 0.25$, without electronic conduction. In this case the initial amplitude is quite large and the linear regime quickly saturates. In the first snapshot ($t =$

m	Viscosity	Conduct	A_0	$\gamma(ns^{-1})$	$\gamma_{theor}(ns^{-1})$
6	yes	no	0.1	4.74	4.97
8	yes	no	0.1	5.78	5.74
10	yes	no	0.1	5.83	6.42
12	yes	no	0.1	6.51	6.93
14	yes	no	0.1	7.01	7.03
16	yes	no	0.1	7.05	8.12
20	yes	no	0.1	7.14	9.08
20	Less	no	0.1	7.64	9.08
20	Balsara	no	0.1	7.91	9.08
12	yes	no	0.05	6.26	6.93
12	yes	no	0.2	6.61	6.93
6	yes	yes	0.1	4.75	-
12	yes	yes	0.1	6.14	-
20	yes	yes	0.1	6.87	-

Table 4.2: Growth rate numerical results γ and theoretical classical growth rate γ_{theor} calculated with Eq 4.1 under different conditions of viscosity, with or without electronic thermal conduction and with different initial amplitudes of the perturbation.

$0.05\ ns$) is already evident how the effect of the perturbation in the velocity field affects the density and it is clear its sinusoidal nature. For $t > 0.20\ ns$ the asymmetry of the dense spikes and the less dense bubbles is already marked. For $t > 0.35\ ns$ the effect of the Kelvin-Helmholtz instability can be seen on the sides of the bubbles which tangle and roll up into vortices.

We have made quantitative measurements of the development of the RT instabilities in order to make a comparison with the results of other authors ([70],[71],[83], [4]). Because of the large initial perturbation it has been possible to measure the growth rate by measuring the distance, ΔR, between the tip of the bubble and the bottom of their nearest spike. Such distance was taken as the arithmetic mean of the distance between the center of the target and those particles whose density is $1/4, 1/2$ and $3/4$ of the maximum density respectively, as shown in Fig. 4.4 for $m = 14$, $t = 0.15\ ns$. In that figure it is depicted the density profile along the radial direction for both, bubbles and spikes, and also includes a color map of density in the rightmost part of the figure. In the same figure the particles located at the

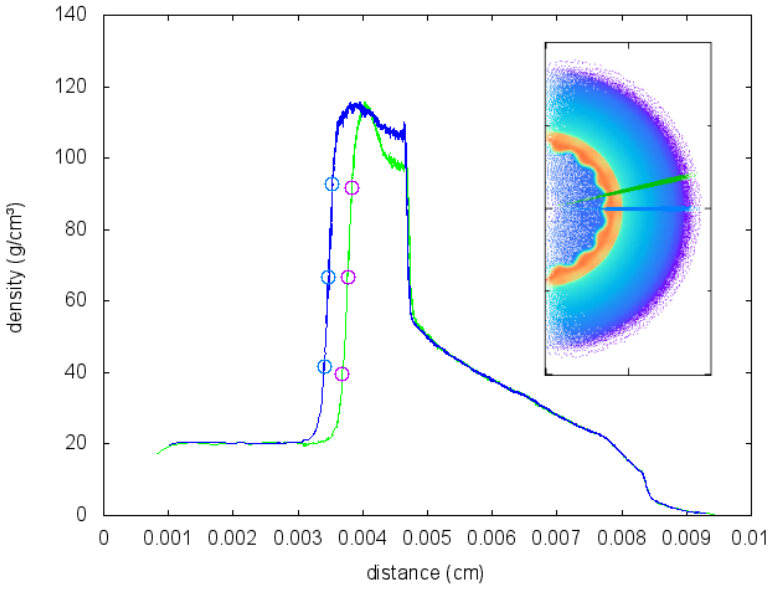

Figure 4.4: Density profiles of particles along the radial direction of a tip (blue) and a bubble (green) for $m = 14$ and $t = 0,15\ ns$. The selected particles are the blue and green particles of the small slide in the rightmost part. The circles mark the position of the nearest particle with densities $\frac{1}{4}$, $\frac{1}{2}$ and $\frac{3}{4}$ of the maximum of each profile.

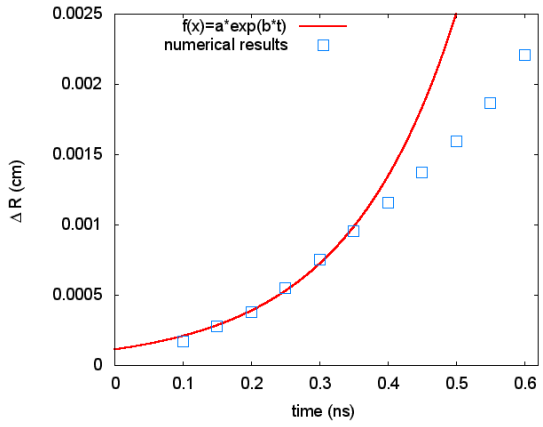

Figure 4.5: Time evolution of ΔR, distance from top of bubble to bottom of spike for mode $m = 12$. Solid line fits the numerical points with an exponential function in the first stage, $t < 0.35\ ns$ of the hydrodynamical evolution when the perturbation grows with the classical linear growth rate.

selected values to measure ΔR are also shown (circles).

An example of the temporal evolution of ΔR for $m = 12$ is shown in Fig. 4.5.

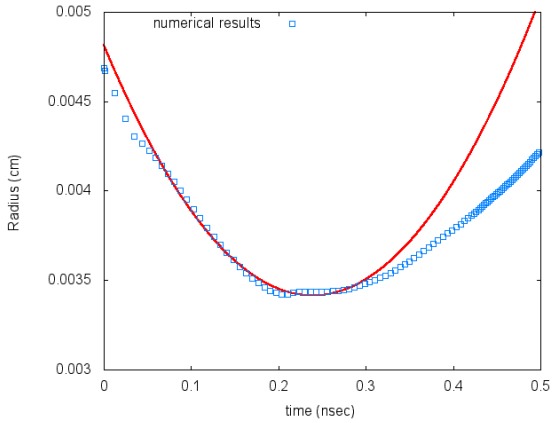

Figure 4.6: Trajectory of the contact surface fitted with a parabolic curve (solid line). The evolution of the contact surface was obtained using a one-dimensional simulation.

As we can see there is an initial stage of exponential growth until $t \sim 0.35\ ns$, that corresponds to the classical growth rate in the linear regime. Fitting the evolution of the numerical results of ΔR using an exponential function leads to the value $\gamma = 6.51\ ns^{-1}$, for the grow rate, (see in Tab. 4.2 for different values of m). This value can be compared with γ_{theor} calculated with Eq 4.1 (because conduction and nuclear reactions are switched off) for the following values $A_t = 0.73$ ($\rho_2 = 160\ g/cm^3$ and $\rho_1 = 25\ g/cm^3$) and $s_c = 0.0034\ cm$ at the moment of maximum compression. The value of the deceleration $g = 0.024\ cm \cdot\ ns^{-2}$, was calculated fitting a parabola with the values of the trajectory of the contact surface (see Fig. 4.6). The theoretical rate was $\gamma_{theor} = 6.93 ns^{-1}$ in reasonable agreement (6 per cent) with the numerical simulation.

In Fig. 4.7 there are represented (diamonds) the numerical values of the growth rate versus time obtained using the *standard* viscosity, without electronic conduction and $A_0 = 0.1$. They compare well with the theoretical curve in red obtained with Eq. 4.1, especially for small values of the mode numbers m (less than 9 per cent for $m \leq 14$) but a larger value for $m = 20$ (20%). This worse values of γ at high modenumbers, could be due to the reduction of resolution and the increase of vorticity. If we increase m we have more mode perturbations with the same total number of particles, which represents a local reduction of resolution. Secondly, the increase on vorticity can produce large amounts of spurious shear viscosity due to the artificial viscosity. Better results have been obtained reducing the artificial viscosity parameters to an a half, and using the functional correction of Balsara (see "*Less Viscosity*" and "*balsara*" in Tab 4.2 and in Fig 4.7 the values represented with

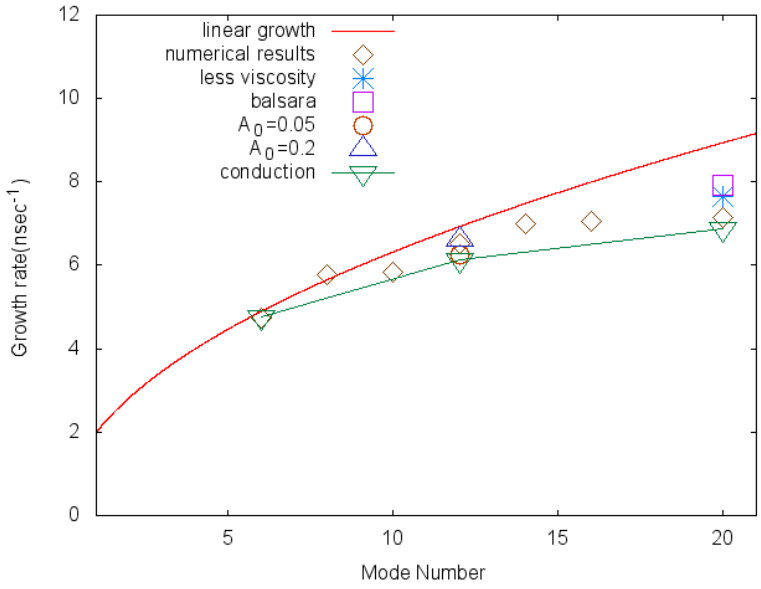

Figure 4.7: Linear dispersion relation (linear growth rate versus mode number m). Different measures are compared: *standard* viscosity, without conduction and $A_0 = 0.1$ (diamonds); with *less* viscosity (asterisk); using the Balsara formula (square); with the *standard* viscosity but changing the initial amplitude to $A_0 = 0.05$ (circles) and $A_0 = 0.2$ (triangles); the electronic conduction is included in the measures represented with inverted triangles and green line. The red solid line represents the Eq. 4.1.

asterisk and square, respectively).

On the other hand we have not seen relevant differences in the growth rate γ for $m = 12$ when the parameter A_0 was changed to an a half or to the double of its original value. The differences were less than 4% and 2% respectively.

Finally we have carried several tests for modes $m = 6, 12, 20$ including the effect of electronic conduction. The effect of the conduction is to reduce the rate of growth. This is in qualitative agreement with Eq 4.2 where the classical growth rate is reduced by the term $\beta k v_a$, as can be seen in Fig 4.7 with inverted triangles and green line.

4.2 Gaseous and metallic jets

As in the case of RT and KH instabilities discussed above the hydrodynamic of jets belongs to a broad family of phenomena which are present in many areas of physics ranging from engineering to astrophysics. Jets play a similar role as laser light does but involving particles (or ions) instead of radiation. Usually a jet is the result of the collimation of an already existing hydrodynamic flow. Under several circumstances such collimation leads to a stable structure consisting of an elonged region possessing a high energy and momentum concentration which moves supersonically. There are many scientific and engineering applications of jets: they are used to cut thick metals, propulse aircrafts or enhance the ability of ICF devices. In astrophysics they are an essential part of the mechanism behind cosmic gamma ray bursts and Herbig Haro objects. Recently jets have become an important part of so called Astrophysics Laboratory where scaling relationships are used to link jets produced in laser and z-pinch facilities to nature [13]. In this chapter we analyze the capability of the proposed axisymmetric SPH to handle jets resulting from the collision of two specular streams of gas along its symmetry plane as well as from two colliding metallic plates. Such kind of jets are very common and they were among the first which were studied either analytically or by using computer simulation means. They have the advantage that a number of analytical relationships can be made assuming a perfect gas EOS, so that they can be used as as test for hydrocodes.

4.2.1 Basic theory of jets

A number of useful relationships can be built assuming several simplificative hypothesis (see [11] and Fig. 4.8):

(1) A conical stream of gas collides incides onto the z-axis with an angle θ so that the process is axisymmetric.

(2) The incident gas obeys a perfect gas EOS law $P = (\gamma - 1)\rho\ u$ being u the specific internal energy of the gas, P the pressure and we take $\gamma = 5/3$ typical of monoatomic gasses.

(3) The refraction of the flux going through the shocked zone is at the origin of

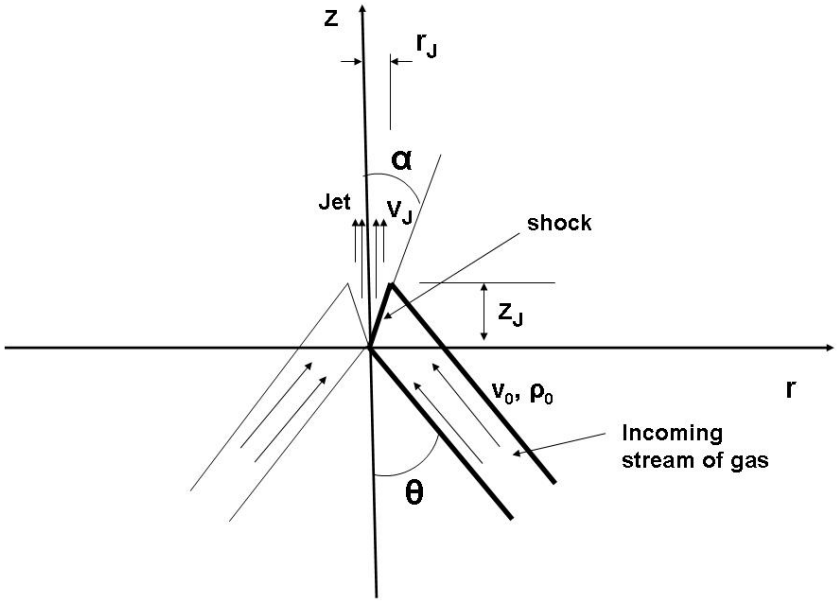

Figure 4.8: Sketch depicting the basic geometrical parameters of a jet.

the jet. The jump of physical variables across the shock front can be described using the classical theory of strong shocks.

According to Fig 4.8, it is easy to show that flux conservation of the gas stream leads to

$$\rho_0' \; v_0 \; \sin(\theta + \alpha) = \rho_J \; v_J \sin\alpha \,, \tag{4.7}$$

where ρ_0' is the density of the gas right before crossing the shock surface. Nevertheless ρ_0' and ρ_J are related by strong shock conditions $\rho_J = c\rho_0'$ where $c = 1/\xi$ is the compression factor, being ξ,

$$\xi = \frac{\gamma - 1}{\gamma + 1} \,, \tag{4.8}$$

which for $\gamma = 5/3$ gives $\xi = 0.25$. Equation 4.7 becomes

$$\xi v_0 \sin(\theta + \alpha) = v_J \sin\alpha \,. \tag{4.9}$$

On the other hand imposing conservation of tangential components of velocity across the shock plane leads to

$$v_0 \ \cos(\theta + \alpha) = v_J \cos\alpha \,. \tag{4.10}$$

Equations (4.9) and (4.10) can be combined to get α, v_J as a function of the usually known magnitudes θ and v_0. For instance

$$\tan\alpha = \frac{(1-\xi) \pm [(1-\xi)^2 - 4\xi \tan^2\theta]^{\frac{1}{2}}}{2\tan\theta} \,. \tag{4.11}$$

It can be shown that only the solution associated with the negative sign is physically correct and is also in agreement with numerical simulations. According to equation (4.11) only those solutions satisfying the the following inequality are possible

$$(1-\xi)^2 \geq \ 4\xi \tan^2\theta \,. \tag{4.12}$$

Depending on the adopted value for θ one or two jets moving in opposite directions could appear. For $\theta < \theta_c$ there is only one jet, the one moving upwards in Fig 4.8. Otherwise a second jet in the opposite direction is also seen (see Fig. 4.9). The value of the critical angle is

$$\tan\theta_c = \frac{1-\xi}{2\xi^{\frac{1}{2}}} = (\gamma^2 - 1)^{-\frac{1}{2}} \,. \tag{4.13}$$

For $\gamma = 5/3$ the the critical angle is $\theta_c = 36.87°$. Therefore reproducing θ_c is an interesting test for any axisymmetric hydrocode.

It is straightforward to find (see [11]) other interesting parameters characterizing the jet, also shown in Fig. 4.8. The uncompressed material of the stream initially placed at position (r_u, z_u) with mass density ρ_0, becomes a shocked material in the jet after crossing the shock front, with coordinates (r_s, z_s) and mass density ρ_J

$$\rho_J = \frac{1}{\xi}\frac{r_u}{r_s}\rho_0 \,, \tag{4.14}$$

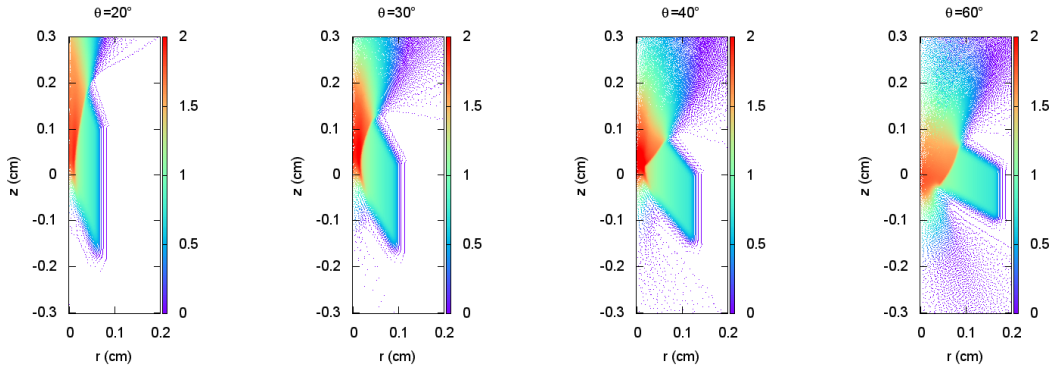

Figure 4.9: Simulations of conical stream of supersonic gas converging onto z-axis for different angles of incidence θ at the same elapsed time. Depending on the collision angle one or two jets (going in different senses along the z-axis) are formed. Color represents density in logarithmic scale.

θ	α_{theor}	α	$(\frac{v_J}{v_0})_{theor}$	$\frac{v_J}{v_0}$	$(\frac{\rho_J}{\rho_0})_{theor}$	$\frac{\rho_J}{\rho_0}$	$r_u(cm)$	$r_s(cm)$	$z_s(cm)$
10°	3.41°	4.14°	0.97	0.98	19.19	18.11	0.086	0.0180	0.249
20°	7.38°	10.76°	0.90	0.88	32.73	31.31	0.171	0.0209	0.110
30°	13.22°	17.69°	0.75	0.73	41.99	41.13	0.251	0.0238	0.075
35°	18.97°	21.76°	0.62	0.55	46.82	45.44	0.287	0.0245	0.061

Table 4.3: Theoretical and measured jet parameters for several angles of incidence $\theta \leq \theta_c$.

that has the contributions of the geometric factor of convergence r_u/r_s and the compression factor across the shock ($\frac{1}{\xi}$ =4 for a monoatomic ideal gas). Notice that the geometric factor can lead to a rather high densities near the z-axis.

The component of the velocity of the jet in the axis direction is

$$v_J = v_0 \frac{\cos(\theta + \alpha)}{cos\alpha} \,. \tag{4.15}$$

Table 4.3 contains the theoretical and measured parameters of the jet, for different angles of incidence lesser than the critical angle $\theta_c = 36.87°$.

4.2.2 Numerical setting and results for ideal gas jets

We have studied the jet formation caused by the convergence of a conical stream of supersonic ideal gas for several angles of incidence θ using *AxisSPH*. To represent the incoming flux of gas we have uniformly spread a sample of $\simeq 8 \cdot 10^4$ particles (the exact number depends on the incidence angle) in a rectangular band of length 1 cm and width 0.1 cm (see the first snapshot in Fig. 4.10 or Fig. 4.13). The mass of the particles was conveniently crafted to get a constant initial density $\rho_0 = 1\ g/cm^3$. The initial specific internal energy of the gas was set to $u_0 = 10^{-4}\ erg/g$ more much lower than the internal energies which will be achieved during the jet formation. Finally a constant initial converging velocity of $v_0 = 1\ cm/s$ (see Fig. 4.8 for the definition of v_0) was given to each particle of the system. The set of SPH equations expressing mass conservation (Eq. 3.1), momentum (Eq. 3.2 and Eq. 3.3) and total energy (Eq. 3.4), with the inclusion of the artificial viscosity (Eq. 3.8), are solved using a two-step centered scheme with second order accuracy.

As in other simulations where strong shocks are present (see for instance Sec. 3.3) the inclusion of an artificial heat conduction term is crucial to improve the quality of the simulations. The effect of including or not such term in the energy equation can be seen in Fig. 4.11 where it is represented a color map of density once the jet is well formed. Both panels in Fig. 4.11 represent the impact of the supersonic conical flow for an angle of incidence $\theta = 30°$. In the leftmost panel the artificial heat conduction was not included leading to the inhomogeneities which are clearly seen in the figure while in the rightmost picture the inclusion of that term manages to erase the inhomogeneities.

In Fig. 4.10 there are shown six snapshots describing the hydrodynamic evolution of the jet at different times (the color intensity denotes the logarithm of the density). As the initially homogeneous cold stream of gas approaches the coordinate origin its density rises due to the geometrical convergence of the flow. Soon the incoming flow collides with the specular stream of gas arriving from the negative part of the r-axis and a localized high pressure zone is born close to the symmetry axis. A steady state is achieved consisting in a high pressure zone with high temperature and density separated from the incoming supersonic flow of gas by a discontinuity. Such discontinuity marks the location of a strong shock wave through which the incoming flow of gas is passing. The nearly steady state has already been achieved in the second snapshot in Fig. 4.10. The cold supersonic ($c_s \simeq 0.05\ cm/s$ and

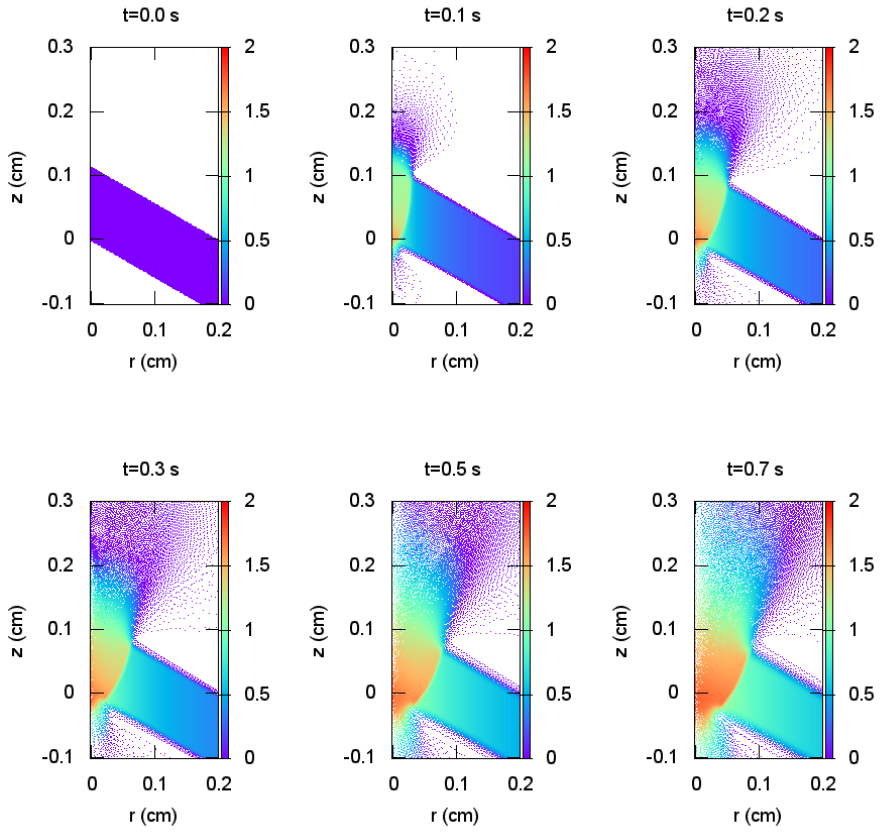

Figure 4.10: Hydrodynamical evolution of the conical stream of supersonic ideal gas for the incidence angle $\theta = 60°$. Color represents density in logarithmic scale.

$v_0 \simeq 1\ cm/s$) impacting gas is practically undisturbed until it crosses the shock front and it is diverted in one or two jets depending on the incidence angle. When the flow goes through the shock front a high pressure bubble forms which rapidly expands along the z-axis giving rise to the jet/s. For angles larger than the critical angle θ_c (as that shown in Fig. 4.10) two jets show up separated by a stagnated zone made of particles with very low velocity, as it can be seen in the fourth panel of Fig. 4.12.

As the angle of incidence decreases there is observed a reduction in the distance from the shock to the z-axis, a reduction in the amount of material in the jet moving towards the $z < 0$ region and also a lesser amount of stagnated particles (see Fig. 4.12). Ideally for incidence angles lesser than θ_c one side of the shock would remain attached to the origin of the z-axis, leading to the total suppression of the

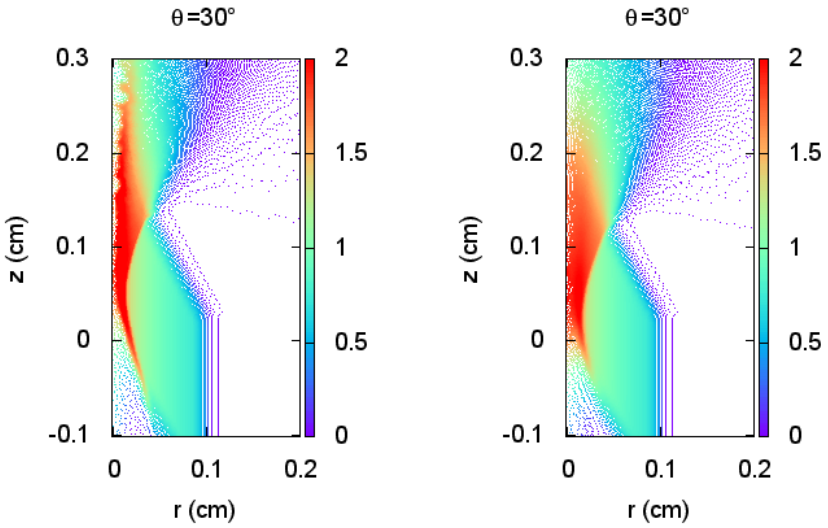

Figure 4.11: Density color map of the late time configuration for an ideal gas jet without (right) and with (left) the inclusion of the artificial heat conduction.

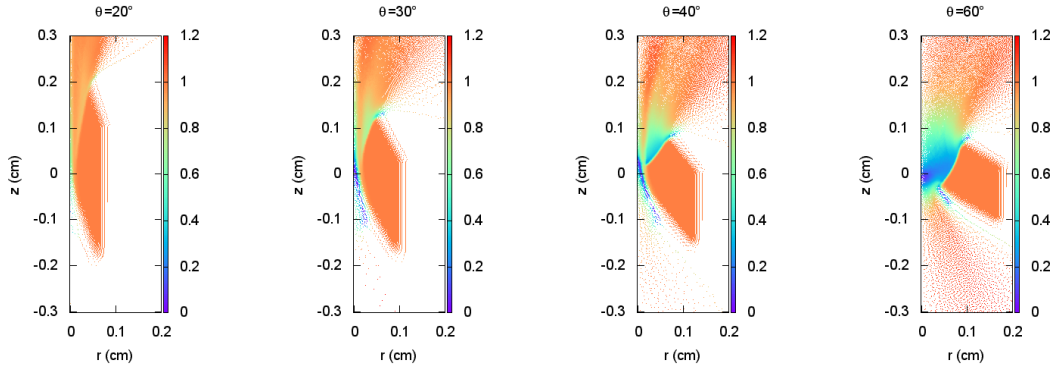

Figure 4.12: Velocity color-map of the same late time configuration for different angles of incidence θ of jets produced by the convergence of ideal supersonic conical gas flows.

jet in the lower quadrant. These cases would correspond to the theoretical model discussed in SubSec. 4.2.1.

It is difficult to get a precise value of the critical angle from the numerical simulations because the suppression of the second jet is not completely abrupt as the angle of incidence of the incident gas decreases. For example, for an incidence angle

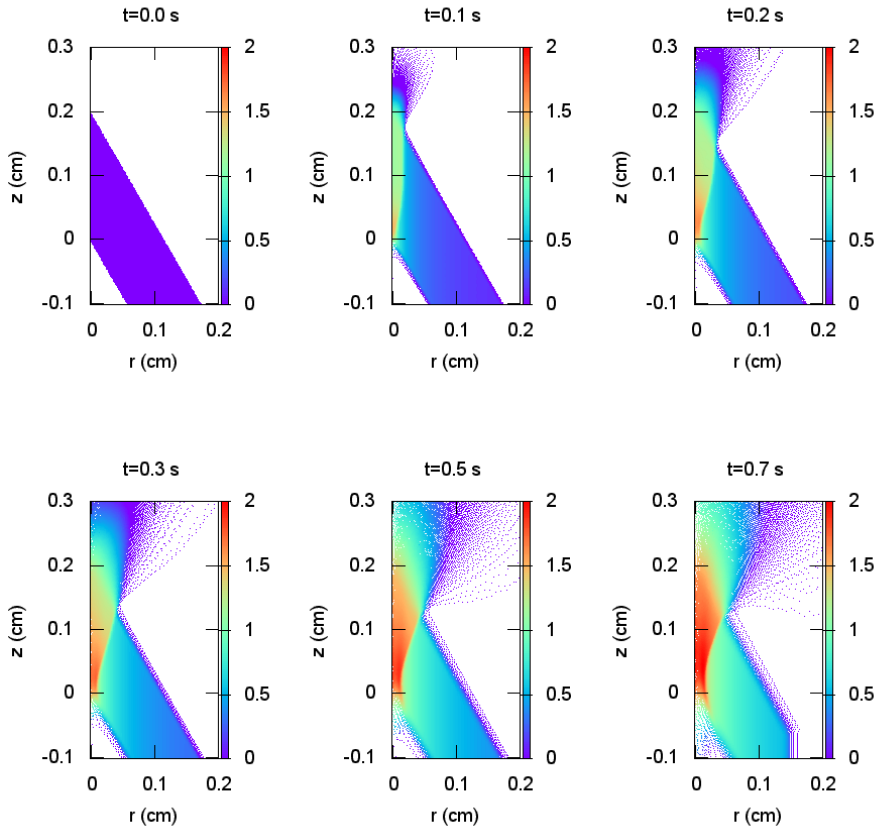

Figure 4.13: Hydrodynamical evolution of the conical stream of supersonic ideal gas for the incidence angle $\theta = 30°$. Color represents density in logarithmic scale.

of $\theta = 30°$, as depicted in Fig.4.13, there still remains a small amount of particles moving with low but negative vertical velocity, v_z. Nevertheless the critical angle obtained from the simulations, $\theta_c \simeq 30°$, is in reasonable agreement with the basic theory of jets exposed above.

Several things must be considered to explain the differences between the simulation and the theoretical model. Firstly, there is a small lateral expansion of the gas stream as it moves towards to the z-axis. Therefore the physical conditions of the gas when it crosses the shock front are not exactly the same as those considered in the analytical model. Secondly, the shock front has not a perfect plane geometry because it has a slight curvature produced by the weakening effects of the lateral rarefaction fans. This effect can be seen clearly in our simulations (see for instance the right panel in Fig. 4.11) and in the simulations made by other authors (as in Fig.

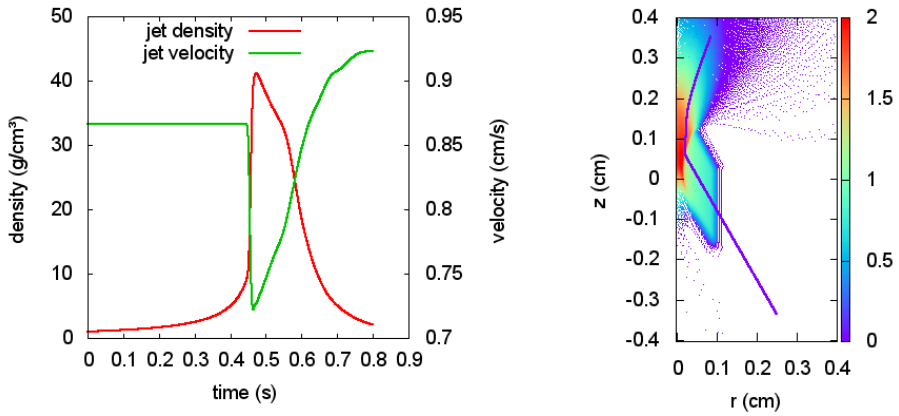

Figure 4.14: Left panel: Evolution of density and z-component of the velocity of a particle initially placed in the center of the jet, with angle of incidence $\theta = 30°$. Right panel: Trajectory of the selected particle (blue line) superposed to the density color-map for $t = 0.8\ s$.

3a in [41]). Under this conditions it become difficult to measure the angle α between the conical shock and the z-axis (see Fig. 4.8).

For each incidence angle θ, we have tracked the trajectory and evolution of the mass density and the velocity of a selected particle from its initial position (placed in the center of the jet through the shock front, see Fig.4.14). In order to measure the jet parameters we have chosen two fiducial points of the trajectory. The first one is in an unshocked position (r_u, z_u) at the center of the initial jet, and the second placed after the shock front (r_s, z_s). The jet parameters were estimated just at the point where the particle gets its maximum density. The measured α values of Table. 4.3 have been calculated as $\alpha = arctan(r_s/z_s)$ and there are sketched by the blue lines in Fig. 4.15. In general, we obtain values for the angle α slightly higher than those predicted by the theory but, given the uncertainties stated above, the agreement is not bad. According to Table. 4.3 the computed velocity and the mass density of the jet is in rather good match to the theory.

4.2.3 Simulation of metallic jets

There are a number of engineering applications where a pair of metallic plates are bring together at supersonic velocity (for example with an explosive charge). Under several circumstances a jet is born at the region of collision. To correctly study

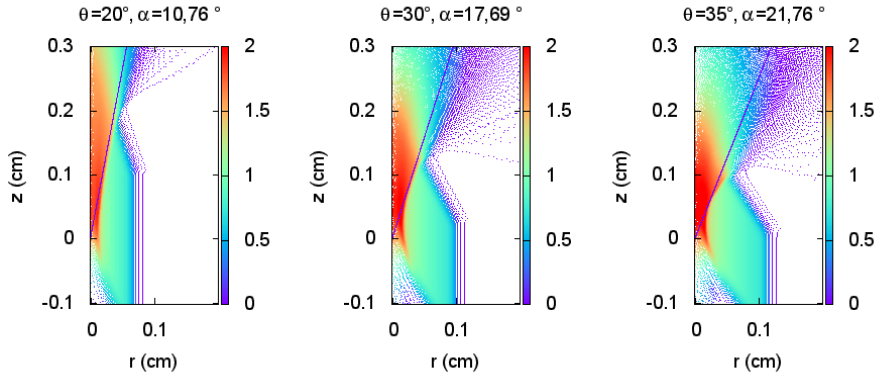

Figure 4.15: Straight blue lines give a estimation of the angle α, between the shock front and the z-axis (see Table 4.3). The lines are superposed to the density color-map for several incidence angles θ.

these jets it is necessary to implement a rather sophisticated EOS. However much insight about the physics involved in the formation of metallic jets can be gained by using simple analytical equations of state. Among them probably the simplest one comes from the use of the so called *stiffened gas*, whose properties resemble those of metals, but whose EOS is still almost as simple as that of an ideal gas. In the stiffened approach the pressure is calculated using the following expression [26]

$$P = (\gamma - 1)\rho u + a^2(\rho - \rho_0)\,, \tag{4.16}$$

where γ and a, are state constants which depend on the type of metallic material considered whereas ρ_0 is the density of the material at normal ambient conditions. The first term in Eq. 4.16 is the ideal gas EOS while the second one contains information concerning the metallic nature of the material. The positive constant a is especially relevant because it is the sound speed of the material at ambient conditions ($\rho = \rho_0$ and $u = 0$). In the limit, as $\rho \to 0$, the pressure approaches a value independent of the internal energy u, $P \to -a^2\rho_0$, meaning that pressure can become negative, as in real metals. Therefore an stiffened gas is able to support tension.

In a isolated system, the specific internal energy u of an stiffened gas can be obtained integrating

$$du = -PdV = \frac{P}{\rho^2} d\rho \,, \tag{4.17}$$

and using Eq. 4.16 to give

$$u = K \left(\frac{\rho}{\rho_0} \right)^{\gamma - 1} - a^2 \left(\frac{1}{\gamma - 1} - \frac{\rho_0}{\gamma \rho} \right) , \tag{4.18}$$

where K is an integration constant depending on the initial conditions. Substituing Eq. 4.18 in Eq. 4.16 gives

$$P = K \rho_0 (\gamma - 1) \left(\frac{\rho}{\rho_0} \right)^{\gamma} - \frac{a^2}{\gamma} \rho_0 \,. \tag{4.19}$$

In the stiffened gas EOS, $P = P(u, \rho)$ so the sound speed must be calculated as

$$c^2 = \left(\frac{\partial P}{\partial \rho} \right)_u + \left(\frac{P}{\rho^2} \right) \left(\frac{\partial P}{\partial u} \right)_\rho , \tag{4.20}$$

using again Eq. 4.16 yields

$$c^2 = \gamma(\gamma - 1)u + a^2 \left(\gamma - (\gamma - 1) \frac{\rho_0}{\rho} \right) , \tag{4.21}$$

finally substituting Eq. 4.18 in the previous expression we obtain another expression for c^2

$$c^2 = K \gamma (\gamma - 1) \left(\frac{\rho}{\rho_0} \right)^{\gamma - 1} . \tag{4.22}$$

Although both equations for c^2 are equivalent it is recommended to use the last expression in hydrocode calculations. The reason is that, according to Eq. 4.21, the sound speed is achieved after a balance of terms that become large and positive and large and negative as $\rho \to 0$. In some cases, these terms may not cancel exactly and produce unphysical negative values of c^2 in numerical calculations. On the other hand Eq. 4.22 does not pose a problem because c^2 is always positive.

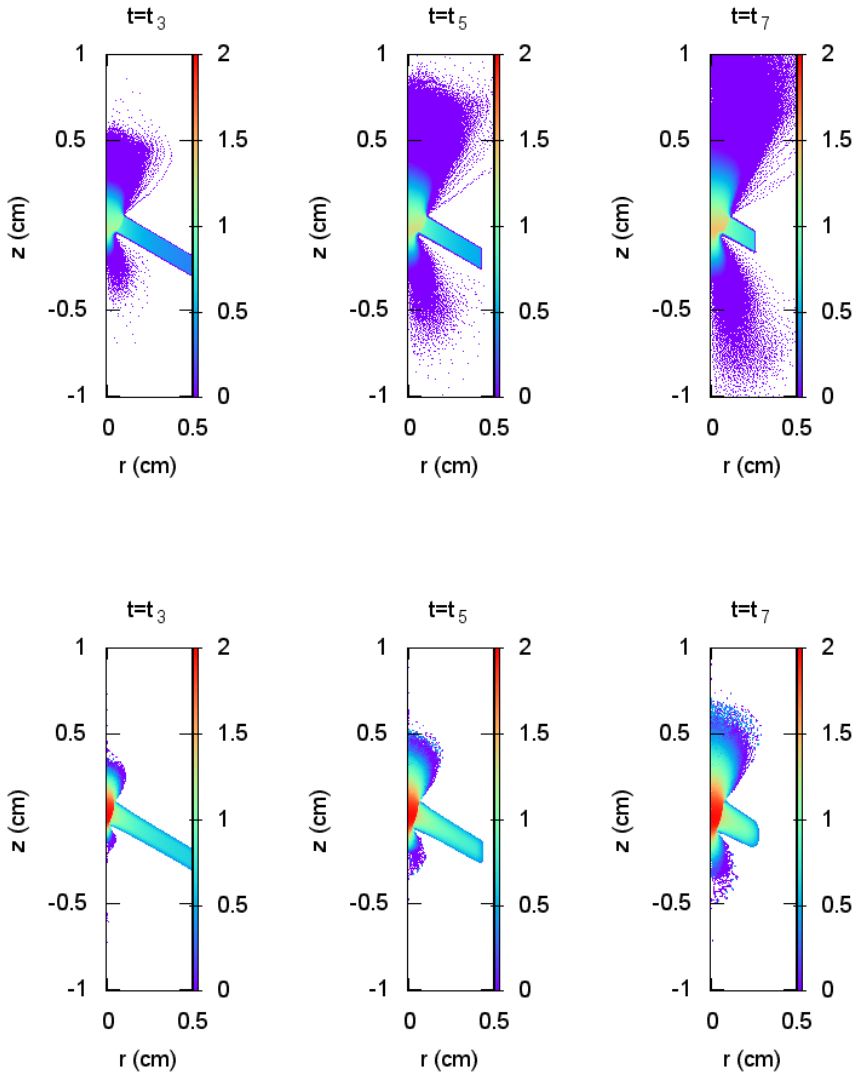

Figure 4.16: Comparison of the hydrodynamical evolution for an ideal gas jet (upper row) and for a stiffened gas (bottom row) at same elapsed times $t_3 = 2.7 \cdot 10^{-8}\ s, t_5 = 4.6 \cdot 10^{-8}\ s, t_7 = 6.4 \cdot 10^{-8}\ s$. Color represents density in logarithmic scale.

In order to qualitatively study the peculiarities of jet formation coming from the supersonic collision of a pair of plates we have implemented the stiffened EOS given by Eq. 4.16 in *AxisSPH*. We have used the following set of parmeters: incidence angle $\theta = 60°$, $\rho_0 = 2.7\ g/cm^3$ (aluminum density), initial impacting velocity $v_0 = 5.5 \cdot 10^6\ cm/s$, initial specific internal energy $u = 8 \cdot 10^6\ erg/g$, $\gamma = 2.5$ and $a = 5.5 \cdot 10^5\ cm/s$. For comparative purposes a model was also run setting $a = 0\ cm/s$

so that the EOS reduces to a pure ideal gas with $\gamma = 2.5$. Both simulations were carried out using the same number of particles $N = 82,530$.

In Fig. 4.16 there is depicted the evolution of density for the ideal gas EOS (upper row) and for the stiffened gas EOS (lower row). Because the angle of incidence is large we see the propagation of two jets moving in opposite directions in each case. The main qualitative difference is in the lateral amplitude of the jets because the jets born from the stiffened gas were much laterally confined than those coming from the ideal EOS. Such behavior is especially marked in the jet pointing to the negative region of the z-axis. That is the correct behavior [26] because as the shocked material expands it reduces its density. Eventually the density becomes lower than the ambient density (i.e. $\rho < \rho_0$) and the stiffened part of Eq. 4.16, $a^2(\rho - \rho_0)$ takes over. The pressure turns to negative values preventing the expansion of the beam which remains much confined than in the case of having an ideal gas with the same adiabatic index γ. Another effect of the stiffened term is the reduction in the speed from non steady flow at the jet tip, as it can also seen in Fig. 4.16, increasing the sharpness in the jet shape. A similar behavior was described in [26]. In consequence metallic jets show much better collimation properties than jets arising from the impact of ideal streams of gas.

Although it could be very interesting to numerically investigate more properties of materials described by an stiffened EOS, for instance the calculation of the critical angle θ_c for different materials or the thickness of the jets as a function of the type of colliding metals, these calculations are out of the scope of this thesis. The main conclusion of this section is that *AxisSPH* can be used to describe the relevant features concerning the jet formation and evolution no matter what EOS is used to describe the nature of the materials.

4.3 Simulating the collision of two white dwarfs using *AxisSPH*

The explosion of a white dwarf star giving rise to a supernova of type Ia is one of the most spectacular and striking phenomenon in the cosmos. Because its extreme brightness it has also acquired particular cosmological significance as a tool to measure the geometry of the universe. These explosions are frequent, occurring at a rate

of about 0.2 per century for elliptical galaxies. However, despite the relevance of these explosions there is not a firmly established model for the progenitor system. In the most commonly studied progenitor of type Ia supernova a massive white dwarf with mass $\simeq 1 - 1.1 M_\odot$ made of carbon an oxygen accretes material from a nearby companion star until the Chandrasekhar-limit mass is reached. Then the white dwarf destabilizes while the temperature at its center becomes high enough to ignite carbon. The nuclear combustion spreads all along of the white dwarf and in a couple of seconds practically the entire star is burnt leading to its total disruption. Other studied scenario involves the coalescence of two CO white dwarfs located in a compact binary system. In this case the mass of the exploding object is the sum of the masses M_1 and M_2 of the two white dwarfs, therefore allowing for a wider variety of explosions from sub-Chandrasekhar $M_1 + M_2 < 1.4 M_\odot$ to super-Chandrasekhar, $M_1 + M_2 > 1.4 M_\odot$.

An interesting variant of the double degenerate scenario has been recently suggested and studied by Rosswog et al. (2009) [69], Raskin et al. (2009 [64] , 2010 [63]) and Loren et al. (2009) [36]. In that proposal the supernova display is produced by the direct encounter of a pair of white dwarfs with mass $0.4 M_\odot \leq M_{wd} \leq 0.9 M_\odot$ in the core of a globular cluster. A rough estimation of the collision rate in a typical globular cluster is $5 - 20 \cdot 10^{-10}$ events per comoving Mpc^3 per year which corresponds to a 10-100 collisions per year in the universe at redshifts $z \leq 1$ [64]. Although the rate is much lower than that of the observed supernova it is not negligible. Therefore the direct collision channel to type Ia supernova merits consideration.

The most complete study of double-degenerate white dwarf collision was carried out by Raskin et al. [63] using a 3D SPH code which typically used $2 \cdot 10^5$ particles (although in one case they did use $2 \cdot 10^6$ particles). In that work different white dwarf masses, $0.5 - 0.81 M_\odot$ and impact parameters (the vertical separation between the cores of both white dwarfs at the moment of impact given as the fraction of the radius of the primary white dwarf), $b = 0, 1$ and 2, were considered. The main conclusion of the study was that for a reasonable choice of the parameters it is not difficult to get $0.3 - 0.8 M_\odot$ of ^{56}Ni, high enough to power the explosion.

Therefore our final and, probably most complete test, to *AxisSPH* is devoted to simulate the head-on impact (i.e. with impact parameter set to $b = 0$) of two twin white dwarfs with $0.7 + 0.7 M_\odot$ and radius $R_{wd} = 8,000\ km$. The same calculation was carried out using an standard 3D-SPH code with exactly the same physics for

comparative purpose.

4.3.1 Astrophysical scenario and numerical setting

The physics included in *AxisSPH* is now much more complex than in the precedent tests. The EOS consists of a mixture of ions, treated as an ideal gas with coulomb corrections, partially degenerate electrons and radiation. Gravity was calculated using the algorithm explained in Subsec. 2.10.2. The energy release due to nuclear combustion was taken into account using an alpha network of 14 species [9]. The nuclear network also includes the binary reactions ^{12}C+^{12}C and ^{16}O+^{16}O. A crucial ingredient of this algorithm devised by Cabezón et al. [9] is that the chemical evolution of nuclear species is calculated implicitly with the temperature evolution. That feature allows to handle all the combustion stages of the mixture from the nuclear statistical equilibrium regime to normal combustion, including the quasi-statistical equilibrium and final freeze out of the species. Networks of similar size but without implicit temperature coupling were used by Rosswog et al. [69] and Loren et al. [36]. Raskin et al. [63] used an hybrid method explicit-implicit to compute the nuclear combustion being, therefore, closer to our implementation. Conductive diffusion was neglected because it remained very small compared to the pdV term in the energy equation.

During the most intense phase of combustion, at densities $\simeq 4 \cdot 10^7\ g/cm^3$ and temperatures $\simeq 6 \cdot 10^9\ K$, the time-step becomes very small $\delta t \leq 10^{-7}\ s$ making the calculation difficult. In these cases the combustion algorithm allows to decouple the nuclear network from the dynamics until the current hydrodynamical time is recovered. Still, it was necessary to run more than a one hundred thousand models to completely follow the event from the stage where the pair of white dwarfs were approaching to the moment where the nuclear combustion becomes negligible after the explosion.

Both white dwarfs have the same mass $0.7 M_\odot$ so that the total mass equals the Chandrasekhar-mass limit. Models in 3D and 2D were built and relaxed to ensure good mechanical equilibrium before collision. The twin stars were then placed with their centres separated by 4 R_{wd} and a velocity $v_z = 1,700\ km/s$ was given to each star (see first snapshot of Fig. 4.17 and Fig. 4.18). The number of particles used in the 3D calculation, $N_{3D} = 200,000$ was similar to that used by Raskin et al.

[63] in many of their simulations. For the axisymmetric simulations we have taken $N_{2D} = 88,560$ particles. Therefore there is factor two of enhancement in resolution, large enough to explore convergence issues of the models.

4.3.2 Description of the collision

As soon as we let both stars free to move their velocity begins to rise and the head on approach starts. The sequence of events is summarized in the series of snapshots depicted in Fig. 4.17. As the stars get close their shape is tidally distorted, as shown in the second image of Fig. 4.17 corresponding to $t = 3.30\ s$. Nevertheless tidal deformation is not strong because of the short time available before the contact. At the third image, $t = 4.66\ s$, the surface of the stars has already come into contact and the collision starts. At that time the relative velocity of the white dwarfs is $v = 4,800\ km/s$, higher than the sound speed at the center of the star, $c_s \simeq 4,000\ km/s$. Therefore we are clearly facing a supersonic event where shock waves will soon or later take over. As a consequence of the brutal impact there is a strong deformation of the white dwarfs along the line joining their centers. As the volume occupied by each white dwarf shrinks the density increases to conserve the total mass. This leads to an increase of the pressure in the central region which provokes the expansion of the plasma along the equatorial plane, giving rise to a ring of material clearly visible in the three last snapshots of Fig. 4.17. When temperature exceeds one billion degrees the binary reaction $^{12}C+^{12}C$ starts along the collision plane and intermediate elements begin to be synthesized at $t \geq 5\ s$ (see Fig. 4.20). The morphology of the merged white dwarfs looks that of a pair of pseudo-semispheres joined by a disc made of burnt material. A detonation propagates through the infalling, still unburnt, material. As carbon and oxygen pass through the shock front, clearly visible in the three lasts snapshots of Fig. 4.17, the fuel compresses, heats and finally ignites. At $t \geq 6\ s$ the combustion is rapid enough to synthesize nuclei of the iron group (see Fig.4.20) and the rate of nuclear energy release jumps to around $10^{52}\ erg/s$. The temperature rises to about 5-6 billion degrees in the shocked zone. In spite of that the burnt region does not expand because of the ram kinetic pressure exerted by the fresh infalling material. Therefore the combustion region remains confined during a time $t \simeq 1\ s$, large enough to allow the synthesis of $\simeq 0.36\ M_\odot$ of ^{56}Ni. At some point the release of nuclear energy in the confined region is large enough to outpower gravity and the kinetic pressure of the infalling matter (two last snapshots in Fig. 4.17). Afterwards the burnt zone expands and

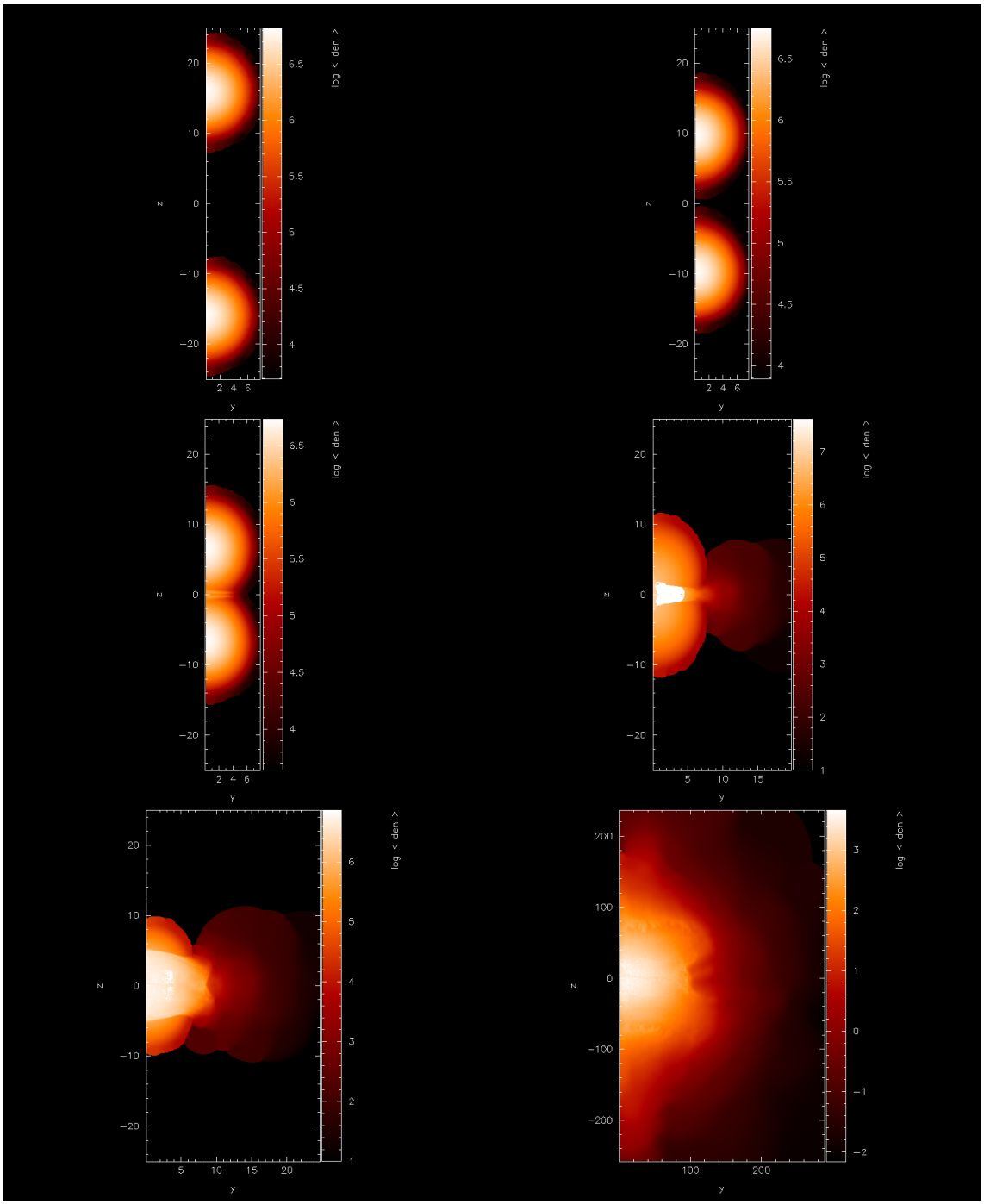

Figure 4.17: Hydrodynamical evolution of the head-on collision of two identical white dwarfs of $0.7\ M_{\odot}$ in 2D. Color represents the logarithm of density, given in g/cm^3 at $t = 0\ s$, $t = 3.30\ s$, $t = 4.66\ s$, $t = 6.27\ s$, $t = 6.80\ s$ and $t = 12.95\ s$ respectively. Axes are scaled to $1,000\ km$. Image obtained using the SPLASH visualization tool [59].

	$3D\ (M_\odot)$	$2D\ (M_\odot)$
α	$1.33 \cdot 10^{-3}$	$3.20 \cdot 10^{-3}$
^{12}C	$5.20 \cdot 10^{-2}$	$5.50 \cdot 10^{-2}$
^{16}0	$1.25 \cdot 10^{-1}$	$1.52 \cdot 10^{-1}$
^{20}Ne	$1.28 \cdot 10^{-4}$	$3.20 \cdot 10^{-5}$
^{24}Mg	$2.45 \cdot 10^{-2}$	$2.86 \cdot 10^{-2}$
^{28}Si	$3.76 \cdot 10^{-1}$	$4.08 \cdot 10^{-1}$
^{32}S	$2.43 \cdot 10^{-1}$	$2.30 \cdot 10^{-1}$
^{36}Ar	$6.94 \cdot 10^{-2}$	$6.10 \cdot 10^{-2}$
^{40}Ca	$9.50 \cdot 10^{-2}$	$8.20 \cdot 10^{-2}$
^{44}Ti	$4.85 \cdot 10^{-4}$	$4.20 \cdot 10^{-4}$
^{48}Cr	$4.34 \cdot 10^{-3}$	$3.80 \cdot 10^{-3}$
^{52}Fe	$2.26 \cdot 10^{-2}$	$1.90 \cdot 10^{-2}$
^{56}Ni	$3.91 \cdot 10^{-1}$	$3.62 \cdot 10^{-1}$
^{60}Zn	$3.48 \cdot 10^{-4}$	$4.02 \cdot 10^{-4}$

Table 4.4: Final abundance of the 14 nuclei for the 3D simulation ($t = 11\ s$) and 2D simulation ($t = 12s$).

cools leading to the rapid freeze-out of nuclear abundances.

The evolution of chemical species is depicted in Fig. 4.20 and a detailed account of the final abundance of the 14 nuclei is given in Tab. 4.4. We see that the heaviest Fe-elements are synthesized in, roughly, a half of a second. We also see that for $t > 6.8\ s$ the abundance of all elements have been frozen by the expansion. The final amount of ^{56}Ni, $\simeq\ 0.4\ M_\odot$ and the total energy of the gas, $E_{tot} \simeq 1.6 \cdot 10^{51}\ erg$ after freezing is plenty compatible with a type Ia supernova event.

4.3.3 Comparison to a 3D-Model

The direct comparison between the above calculation and a full three-dimensional simulation of the same phenomena using the same initial setting and physics will be very valuable because:

(1) It will serve to validate *AxisSPH*.

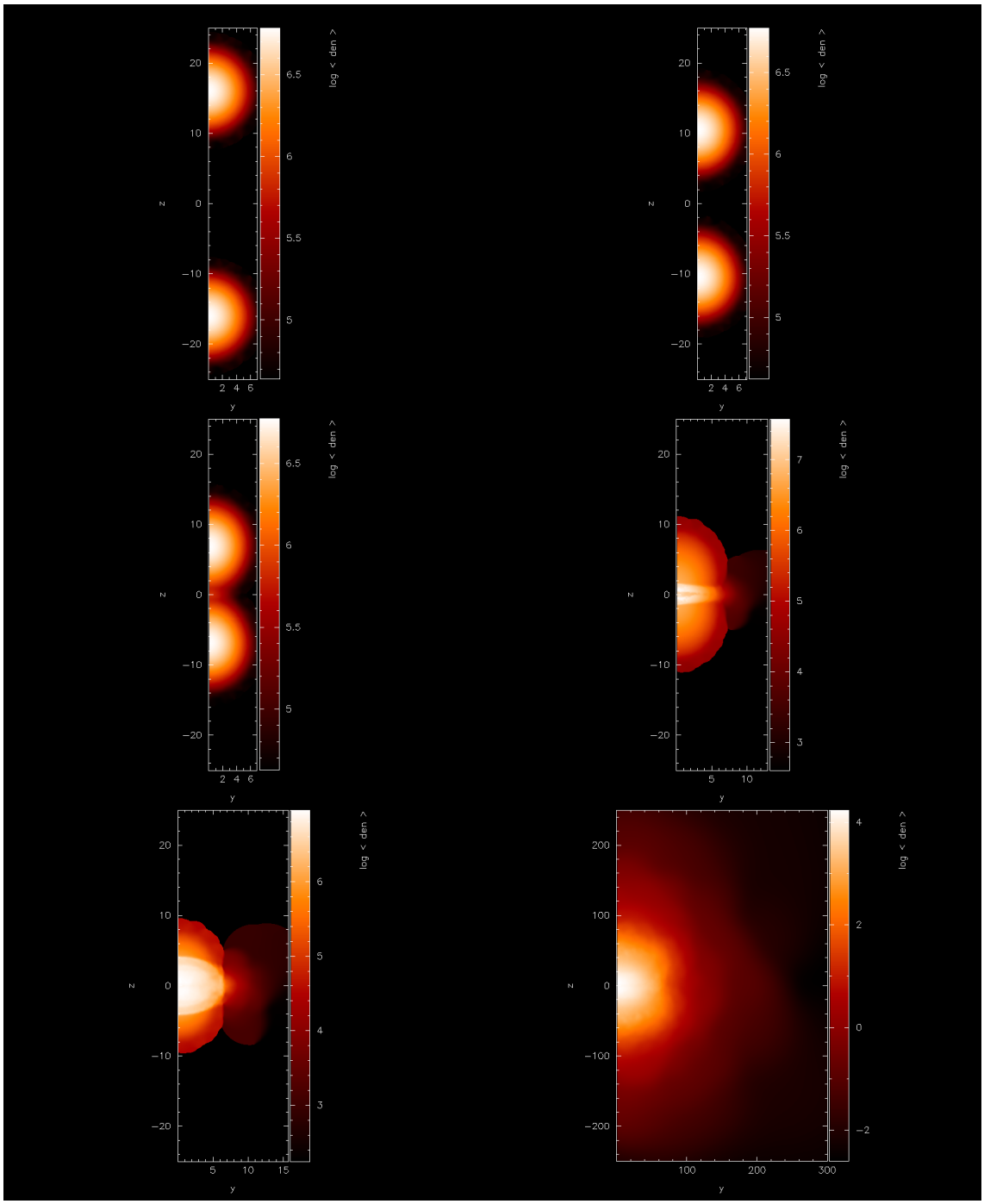

Figure 4.18: Hydrodynamical evolution of the head-on collision of two identical white dwarfs of $0.7\ M_{\odot}$ in 3D. For comparison with Fig. 4.17 it is represented a section in plane YZ with $y > 0$ (axes are scaled to $1,000\ km$). Color represents the logarithm of density in g/cm^3 at $t = 0\ s$, $t = 2.96\ s$, $t = 4.50\ s$, $t = 6.31\ s$, $t = 6.74\ s$ and $t = 10.7\ s$. Image obtained using the SPLASH visualization tool [59].

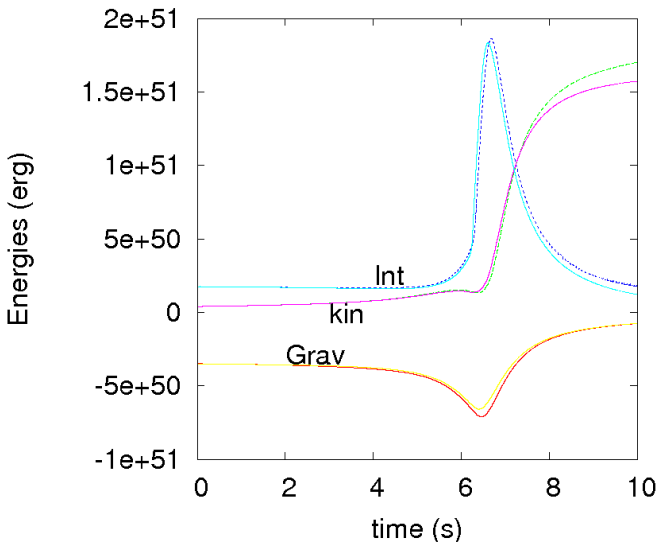

Figure 4.19: Evolution of total internal energy (*Int*), kinetic energy (*kin*) and gravitational energy (*Grav*) for the *AxisSPH* (with dotted lines) and 3D-SPH (with solid lines) simulations.

(2) It will also be useful as a convergence study for the 3D model.

For the 3D setting of the problem we have used $N = 200,000$ particles with equal mass and $N = 88,560$ particles with equal mass for the 2D calculation. There is, therefore, a factor $\simeq 5$ of enhancement in resolution.

The evolution of the 3D model is summarized in Fig. 4.18, depicting the color map of density at different times. The evolution of various energies and chemical species are shown in Fig. 4.19 and Fig. 4.20 respectively. Quantitative data of the abundances of the 14 nuclei considered in our nuclear network is given in Tab. 4.4. Despite the different code conception and resolution the outcome of the simulations in 2D and 3D are strikingly similar. Very minor differences can be seen in the evolution of abundances shown in Fig. 4.20. Production of intermediate-mass elements (IME, from ^{20}Ne to ^{40}Ca) is a bit delayed in the axisymmetric calculation. This can be due to the lower value of the smoothing length parameter in *AxisSPH* which delays the contact between both stars in about $\delta t \simeq 4h/v_{rel}$ being v_{rel} the relative velocity at the impact moment . A little more elements belonging to the iron group are synthesized in the three-dimensional calculation while the total amount of IME is practically equal in both calculations (see Tab. 4.4, and Fig. 4.20). The energetics of both simulations is consistent with the nucleosynthetic trend: the 3D event dis-

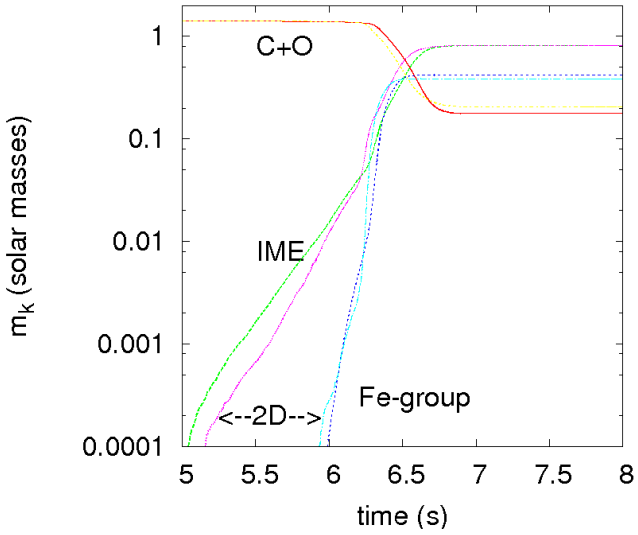

Figure 4.20: Comparison of the abundances (of three isotopes groups: ^{12}C+^{16}0, intermediate-mass elements (IME, from ^{20}Ne to ^{40}Ca) and Fe-group (from ^{44}Ti to ^{60}Zn) evolution for the *AxisSPH* and 3D calculations.

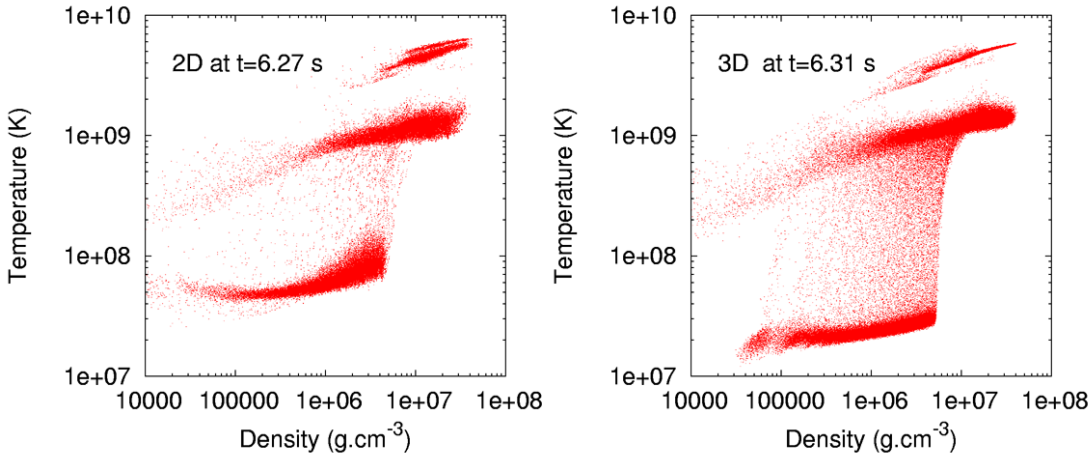

Figure 4.21: Density vs. temperature for all particles of one of the white dwarfs. Left: for the *AxisSPH* simulation when t=6,27 s. Right: for the 3D simulation when t=6,31 s.

plays a slightly larger total energy after the freezing out than that computed with *AxisSPH*. The amount of synthesized ^{56}Ni is 0.39 $M_\odot$ (3D) and 0.36 $M_\odot$ (2D) respectively (Tab. 4.4) but a precise estimation of the final abundance of the elements would need the postprocessing of the model using a much larger nuclear network.

Calculation	Masses ($M_\odot$)	Code	Particles	^{56}Ni ($M_\odot$)
Rosswog et al.(2009)[69]	0.60+0.60	3D-SPH	$2 \cdot 10^6$	0.32
Raskin et al.(2009)[64]	0.60+0.60	3D-SPH	$8 \cdot 10^5$	0.34
Raskin et al.(2010)[63]	0.64+0.64	3D-SPH	$2 \cdot 10^5$	0.51
Raskin et al.(2010)[63]	0.64+0.64	3D-SPH	$2 \cdot 10^6$	0.53
This work (2012)	0.70+0.70	3D-SPH	$2 \cdot 10^5$	0.39
This work (2012)	0.70+0.70	2D-SPH	88,560	0.37
Raskin et al.(2010)[63]	0.81+0.81	3D-SPH	$2 \cdot 10^6$	0.84

Table 4.5: Comparison of simulation ^{56}Ni yields of a head-on white collision for different initial mass combinations and number of SPH particles next to those used in this work.

4.3.4 Comparison to other authors

There are few studies devoted to the WD+WD collision channel to type Ia supernova. Basically those by Rosswog et al. (2009) [69], Raskin et al. (2009) [64], Loren et al. (2009) [36] and Raskin et al. (2010) [63]. With the exception of the paper by Rosswog et al., who simulated only head on collisions, the other ones also included simulations with different impact parameters. The report by Loren et al. especially focussed on orbital aspects of the scenario, from the initial approach of the stars by gravitational focussing to their tidally-induced final collision at several impact parameters. In Tab. 4.5 we summarize the main available information about the head on collision of twin white dwarfs with masses as close as possible to that considered in this thesis (0.7 $M_\odot$).

The most remarkable difference between the models shown in Tab. 4.5 affects the final mass of synthesized ^{56}Ni. For a pair of colliding 0.6 $M_\odot$ white dwarfs Rosswog et al. get around 0.32 $M_\odot$ of ^{56}Ni after postprocessing the hydrodynamic output. A similar amount of ^{56}Ni was reported in Raskin et al. (2009) using an α-network of 13 nuclei. A larger amount of radioactive Nickel, 0.51 $M_\odot$ was, however, found in Raskin et al. (2010), this time with a pair of 0.64 $M_\odot$ white dwarfs. The highest amount of nickel obtained in the latter work is the consequence of the different method of integration of the α-network chain with 13 nuclei used to represent the nuclear combustion [82]. They made use of a semi-implicit integration method called hybrid-burning scheme which, depending on a parameter called f_u, progressively handle reactions implicitly as the photodisintegration regime approaches ([48], [9]).

The abundances shown in Tab.4.4 were calculated using the fully implicit method described in Cabezón et al. (2004) [9] which is more akin to the hybrid-burning method than to standard methods of integration. For the pair $0.7 + 0.7\ M_{\odot}$ white dwarfs we obtain similar amounts of nickel as in Rosswog et al. (2009) and but less than in Raskin (2010), a discrepancy which deserves further investigation. Nevertheless the precise amount of synthesized radioactive ^{56}Ni can only be estimated after postprocessing the output of the hydrodynamic model using a much larger nuclear network.

A convergence study was also carried out in Raskin et al. (2010). They concluded that above $N \simeq 2{\cdot}10^5$ particles there is a convergence in the final amount of ^{56}Ni (see their Figure 11) and other magnitudes. That conclusion is in fair agreement with our own results which were summarized in Figs. 4.19 and 4.20.

Chapter 5

Conclusions

A two-dimensional axisymmetric implementation of the smoothed particle hydrodynamics (SPH) technique, called for short *AxisSPH*, has been described in the precedent pages, along with a number of basic tests and realistic applications. The main goal of this work was to fill a gap on a topic which has been scarcely addressed in the published literature concerning SPH. Although the application of *AxisSPH* to the simulation of real problems is restricted to those systems which display the appropriate symmetry there are, however, many interesting examples of physical systems which evolve following the axisymmetric premise. These examples belong to a variety of scientific and technological areas such as, for example, astrophysics, laboratory astrophysics or inertial confinement fusion. Additionally *AxisSPH* can be also useful in convergence studies of the standard 3D-SPH technique because the higher resolution achieved in 2D can be used to benchmark the three-dimensional codes. To do that it is enough to build an initial 3D configuration related to the problem at hand but with revolution symmetry around an axis. A direct comparison between these three-dimensional and 2D-axisymmetric simulations often sheds light on resolution issues affecting the full 3D calculation.

Old algorithms dealing with axisymmetric SPH were rather crude because they were built simply by taking the mass of the particles $m^{2D} = \frac{m^{3D}}{2\pi r}$ where r is the cylindrical coordinate, [28]. Therefore the hoop-stress effects were neglected and conservation of energy was poor. Petscheck & Libersky [57] and more recently Brookshaw [8] gave a formulation of axisymmetric SPH which incorporated the hoop-stress term expected to appear in the Euler equations in cylindrical coordinates. The hoop-stress force arise from the toroidal nature of particles in axisymmetric codes.

When a particle approaches the symmetry axis it suffers a net outward force derived from the difference of radius between the inward and the outer surface of the torus. Quantitatively the hoop-stress force is proportional to the inverse to the distance to the z-axis (Chapter 2). Such $1/r$ dependence is not rare in cylindrical geometry where there are other magnitudes with the same behavior, especially those related to the divergence operator. Unfortunately the $1/r$ dependence leads to numerical troubles when a particle gets very close to the symmetry axis and $r \to 0$. The problem is difficult and there have been several attempts to handle or, at least to bypass, the problem in axisymmetric SPH. The most simple of them was to keep the system far enough from the z-axis just by constraining the hydrodynamics to take place in a wedge with its apex at the coordinate origin. Using that approach the singularity is reduced from a line to an unique point which can be handled using special conditions [27]. Nevertheless that procedure has the inconvenient that it needs from artificial boundary conditions at both sides of the wedge. A better approach was proposed by Omang, Børve and Trulsen [55] who derive an interpolating kernel that embeds the main features of the cylindrical geometry so that the user works in cartesian coordinates and the modified kernel translates the information to cylindrical coordinates. The formulation of Omang et al. is able to cope with the singularity problem but the price to pay in an increase of in the computational load because an elliptic integral has to be solved numerically for each particle at each time-step.

Given the above difficulties to implement an efficient axisymmetric SPH code which incorporates the hoop-stress terms and, at the same time, is free of singularities we have developed a new scheme based on a formulation which includes all the relevant features of axisymmetric geometry but includes a number of, physically motivated, corrective terms to avoid divergences close to the singularity axis [24]. The main improvements implemented in *AxisSPH* with respect existing axisymmetric SPH formulations are summarized as follows:

- We have derived simple analytical expressions for the correction factors f_1^i (Eq. 2.41) and f_2^i (Eq. 2.96) which largely improves the calculation of density and velocity in the vicinity of the z-axis. These expressions and their derivatives were given as a function of the adimensional parameter $\zeta = r/h$ and do not increase the computational load of the scheme.

- We have obtained the appropriate expression of the fluid Euler equations con-

taining the new correction functions and their derivatives (see Sec.3.1). Far enough from the singular axis, once $r \geq 2h$, the scheme reduces to the standard formulation discussed by Brookshaw [8].

- A novel expression for the heat conduction term (Eq. 2.117), which has to be added to the energy equation Eq. 3.4, was devised and checked. This new term improves the description of the heat flux for those particles located at the axis neighborhoods. It was probed that the new equation leads to the adequate increase of entropy for those systems where conductive (or diffusive) heat transport controls the energy equation.

- Until now axisymmetric SPH hydrocodes handle artificial viscosity using a crude approach because it was treated as a simple restriction of the standard 3D cartesian viscosity to 2D. Here we propose to calculate the viscous pressure as a combination of two terms, $\Pi_{ij}^{2D} = \Pi_{ij}^{(1)} + \Pi_{ij}^{(2)}$, where $\Pi_{ij}^{(1)}$ (Eq. 2.141) and $\Pi_{ij}^{(2)}$ are the (standard) cartesian part and the axis-converging part of the viscosity respectively. As expected the value of $\Pi_{ij}^{(2)}$(Eq. 2.145) is proportional to v_r/r ($v_r > 0$), being of special relevance to simulate implosions.

- We have developed an original method to incorporate gravity into *AxisSPH*. First the direct ring to ring force was found as a function of the Euclidean distance between the 2D particles (Eq. 2.153). In second place the gravitational force on a given particle was obtained by summing the contributions of all particles. Although the ensuing algorithm scales as N^2 instead of the $N\ logN$ behavior typical of hierarchical methods, as for instance the TREESPH [29] the performance is good because: a) a good resolution can be achieved in 2D with less than 10^5 particles, which makes the direct calculation affordable, b) the algorithm can be easily parallelizable, c) it was demonstrated that ring interaction is symmetric so that the real computational load is $N^2/2$, d) the gravity force calculated that way leads to perfect linear and angular momentum conservation.

  A more efficient scheme to obtain the gravitational force can be done if the potential of the ring, instead the force, is calculated because it involves lesser algebraic operations. The force is then evaluated taking the gradient of the potential in the usual SPH manner. Not only the calculation is around two times faster but the potential route has the advantage of being more compatible to the momentum equation because both, gravity and pressure forces are calculated using the nabla operator. However, one inconvenient of using the

potential is that the resulting scheme is not totally conservative but neither it is in the hierarchical tree methods.

- The scheme has been checked using a large number of tests cases. These tests range from very specific, oriented to check a particular algorithm or a piece of physics, to a rather complex ones intended to analyze the behavior of the scheme in potential real applications (ICF, jets, astrophysics). At least in one case, the head on collision of a pair of white dwarfs, the results of the simulations carried out using *AxisSPH* brings new, unpublished, scientific material.

Future work, from immediate to a more distant future, should cover two areas of development: a) The improvement the code, b) Its applications to interesting problems.

Improvements of *AxisSPH*:

- Include the ∇h terms in the equations which have been proved that generally leads to an improvement in the conservation of energy. An expression for these ∇h terms naturally arise from the Lagrangian description of the dynamics [68] and is straightforward to implement.
- It has been mentioned that the calculation of gravity using the gradient of the potential energy is, in its present form (Eq. 2.165), no totally conservative. A future improvement could be to find a symmetric form for ∇V which conserve energy by construction. Probably it would need to work out the axisymmetric SPH from a Lagrangian which include the gravitational potential energy.
- It would be extremely useful for astrophysics to include the transport of angular momentum due to the viscous coupling between particles. This would allow to study many astrophysical problems where rotation can not be neglected (such as differential star rotation or accretion discs).

Applications of *AxisSPH*:

Several applications of the code to astrophysics are going on. For example *AxisSPH* made feasible to calculate the long term evolution, $\Delta t \simeq 1,000\ yr$ of a supernova remnant hosting an axisymmetric void created during the interaction of

the supernova with the secondary star $\simeq$ 1 hour after the explosion [21]. Another potential scenarios are:

- Head on collision of stellar bodies: stars, planets, asteroids etc... In this respect the simulation of the collision of two white dwarfs described in Sec 4.3 is representative of these kind of simulations.
- Advanced states of stellar evolution including rotation: type I and II supernova explosions, gamma-ray bursts, rotating compact objects (white dwarfs, neutron stars, cores of giant stars).
- Laboratory of astrophysics and ICF. There are many terrestrial devices built in axisymmetric geometries which involve very dynamical processes. Among them we can cite the production of jets using Z-pinch devices [33] and the direct and indirect methods to achieve the ignition of deuterium in ICF. However, to properly handle with these kind of problems the hydrocode should include particle and radiative diffusion, many times in the optically thin regime. Therefore this is a difficult task and a challenge for the future.

Appendix A

Appendix: Initial Models

One practical difficulty, of SPH is how to generate suitable initial models mapping from the one-dimensional profile of a physical magnitude to a multidimensional distribution of particles. Some magnitudes as internal energy, temperature or velocity can be easily reproduced just assigning the corresponding value to each particle as a function of its position. Nevertheless, this is not the situation for the density because its value is determined by the contribution of the neighbor particles with different weights as a function of its masses and distances.

In this work we have used different techniques to construct the initial 2D-axisymmetric models. The easiest way to generate an initial model with constant density is to set the particles in a square lattice and give to them a mass proportional to their initial r-coordinate, r_0. Notice that real nature of the 2D interpolation points in the square lattice are 3D rings so taking $dm \propto r_0$ produce

$$\rho = \frac{\eta}{2\pi r_0} \propto \frac{r_0}{2\pi r_0} = cte\,. \tag{A.1}$$

This procedure can be extended to arbitrary spherically symmetric density profiles $\rho_1 = \rho_1(s)$ taking $m \propto r_0 \cdot \rho_1(s)$. Using this technique we have obtained the initial 2D-cylindrical models used in Chap. 3 devoted to validate *AxisSPH*. Nevertheless this technique implies working with particles of variable mass, that in the case of large initial density gradients or under mixing conditions, can lead to large mass contrasts inside the kernel domain. This situation may lead to numerical artefacts in the interpolation of the physical magnitudes. On the other hand, the square

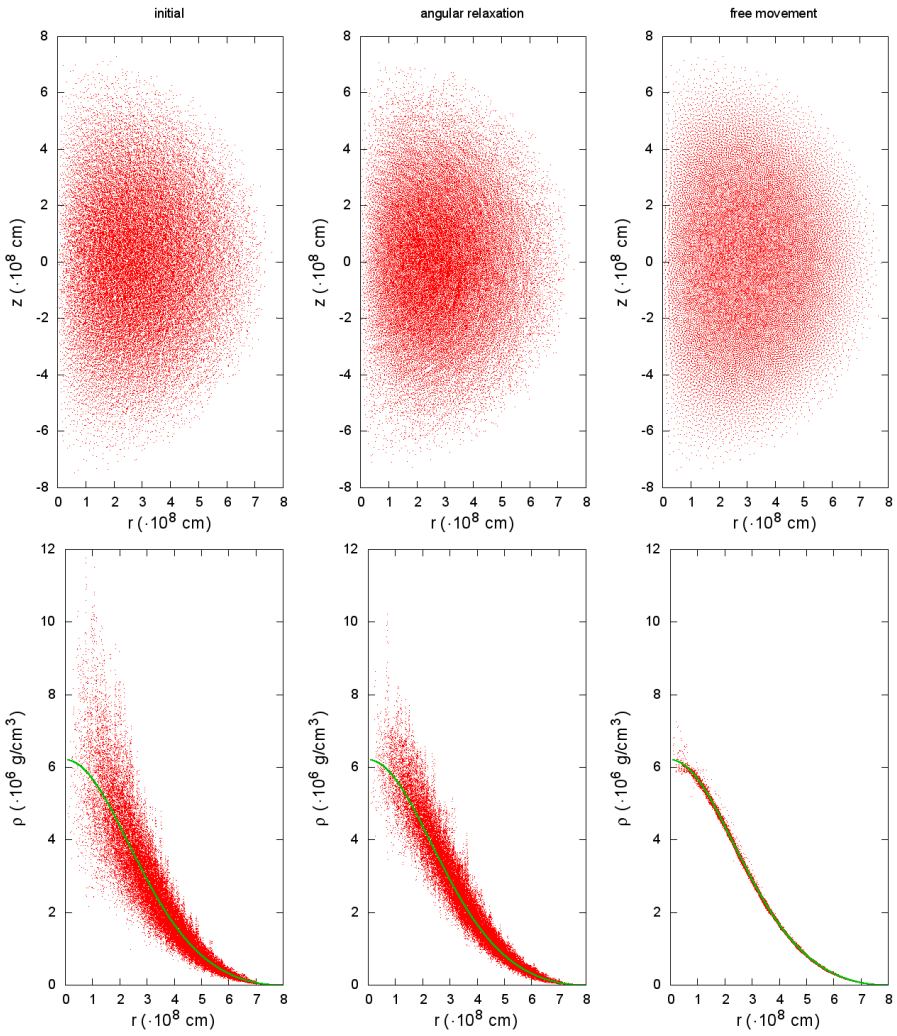

Figure A.1: Spatial distribution (top) and density profile (bottom) of the tree steps procedure to obtain the initial model of one white dwarf used in Sec. 4.3, before (left) and after (center) the angular relaxation process, and after the particles were allowed to move freely (right).

lattice distribution can produce numerical irregularities that arise from preferred directions for the strain propagation. This phenomenon is known as hourglass instability [32]. This undesirable effect can be reduced using an initial mesh with polar symmetry and a random distribution.

In order to minimize these problems it is better to use random distributions of particles with the same mass, dm. Thus, in the simulations of the ICF implosion capsule (Sec. 4.1) and in the head-on collision of two dwarfs (Sec. 4.3) we have built

initial models mapping from spherically symmetric profiles, ρ_{1D}, into a distribution of particles in a plane, that in fact are loops around the z-axis. Notice that we have to be careful with the distribution of particles respect to the zenith angle θ. For example, to construct a sphere of constant density the mass of each particle has to be proportional to the volume element, $dV = s^2 sin\theta ds d\theta d\varphi$, expressed in spherical coordinates, where s is the distance from the origin, $s = \sqrt{r^2 + z^2}$. Due to the symmetry around the z-axis, $dm \propto 2\pi s^2 sin\theta d\theta$. Therefore to maintain dm=cte, $df \equiv sin\theta d\theta$ has to be constant too, meaning that an uniform distribution in $f \in (0, 1]$ implies a angular mesh following an arcosinus distribution. For arbitrary 1D density profiles we have mapped the particles in that angular arcosinus distribution placing randomly the particles from the origin in such way that total accumulated mass must reproduce the theoretical 1D profile. The resulting distribution of particles and the radial density profile are shown in the left panels of Fig. A.1. Note the lower concentration of particles when the values of the angle are $\theta \approx 0, \pi$ due to the arcosinus distribution. As it can be seen there are local artificial clumps of particles producing noise in the density profile. Allowing the particle to move angularly in θ (what it is called *angular relaxation*) we get smoothed profiles (see the central panels of Fig A.1). In a third step we let the system evolve without any constraint. After several hundreds models the system achieves the adequate configuration to be used as an initial model. The spatial distribution of particles and radial density profile after this third stage are shown in the rightmost panels of Fig A.1.

Appendix B

Appendix: Adaptive Harmonic Kernel

As it has been mentioned one of the most important challenges of the SPH technique is to adequately capture the physical discontinuities that appear in some situations, for example in those were shocks or thermal discontinuities are present. In these cases the nature of the kernel becomes relevant to reduce the errors associated to interpolations which can especially affect the calculation of gradients.

Occasionally, it can be helpful to use a more centrally peaked kernel to better reproduce the maximum value of sharp profiles. For example, it is well known that strong shocks moving through a perfect gas with $\gamma = 5/3$ do present a jump in density $\rho_{max}/\rho_0 = 4$. Such jump is difficult to achieve in more than 1D because of the limited resolution of simulations. A possible way to improve the description of discontinuities is to modify the profile of the kernel in the neighborhood of a shock wave or any kind of discontinuities. In this respect Price [61] found that using the quintic M6 polynomial interpolator leads to more satisfactory results than using the standard M4 cubic-spline kernel. A more sophisticated approach was proposed by Owen et al [56] who used highly adaptive kernels which change their geometry from the standard spherically symmetric to an ellipsoid in the presence of a shock (with its minor axis oriented in the shock direction).

Recently we proposed [10] a one-parameter family of interpolating kernels, with compact support based on harmonic-like functions that covers the whole range of the spline kernels in a continuous manner by simply varying a leading parameter n. The

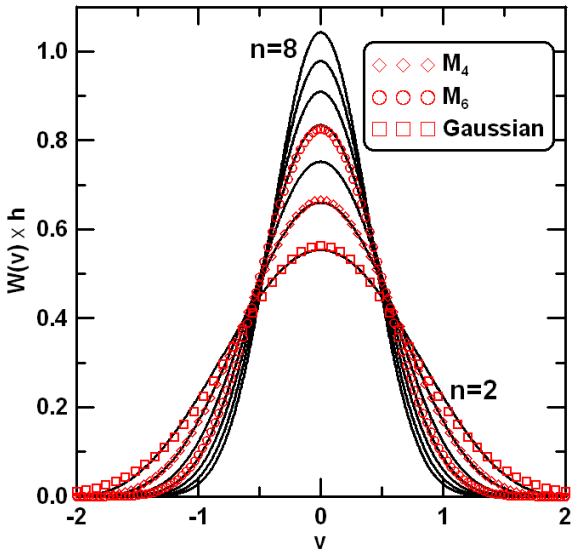

Figure B.1: Profiles of $W_n^H \times h$ in 1D for integer values of n in the range $2 \leq n \leq 8$. Superposed are also depicted the profiles of various of the most common kernels used in SPH: M_4 (cubic spline), M_6 (quintic spline) and truncated Gaussian.

different shapes of the kernel range from more extend to more centrally condensed profiles as the parameter n increases in order to increase the local resolution when it is necessary. This set of functions $W_n^H(v,h)$ is defined as

$$W_n^H(v,h) = \frac{B_n}{h^2} \begin{cases} 1 & v = 0 \\ \left(\frac{\sin\left[\frac{\pi}{2}v\right]}{\frac{\pi}{2}v} \right)^n & 0 < v \leq 2 \\ 0 & v > 2 \end{cases} , \tag{B.1}$$

where B_n is a normalization factor. In Fig B.1 is plotted the different profiles of $W_n^H(v,h)$ for values of n from 2 to 8, as it can clearly seen the resulting profile for $n = 3$ is very close to that of the cubic spline (Eq. 2.6, represented with diamonds in Fig B.1), as well as the profile for $n = 5$ that matches very well the quintic M6 polynomial interpolator profile (renormalizated for $0 \leq v \leq 2$ [10] and plotted with circles in Fig B.1).

An interesting feature is that contrary on the cubic spline, whose second derivative is not smooth in several points, the set of functions $W_n^H(v,h)$ is infinitely derivable, with continuous an well-behaved derivatives (see Fig B.2).

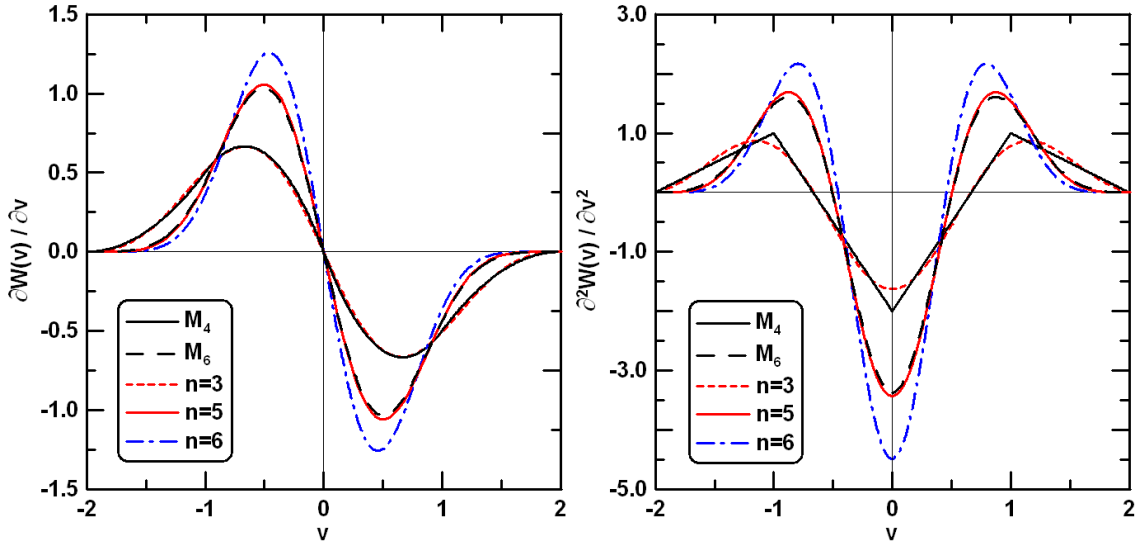

Figure B.2: First (left) and second (right) derivatives of $W_n^H(v,h)$ for $n = 3; 5; 6$ and splines $M4$; $M6$.

Another well-known problem of SPH related with the use of the cubic spline an other bell-shaped kernels is the pairing or tensile-instability. As we can see in the left figure of Fig B.2 those kernels have a minimum v_0 for the first derivative of the kernel $\partial W/\partial v$ ($v_0 = 2/3$ for the cubic spline M_4). For a pair of particles that get closer and $v < v_0$, the gradient of the kernel will decrease and, because the direct dependence of the force to the gradient of the kernel, it can produce the undesirable effect that the *normal* repulsive force between particles diminishes and tends to zero. The net result is that the pair of particles get stuck. Usually the distance from particles is around h so $v \sim 1$ and $v > v_0$. When the particles get closer the smoothing length decreases to keep the number of neighbors approximately constant and v remains $v \sim 1$. Under some anisotropic conditions, like in strong shocks, h decreases but particles along the shock direction get too close, and the reduction of h may be not enough to prevent $v < v_0$, producing pair instability. Although some authors [61] do not consider the pairing instability particularly problematic, we have had some difficulties in our 2D axisymmetric simulations related with this instability when the cubic spline kernel was used. When the particles get too close sometimes they acquire unphysical velocities large enough to move particles to negative r-coordinates, making it impossible to continue the simulation. Fortunately we overcame the problem using the family of kernels $W_n^H(v,h)$. The higher the index n in $W_n^H(v,h)$ is, the closer is v_0 to the origin ($v_0 = 0.5039$ for $n = 5$, see [10] for details), making harder for a couple of particles to get stuck. The parameter n is dy-

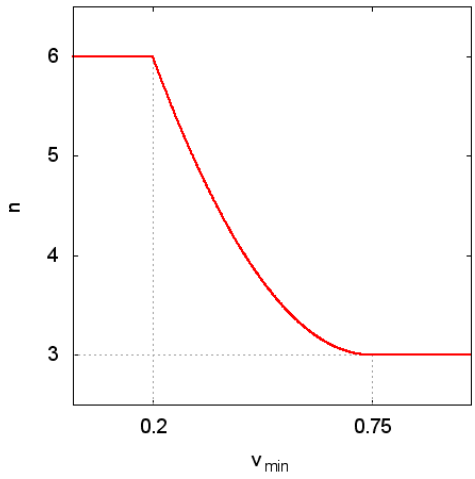

Figure B.3: Plot of n_i, the leading parameter of the family of kernels W_n^H, as a function of v_i^{min}, the minimum scaled distance of each particle to its closest neighbor (v_i^{min}, is in $\tilde{v}$ units, see text).

namically modified during the simulation as a function of the local fluid properties. However, the choice of kernels with a large exponent n is limited by the increase in the numerical noise being therefore restricted to the cases discussed above, that is to track discontinuities and to avoid the pairing instability. The enhancement in resolution is not monotonic as n rises. For $n > 6$ any further increase in resolution is moderate but the noise increases significantly. So in practice we have restricted the values of n to the range $3 \leq n \leq 6$, increasing n using the following functional relation between n and the minimum scaled distance of each particle to its closest neighbor v_i^{min}

$$n_i = \begin{cases} 3 & \frac{3}{4}\tilde{v} < v_i^{min} \\ \frac{300}{121} n_v^0 \left(v_i^{min}\right)^2 - \frac{900}{121}\sqrt{n_v^0} v_i^{min} + \frac{1038}{121} & \frac{1}{5}\tilde{v} \leq v_i^{min} \leq \frac{3}{4}\tilde{v} \\ 6 & v_i^{min} < \frac{1}{5}\tilde{v} \end{cases} , \tag{B.2}$$

where $\tilde{v}$ is the scaled distance between neighbors $\tilde{v} = 2/n_v^0$ assuming that n_v^0 neighbors are homogeneously distributed within a circle of radius $2h$. In Fig. B.3 it is depicted n_i as a function of v_i^{min}.

Notice that the analytical corrections f_1 (Eq. 3.6) and f_2 (Eq. 3.7) that appear in the fluid equations (see Sec. 3.1) have been derived using the cubic spline kernel (see

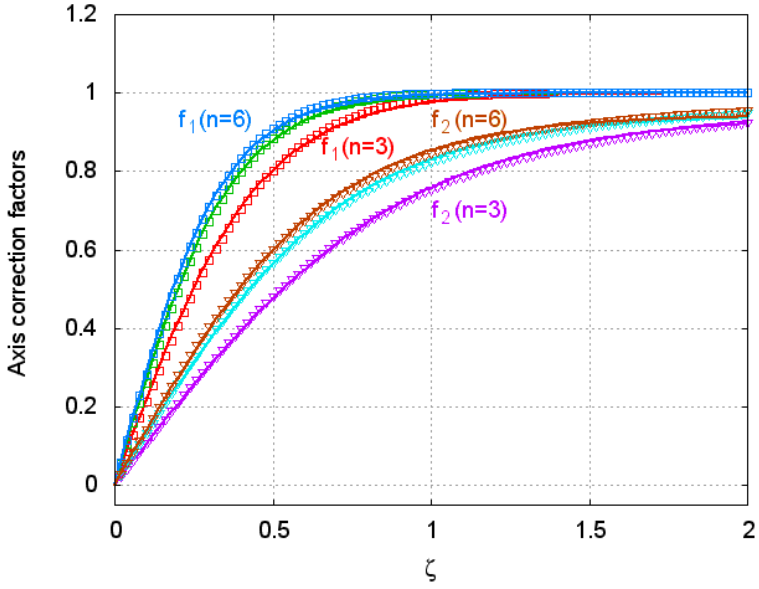

Figure B.4: Correction factors f_1 and f_2 as a function of $\zeta = r/h$, calculated using the kernels W_n^H for n=6, 5 and 3 (squares and inverted triangles respectively). The solid lines represent the fitting obtained using Eq. B.3.

Sec. 2.4 and Sec. 2.6). To be consistent with the introduction of the adaptive harmonic kernels in the simulations, the correction functions must be also recalculated substituting the cubic spline kernel for the $W_n^H(v,h)$.

For the values of $n = 3,4,5,6$ the correction functions f_1 and f_2 have been numerically calculated using the kernels $W_n^H(v,h)$. The results are plotted in a diagram (see Fig. B.4) where it can be seen that the numerical results can be fitted with the analytical functions $\tilde{f}_{k,n}$

$$\tilde{f}_{k,n}(\zeta) = A_k \cdot tanh(B_{k,n} \cdot \zeta)\,, \tag{B.3}$$

where $\zeta = r/h$ is the distance to the z-axis, A_k and $B_{k,n}$ are different constants, $k = 1$ and $k = 2$ refers the approximated functions f_1 and f_2 respectively, for the different values of the kernel parameter $n = 3,4,5,6$. The values of $B_{k,n}$ are provided in Tab. B.1 and $A_1 = 1.0$ and $A_2 = 0.944289$

For any real value of n the parameters $B_{k,n}$ $(k = 1,2)$ have been approximated by a polynomial function

n	$B_{1,n}$	$B_{2,n}$	l	$b_{1,l}$	$b_{2,l}$
2	1.88965	0.94581	0	$1.09342 \cdot 10^{\ 0}$	$5.45570 \cdot 10^{-1}$
3	2.20552	1.10549	1	$4.70213 \cdot 10^{-1}$	$2.35557 \cdot 10^{-1}$
4	2.48501	1.24723	2	$-4.26621 \cdot 10^{-2}$	$-2.09781 \cdot 10^{-2}$
5	2.73767	1.37563	3	$3.59250 \cdot 10^{-3}$	$1.77301 \cdot 10^{-3}$
6	2.96962	1.49357	4	$-1.42917 \cdot 10^{-4}$	$-7.18333 \cdot 10^{-5}$

Table B.1: Values of $B_{1,n}$ and $B_{2,n}$ for integers values of n, and fitting coefficients to $B_{1,n}$ and $B_{2,n}$ for non integers values of n (see Eq.B.4).

$$B_{k,n} = b_{k,4} \cdot n^4 + b_{k,3} \cdot n^3 + b_{k,2} \cdot n^2 + b_{k,1} \cdot n + b_{k,0} \qquad k = 1, 2\,, \tag{B.4}$$

where the values of the fitting coefficients $b_{k,l}$ are provided in Tab. B.1. Once the parameters $B_{k,n}$ are calculated for any real value of n the approximated correction functions $\tilde{f}_{k,n}$ of f_1 and f_2 are estimated using Eq. B.3.

The values of $\partial f_k / \partial r$ needed to evaluate the energy equation (Eq. 2.103) can be easily calculated just making the derivative of $\tilde{f}_{k,n}$

$$\frac{\partial \tilde{f}_{k,n}}{\partial r} = \frac{\partial \tilde{f}_{k,n}}{\partial \zeta} \cdot \frac{d\zeta}{dr} = \frac{A_k B_{k,n}}{h} \cdot \frac{1}{cosh^2(B_{k,n}\zeta)}\,. \tag{B.5}$$

Appendix C

Abbreviations and acronyms

In the following, we include a list with the abbreviations and acronyms used in the text.

AMR	Adaptive Mesh Refinement
AV	Artificial Viscosity
D-T	Deuterium-Tritium
EOS	Equation Of State
ICF	Inertial Confinement Fusion
IME	Intermediate-Mass Elements
KH	Kelvin-Helmholtz
PPM	Piecewise Parabolic Method
RM	Richtmyer-Meshkov
RT	Rayleigh-Taylor
SN	Supernova
SPH	Smoothed Particle Hydrodynamics
WD	White Dwarf

List of Figures

List of Tables

References

[1] Agertz, O., Moore, B., Stadel, J., Potter, D., Miniati, F., Read, J., Mayer, L., Gawryszczak, A., Kravtsov, A., Nordlund, Å., Pearce, F., Quilis, V., Rudd, D., Springel, V., Stone, J., Tasker, E., Teyssier, R., Wadsley, J., and Walder, R. Fundamental differences between SPH and grid methods. *MNRAS 380* (Sept. 2007), 963–978.

[2] Atzeni, S. LETTER: Ablative stabilization of short wavelength Rayleigh-Taylor instability. *Nuclear Fusion 36* (Jan. 1996), 69–74.

[3] Atzeni, S., and Meyer-Ter-Vehn, J. *The Physics of Inertial Fusion: Beam Plasma Interaction, Hydrodynamics, Hot Dense Matter*. Oxford Science Publications, 2004.

[4] Atzeni, S., Schiavi, A., and Temporal, M. Converging geometry Rayleigh Taylor instability and central ignition of inertial confinement fusion targets. *Plasma Physics and Controlled Fusion 46* (2004), B111–B120.

[5] Balsara, D. Von Neumann stability analysis of smoothed particle hydrodynamics - Suggestions for optimal algorithms. *J. Comp. Phys. 121* (1995), 357–372.

[6] Bell, A. R. Non-Spitzer heat flow in a steadily ablating laser-produced plasma. *Physics of Fluids 28* (1985), 2007–2014.

[7] Børve, S., Sato, H., Pécseli, H. L., and Trulsen, J. K. Minute-scale period oscillations of the magnetosphere. *Annales Geophysicae 29* (2011), 663–671.

[8] Brookshaw, L. Smooth particle hydrodynamics in cylindrical coordinates. *ANZIAM 44* (2003), 114–139.

[9] Cabezón, R. M., García-Senz, D., and Bravo, E. High-Temperature Combustion: Approaching Equilibrium Using Nuclear Networks. *ApJS 151* (Apr. 2004), 345–355.

[10] Cabezón, R. M., García-Senz, D., and Relaño, A. A one-parameter family of interpolating kernels for smoothed particle hydrodynamics studies. *Journal of Computational Physics 227* (2008), 8523–8540.

[11] Cantó, J., Tenorio-Tagle, G., and Rozyczka, M. The formation of interstellar jets by the convergence of supersonic conical flows. *A&A 192* (Mar. 1988), 287–294.

[12] Chandrasekhar, S. *Hydrodynamic and hydromagnetic stability*. Oxford University Press, 1961.

[13] Ciardi, A. Laboratory Studies of Astrophysical Jets. In *Lecture Notes in Physics, Berlin Springer Verlag* (Mar. 2010), P. J. V. Garcia & J. M. Ferreira, Ed., vol. 793 of *Lecture Notes in Physics, Berlin Springer Verlag*, p. 31.

[14] Clayton, D. D. *Principles of Stellar Evolution and Nucleosynthesis*. McGraw-Hill, 1968.

[15] Colgate, S. A., and White, R. H. The Hydrodynamic Behavior of Supernovae Explosions. *ApJ 143* (Mar. 1966), 626–681.

[16] Crespo, A., Dominguez, J., Barreiro, A., Gómez-Gesteira, M., and Rogers, B. DualSPHysics, new GPU computing on SPH models. In *Schriftenreihe Schiffbau 6th SPHERIC* (2011), Edited by Hamburg University of Technology, Ed., pp. 348–354.

[17] Ellinger, C. I., Young, P. A., Fryer, C. L., and Rockefeller, G. R. Development of Structure in Supernova Simulations From the Explosion out to Late Times. In *American Astronomical Society* (Jan. 2011), vol. 43 of *Bulletin of the American Astronomical Society*, p. 423.05.

[18] Epperlein, E. M., Rickard, G. J., and Bell, A. R. Two-dimensional nonlocal electron transport in laser-produced plasmas. *Physical Review Letters 61* (1988), 2453–2456.

[19] Fryer, C. L., and Warren, M. S. Modeling Core-Collapse Supernovae in Three Dimensions. *ApJ 574* (July 2002), L65–L68.

[20] Fryer, C. L., and Warren, M. S. The Collapse of Rotating Massive Stars in Three Dimensions. *ApJ 601* (Jan. 2004), 391–404.

[21] García-Senz, D., Badenes, C., and Serichol, N. Is There a Hidden Hole in Type Ia Supernova Remnants? *ApJ 745* (2012), 75.

[22] García-Senz, D., and Bravo, E. Type Ia Supernova models arising from different distributions of igniting points. *A&A 430* (2005), 585–602.

[23] García-Senz, D., Cabezón, R. M., and Escartín, J. A. Improving smoothed particle hydrodynamics with an integral approach to calculating gradients. *A&A 538* (2012), A9.

[24] García-Senz, D., Relaño, A., Cabezón, R. M., and Bravo, E. Axisymmetric smoothed particle hydrodynamics with self-gravity. *MNRAS 392* (2009), 346–360.

[25] Gingold, R. A., and Monaghan, J. J. Smoothed particle hydrodynamics - Theory and application to non-spherical stars. *MNRAS 181* (1977), 375–389.

[26] Harlow, F. H., and Pracht, W. E. Formation and Penetration of High-Speed Collapse Jets. *Physics of Fluids 9* (Oct. 1966), 1951–1959.

[27] Herant, M. Dirty Tricks for SPH (Invited paper). *Mem. Soc. Astron. Italiana 65* (1994), 1013.

[28] Herant, M., and Benz, W. Postexplosion Hydordynamics of SN 1987A. *MNRAS 387* (1992), 294–307.

[29] Hernquist, L., and Katz, N. TREESPH - A unification of SPH with the hierarchical tree method. *ApJS* **70** (1989), 419–446.

[30] Hubber, D. A., Falle, S. A. E. G., and Goodwin, S. P. Convergence of SPH and AMR simulations. In *IAU Symposium* (Apr. 2011), J. Alves, B. G. Elmegreen, J. M. Girart, & V. Trimble, Ed., vol. 270 of *IAU Symposium*, pp. 429–432.

[31] Jubelgas, M., Springel, V., and Dolag, K. Thermal conduction in cosmological SPH simulations. *MNRAS 351* (2004), 423–435.

[32] Knoll, D., Morel, J., Margolin, L., and Shashkov, M. Physically motivated discretization methods. *Los Alamos Science*, 29 (2005), 188–212.

[33] Lebedev, S. V., Chittenden, J. P., Beg, F. N., Bland, S. N., Ciardi, A., Ampleford, D., Hughes, S., Haines, M. G., Frank, A., Blackman, E. G., and Gardiner, T. Laboratory Astrophysics and Collimated Stellar Outflows: The Production of Radiatively Cooled Hypersonic Plasma Jets. *ApJ 564* (Jan. 2002), 113–119.

[34] Lindl, J. Development of the indirect-drive approach to inertial confinement fusion and the target physics basis for ignition and gain. *Physics of Plasmas 2* (1995), 3933–4024.

[35] Lobatchev, V., and Betti, R. Ablative Stabilization of the Deceleration Phase Rayleigh-Taylor Instability. *Physical Review Letters 85* (Nov. 2000), 4522–4525.

[36] Lorén-Aguilar, P., Isern, J., and García-Berro, E. High-resolution smoothed particle hydrodynamics simulations of the merger of binary white dwarfs. *A&A 500* (2009), 1193–1205.

[37] Lucy, L. B. Numerical approach to the testing of the fission hypothesis. *AJ 82* (1977), 1013–1024.

[38] Marek, A., and Janka, H.-T. Delayed Neutrino-Driven Supernova Explosions Aided by the Standing Accretion-Shock Instability. *ApJ 694* (2009), 664–696.

[39] Marinak, M. M., Kerbel, G. D., Gentile, N. A., Jones, O., Munro, D., Pollaine, S., Dittrich, T. R., and Haan, S. W. Three-dimensional HYDRA simulations of National Ignition Facility targets. *Physics of Plasmas 8* (May 2001), 2275–2280.

[40] Marrone, S., Colagrossi, A., Antuono, M., Lugni, C., and Tulin, M. P. A 2D+t SPH model to study the breaking wave pattern generated by fast ships. *Journal of Fluids and Structures 27* (2011), 1199–1215.

[41] Mizuta, A., Yamada, S., and Takabe, H. Numerical Analysis of Jets Produced by Intense Laser. *ApJ 567* (2002), 635–642.

[42] Monaghan, J. J. On the problem of penetration in particle methods. *J. Comp. Phys. 80* (1989), 1–15.

[43] Monaghan, J. J. Smoothed particle hydrodynamics. *ARA&A 30* (1992), 543–574.

[44] Monaghan, J. J. SPH and Riemann Solvers. *Journal of Computational Physics 136* (1997), 298–307.

[45] Monaghan, J. J. Smoothed particle hydrodynamics. *Rep. Prog. Phys. 68* (2005), 1703–1759.

[46] Monaghan, J. J., and Lattanzio, J. C. A refined particle method for astrophysical problems. *A&A 149* (1985), 135–143.

[47] Morsony, B. J., Lazzati, D., and Begelman, M. C. Temporal and Angular Properties of Gamma-Ray Burst Jets Emerging from Massive Stars. *ApJ 665* (2007), 569–598.

[48] Mueller, E. Nuclear-reaction networks and stellar evolution codes - The coupling of composition changes and energy release in explosive nuclear burning. *A&A 162* (1986), 103–108.

[49] Müller, M., Schirm, S., and Teschner, M. Interactive blood simulation for virtual surgery based on smoothed particle hydrodynamics. *Technology and health care official journal of the European Society for Engineering and Medicine 12*, 1 (2004), 25–31.

[50] Nakai, S., and Mima, K. Laser driven inertial fusion energy: present and prospective. *Reports on Progress in Physics 67* (2004), 321–349.

[51] Nakai, S., and Takabe, H. Principles of inertial confinement fusion - physics of implosion and the concept of inertial fusion energy. *Reports on Progress in Physics 59* (1996), 1071–1131.

[52] Noh, W. F. Errors for calculations of strong shocks using an artificial viscosity and an artificial heat flux. *Journal of Computational Physics 72* (1987), 78–120.

[53] Ogando, F., and Velarde, P. Development of a radiation transport fluid dynamic code under AMR scheme. *J. Quant. Spec. Radiat. Transf. 71* (2001), 541–550.

[54] Omang, M., Børve, S., and Trulsen, J. Alternative kernel functions for Smoothed Particle Hydrodynamics in cylindrical symmetry. *Shock Waves 14* (2005), 293–298.

[55] Omang, M., Børve, S., and Trulsen, J. SPH in spherical and cylindrical coordinates. *Journal of Computational Physics 213* (2006), 391–412.

[56] Owen, J. M., Villumsen, J. V., Shapiro, P. R., and Martel, H. Adaptive Smoothed Particle Hydrodynamics: Methodology. II. *ApJS 116* (1998), 155–209.

[57] Petschek, A. G., and Libersky, L. D. Cylindrical Smoothed Particle Hydrodynamics. *Journal of Computational Physics 109* (1993), 76–83.

[58] Post, D. Codes Written by the National and International Computational Physics Community. *LA-UR-02-6284* (2002), 1–157.

[59] Price, D. J. Splash: An interactive visualisation tool for smoothed particle hydrodynamics simulations. *Publications of the Astronomical Society of Australia 24*, 3 (2007), 14.

[60] Price, D. J. Modelling discontinuities and Kelvin Helmholtz instabilities in SPH. *Journal of Computational Physics 2271* (2008), 10040–10057.

[61] Price, D. J. Smoothed Particle Hydrodynamics and Magnetohydrodynamics. *Journal of Computational Physics* (2010).

[62] Ramirez, J., Ramis, R., and Meyer-Ter-Vehn, J. Integrated numerical simulation of indirect laser-driven implosion for icf. *Laser and Particle Beams 16*, 01 (1998), 91–99.

[63] Raskin, C., Scannapieco, E., Rockefeller, G., Fryer, C., Diehl, S., and Timmes, F. X. ^{56}Ni Production in Double-degenerate White Dwarf Collisions. *ApJ 724* (Nov. 2010), 111–125.

[64] Raskin, C., Timmes, F. X., Scannapieco, E., Diehl, S., and Fryer, C. On type ia supernovae from the collisions of two white dwarfs. *MNRAS 399* (Oct. 2009), L156–L159.

[65] Rathkopf, J., Miller, D., Owen, J., Stuart, L., Zika, M., Eltgroth, P., Madsen, N., McCandless, K., Nowak, P., Nemanic, M., Gentile, N., Keen, N., and Palmer, T. KULL: LLNL's ASCI inertial confinement fusion simulation code. In *Physor 2000 American Nuclear Society Topical Meeting on Advances in Reactor Physics and Mathematics and Computation into the Next Millennium* (2000).

[66] Relaño, A., García-Senz, and Bravo, E. Numerical hydrodynamics of inertial confinement fusion: First steps toward a gridless particle approach. In

Mathematics and Computation, Reactor Physics and Environmental Analysis in Nuclear Applications (1999), pp. 228–238.

[67] Relaño, A., García-Senz, and Bravo, E. The stagnation phase of an icf capsule simulated with an axisymmetrical smoothed-particle-hydrodynamics code. In *Proceedings of the XXIX ECLIM 29th European Conference on Laser Interaction with Matter* (2006), pp. 91–96.

[68] Rosswog, S. Astrophysical smooth particle hydrodynamics. *New. Astron. Rev. 53* (2009), 78–104.

[69] Rosswog, S., Kasen, D., Guillochon, J., and Ramirez-Ruiz, E. Collisions of White Dwarfs as a New Progenitor Channel for Type Ia Supernovae. *ApJ 705* (Nov. 2009), L128–L132.

[70] Sakagami, H., and Nishihara, K. Rayleigh-Taylor instability on the pusher-fuel contact surface of stagnating targets. *Physics of Fluids B 2* (1990), 2715–2730.

[71] Sakagami, H., and Nishihara, K. Three-dimensional Rayleigh-Taylor instability of spherical systems. *Physical Review Letters 65* (July 1990), 432–435.

[72] Sakaiya, T., Azechi, H., Matsuoka, M., Izumi, N., Nakai, M., Shigemori, K., Shiraga, H., Sunahara, A., Takabe, H., and Yamanaka, T. Ablative rayleigh-taylor instability at short wavelengths observed with moiré interferometry. *Phys. Rev. Lett. 88*, 14 (Mar 2002), 145003.

[73] Sangster, T. C., Betti, R., Craxton, R. S., Delettrez, J. A., Edgell, D. H., Elasky, L. M., Glebov, V. Y., Goncharov, V. N., Harding, D. R., Jacobs-Perkins, D., Janezic, R., Keck, R. L., Knauer, J. P., Loucks, S. J., Lund, L. D., Marshall, F. J., McCrory, R. L., McKenty, P. W., Meyerhofer, D. D., Radha, P. B., Regan, S. P., Seka, W., Shmayda, W. T., Skupsky, S., Smalyuk, V. A., Soures, J. M., Stoeckl, C., Yaakobi, B., Frenje, J. A., Li, C. K., Petrasso, R. D., Séguin, F. H., Moody, J. D., Atherton, J. A., MacGowan, B. D., Kilkenny, J. D., Bernat, T. P., and Montgomery, D. S. Cryogenic DT and D_2 targets for inertial confinement fusion. *Physics of Plasmas 14*, 5 (May 2007), 058101.

[74] Sijacki, D., and Springel, V. Hydrodynamical simulations of cluster formation with central AGN heating. *MNRAS 366* (2006), 397–416.

[75] Smalyuk, V. A., Delettrez, J. A., Goncharov, V. N., Marshall, F. J., Meyerhofer, D. D., Regan, S. P., Sangster, T. C., Town, R. P. J., and Yaakobi, B. Rayleigh-Taylor instability in the deceleration phase of spherical implosion experiments. *Physics of Plasmas 9* (June 2002), 2738–2744.

[76] Spitzer, L., and Härm, R. Transport phenomena in a completely ionized gas. *Phys. Rev. 89*, 5 (Mar 1953), 977–981.

[77] Stone, J. M., Pringle, J. E., and Begelman, M. C. Hydrodynamical non-radiative accretion flows in two dimensions. *MNRAS 310* (1999), 1002–1016.

[78] Tabak, M., Hammer, J., Glinsky, M. E., Kruer, W. L., Wilks, S. C., Woodworth, J., Campbell, E. M., Perry, M. D., and Mason, R. J. Ignition and high gain with ultrapowerful lasers. *Physics of Plasmas 1* (May 1994), 1626–1634.

[79] Takabe, H., and Ishii, T. Effect of Nonuniform Implosion on High-Gain Intertial Confinement Fusion Targets. *Japanese Journal of Applied Physics 32* (1993), 5675.

[80] Tasker, E. J., Brunino, R., Mitchell, N. L., Michielsen, D., Hopton, S., Pearce, F. R., Bryan, G. L., and Theuns, T. A test suite for quantitative comparison of hydrodynamic codes in astrophysics. *MNRAS 390* (Nov. 2008), 1267–1281.

[81] Temporal, M., Honrubia, J. J., and Atzeni, S. Numerical study of fast ignition of ablatively imploded deuterium-tritium fusion capsules by ultra-intense proton beams. *Physics of Plasmas 9* (2002), 3098–3107.

[82] Timmes, F. X., and Swesty, F. D. The Accuracy, Consistency, and Speed of an Electron-Positron Equation of State Based on Table Interpolation of the Helmholtz Free Energy. *ApJS 126* (2000), 501–516.

[83] Town, R. P. J., and Bell, A. R. Three-dimensional simulations of the implosion of inertial confinement fusion targets. *Physical Review Letters 67* (1991), 1863–1866.

[84] Velarde, P., García-Senz, D., Bravo, E., Ogando, F., Relaño, A., García, C., and Oliva, E. Interaction of supernova remnants: From the

circumstellar medium to the terrestrial laboratory. *Physics of Plasmas 13*, 9 (Sept. 2006), 092901.

[85] Velarde, P., Ogando, F., Eliezer, S., Martínez-Val, J. M., Perlado, J. M., and Murakami, M. Comparison between jet collision and shell impact concepts for fast ignition. *Laser and Particle Beams 23* (2005), 43–46.

[86] Zhang, W., and MacFadyen, A. I. RAM: A Relativistic Adaptive Mesh Refinement Hydrodynamics Code. *ApJS 164* (May 2006), 255–279.